www.czasopisma.pan.pl PAN POLSKA AKADEMIA NAUK www.journals.pan.pl

Vol. 38 • No. 4 • 2017

Chemical and Process Engineering

Inżynieria Chemiczna i Procesowa

Polish Academy of Sciences
Committee of Chemical and Process Engineering

The Journal is supported by the Ministry of Science and Higher Education

Address

ul. Waryńskiego 1
00-645 Warszawa
cpe.czasopisma.pan.pl; degruyter.com/view/j/cpe

Printed in Poland
Print run: 100 copies

Printing/binding:
Centrum Poligrafii Sp. z o.o.
ul. Łopuszańska 53
02-232 Warszawa

www.czasopisma.pan.pl www.journals.pan.pl
Chemical and Process Engineering 2017, 38 (4), 505-512
DOI: 10.1515/cpe-2017-0039

SHORTER COMMUNICATION

APPLICATION OF FLUORESCENT MARKERS FOR HOMOGENEITY ASSESSMENT OF GRAIN MIXTURES BASED ON MAIZE CONTENT

Dominika B. Matuszek*[1], Krystian Wojtkiewicz[2]

[1]Opole University of Technology, Department of Biosystems Engineering, ul. Prószkowska 76, 45-758 Opole, Poland

[2]Wroclaw University of Science and Technology, Department of Information Systems, Wybrzeże Wyspiańskiego 27, 50-370 Wroclaw, Poland

The paper presents test results for the assessment of the tracer content in a three-component (green peas, sorghum, maize) feed mixture that is based on the fluorescent method. The homogeneity of mixtures was determined on the basis of the maize content (as the key component), which was treated with fluorescent substance: tinopal, rhodamine B, uranine and eosin. The key components were wet-treated with fluorescent substances with different concentrations. Feed components were mixed in a vertical funnel-flow mixer. 10 samples were collected from each mixed batch. Samples were placed in a chamber equipped with UV light and, then, an image recorded as BMP file was generated. The image was analysed by means of the software programme Patan. On the basis of the analyses conducted, data on the maize content marked with a fluorescent marker were obtained. Additionally, the content of the key component was determined in a conventional manner – using an analytical scale. Results indicate the possibility of using this method for homogeneity assessment of the three-component grain mixture. From these tests, fluorescent substances that can be applied in the case of maize as a key component, together with their minimum concentrations, were identified: tinopal 0.3%, rhodamine B 0.001%.

Keywords: grain mixture, fluorescent, homogeneity, image analysis

1. INTRODUCTION

The quality of feed mixtures is determined by means of a number of factors. An adequate feed homogeneity guarantees proper nutrition of livestock intended for food production. The adequate homogeneity can be mentioned as the most relevant among numerous feed quality determinants (Çiftc et al., 2003; Djuragic et al., 2007; Królczyk 2016).

The mixing process as well as the assessment of its efficiency are becoming more and more important. Nowadays, feeds contain a lot of components often added in small doses (e.g. flavours, vitamins, minerals); therefore a proper level of the homogeneity of such a mixture ensures that the animal feed with it will make a full use of its components.

The ideal, yet theoretical, composition of the mixture characterised by an identical amount of all components in each collected sample of the feed is not possible to be obtained in practise (Rocha et al., 2015). During the mixing of granular and bulk components, particular particles tend to occupy specific places in the bed. The location of particles depends on various factors such as: density, size of particles, interactions between them and design parameters of a mixer (Hogg, 2009). In most cases, the aim under industrial conditions is to obtain a homogeneous mixture which is characterised by the lowest possible

*Corresponding authors, e-mail: d.matuszek@po.opole.pl

CV coefficient (not higher than 10%) while maintaining its minimum differentiation between mixing cycles (Rocha et al., 2015).

Reference methods for the assessment of the homogeneity of feedingstuffs are usually based on the determination of various key components, including, *inter alia*, those that are naturally present in the feed, such as: chlorides, carbonates, zinc, copper, manganese, cobalt, methionine or lysine. The second group of methods based on key components added to the feeding stuffs includes iron filings (Microtracer) (Eisenberg, 2008) or amoxicillin, chlortetracycline, doxycycline, lincomycin, tiamulin and tylosin - in the case of medicated feeds (Przeniosło-Siwczyńska et al., 2010). In Poland, the reference method for assessing homogeneity is the determination of the content of chlorides and calcium (Walczyński and Korol, 2007). This article describes the use of high sensitivity photometers to record the light reflected by the coloured particles of the granular mixture. This method was the subject of research of also other authors (Alonso and Alguacil, 1999; Poux et al., 1995; Weinekötter and Reh, 1994). The method of computer image analysis of granular mixtures with different color was described and applied by Boss, Tukiendorf and Matuszek (Boss et al., 2002; Matuszek and Tukiendorf, 2007). This method uses the RGB model to estimate the content of a key component. Among many innovative methods, there are also cases where homogeneity assessment requires manual separation using a set of sieves (Królczyk and Tukiendorf, 2006).

The authors have examined methods for the quality assessment of multicomponent mixtures that can be used for the evaluation of the feed homogeneity. Among the variety of tools, particular attention was paid to the methods using the fluorescence phenomenon and image analysis. These instruments are used in the following industrial sectors: food, agricultural, pharmaceutical and chemical industries (Berthiaux et al., 2006, Coppeta et al., 1995; Dauman et al., 2008; Karumanchi et al., 2011; Lai et al., 2001; Matuszek, 2015; Realpe et al., 2003; Zelko et al., 2012).

The conceptual work (Matuszek et al., 2013) includes attempts to pre-verify the suitability of the proposed method developed by the authors. This article presents the results of the subsequent analyses.

The paper presents the results of homogeneous tests carried out in relation to the three-component grain mixture with the use of fluorescent markers. The suitability of maize as the key component was evaluated and the types and concentrations of the fluorescent solution for this method were determined.

Due to the authors experience the selected method was tested using available equipment. Results are a continuation of the research aiming at developing a fluorescence method applicable for assessing the homogeneity of granular mixtures focusing, above all, on the simplicity, accuracy and reproducibility of results. In order to determine the accuracy of the proposed method, the homogeneity of each of the collected samples was assessed using two methods:

1. by specifying the percentage share of the tracer coated with a fluorescent substance by means of computer image analysis,
2. by specifying the percentage share of the tracer coated with a fluorescent substance by means of the analytical balance.

2. MATERIALS AND METHODS

The solution composed of four fluorescent substances, such as tinopal, fluorescein, eosin and rhodamine B, was used in the research (Table 1). One of the mixtures' components – maize was applied as a tracer. Maize was wet-treated with solutions of fluorescent substances presented in Table 1. After soaking, the grain was naturally dried at the expense of the ambient heat in the laboratory room. After obtaining the appropriate moisture, the tagged grains were stored in appropriately labeled containers at room temperature under the same conditions as the rest of the ingredients.

Table 1. Fluorescence substance used in the tests

Fluorescence tracers	Excitation, nm	Emission, nm	CAS Registry Number	Molecular weight	Formula	Solution, %
Tinopal	350	430	27344-41-8	562.6	$C_{28}H_{20}Na_2O_6S_2$	0.3 0.03
Fluorescein (Uranine)	494	520	518-47-8	376.3	$C_{20}H_{10}Na_2O_5$	0.3 0.03 0.01
Eosin	525	545	15086-94-9	647.9	$C_{20}H_8Br_4O_5$	0.3
Rhodamine B	553	627	88-81-9	479.02	$C_{28}H_{31}ClN_2O_3$	0.3 0.03 0.01 0.007 0.001

Using maize as the key component results from observations and tests conducted and collected at the first stage of the research. The same research excluded the possibility of utilising sorghum or peas for this purpose (Matuszek et al., 2013). The feed mixture contained a three-component structure (green peas, sorghum, maize where the last one was as the key component) with the characteristics presented in Table 2.

Table 2. Characteristics of mixed components

Component	Bulk density, $kg \cdot m^{-3}$	Mean particle size, mm	Share of component, %
green peas	771	6.95	60
sorghum	697	3.94	30
maize	745	8.20	10

These components are often used for the production of feed mixtures. Since multi-component systems are mixed in the industrial practice, tests on multi-component mixtures carried out under laboratory conditions are highly recommended.

The mixing was carried out using a funnel-flow mixer. However, the mixer used is merely a tool for conducting the mixing process which is not the subject of this paper. More details concerning the parameters of the test stand and the mixing process using the pouring method can be found elsewhere (Matuszek et al., 2008). The total mass of the mixed material was 1000g. The mixer tank was filled with 600g of green peas, 300g of green sorghum and 100g of coloured maize. The mixing process was started basis on the flow from one tank to another. Each time, 10 dumps were made. At the end of the mixing process, 10 samples (N = 10) of feed from each tank level were taken (thanks to a special demountable construction of the mixer). The weight of each sample was 40 g. Taken samples before further analysis were placed in sun-proof packs.

For each sample, the share of the tracer was assessed by two methods:

2.1. Method with the use of computer analysis of image

Each collected sample was placed on a clean glass – the Petri plate - of diameter 120 mm and then subsequently immersed in UV-chamber. The chamber was made of the material impermeable to light

rays, equipped with UV light (two 15 W fluorescent lamps without housing). A camera was fixed in the upper part of the chamber to record images in BMP format. A sample of the mixture was placed inside a sealed chamber made of a material not impermeable to external rays. A proper design of the test stand is very important to maintain the reproducibility of measurements (Fig. 1). The sample was illuminated with UV rays and then a picture was taken. Photos of each sample – three shots at the resolution of 1600x1200 pixels were taken. Images obtained in this manner were subjected to computer analysis, using original PATAN® software programme. On the basis of a value scale, the RGB-256 components of the test areas were defined and divided into classes: 1^{s} class – tracer, 2nd class – green peas, and 3rd class - sorghum. Then, the area designated for analysis, i.e. circular area, was determined. Thanks to the analysis of the designated area, information on the percentage share of each class (Fig. 2) in the entire area was obtained. The data on the content of tracer – 1st class (average of three measurements) were used for further analysis. It should also be noted that the size obtained as a result of computations performed using the computer-aided image analysis is a dimensionless parameter, and more precisely, it describes the sum of the area of individual elements belonging to the „tracer" class in relation to the total surface. Therefore, an extremely important aspect is that specific measurements were carried out under the same metrological conditions.

These conditions include, for instance, the distance between the camera and the test sample, lighting conditions, and sample dimensions. The reproducibility of measurements was achieved by means of the specialized test stand ensuring control over the relevant image acquisition parameters. A verification test consisting in the determination of the weight of the tracer in relation to the mass of the entire sample was the reference for the computer-aided image analysis. In order to satisfy the requirements of the research work, it was assumed that this research method is unequivocal.

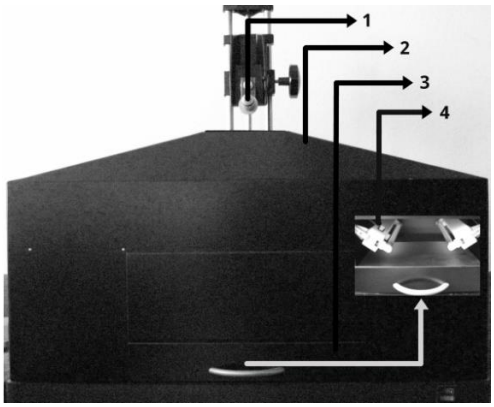

Fig. 1. Stand to take pictures, 1. Camera tripod, 2. Chamber casing , 3. Tray for material samples, UV lighting

a) b)

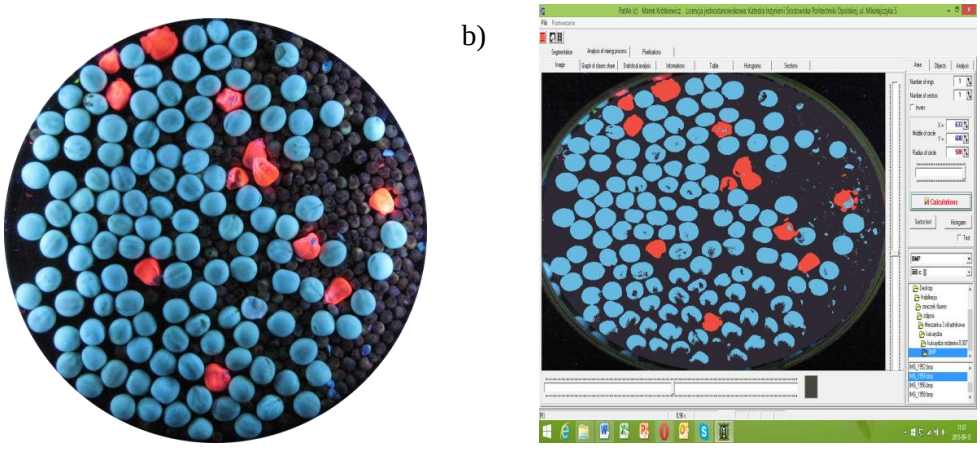

Fig. 2. Image of feed mixture sample (Rhodamine B solution 0.001%) a) image under UV light recorded as .gmp file, b) image after analysis in the Patan® programme.

2.2. Method with analytical scale (control research)

This method based on the precise assessment of the tracer mass in each sample with electronic scales with an accuracy of 0.01 g. Then, in order to compare results obtained from a computer-aided image analysis and the gravimetric method, the so-called percentage content of the tracer (maize) was determined. This parameter was evaluated based on the juxtaposition of the mass (electronic scales) and the share of the tracer (computer-aided image analysis) for various amounts of grains - from 5 to 100. Table 3 obtained in such a way is a useful template for the recalculation of the mass of the tracer to express it as a percentage share of this component (Table 3).

Each series of tests was carried out under identical laboratory conditions as described above.

3. RESULTS AND DISCUSSION

Statistical calculations were performed with Statistica version 12.0 software (StatSoft 2015).

For calculations of t-Student statistics, the following assumptions were made:

- Each of the two populations (population should be understood as the method for the assessment of the share of the tracer) is normally distributed (this assumption was verified using the Shapiro-Wilk test).
- Both populations have equal variances (this assumption was verified by the Fisher test).

The null hypothesis is:

$$H_0: \mu_1 = \mu_2 \tag{1}$$

The means of the populations of interest are equal at the value of $r = 2$.

The alternative hypothesis is:

$$H_1: \mu_1 \neq \mu_2 \tag{2}$$

The means of the populations of interest are different at the value of $r = 2$.

Verification of assumptions (points 1 and 2) was based on the Shapiro-Wilk test (test for normality) and the Fisher's test (F-test of equality of variances). The analysis of hypotheses was performed on the basis of *t*-Student test for independent samples, by assuming the value of significance level equal to $\alpha = 0.05$ (Aczel 2012).

The results of research and statistical calculations are presented in Table 3.

As a result of the analysis of obtained average and standard deviation values, it can be observed that there are significant differences in the share of the tracer on the basis of results obtained with the computer-aided image analysis method and the gravimetric method. It can be noticed that the concentration of the solution is crucial for the suitability of the applied method. It can be presented using the example of Rhodamine B solution, which, at the concentration of 0.3%, is not suitable to be used in the proposed method, while at the concentration of 0.007%, allows to obtain the best results.

Based on the probability analysis with p-value (at $\alpha = 0.05$) presented in Table 3, there is no reason to reject the null hypothesis on the equality of average shares for the main component in the following solutions: 0.3% Tinopal, 0.3% Fluorescein, 0.01%, 0.001% and 0.007% Rhodamine B. It can be assumed that the results are homogeneous and the mixtures analysed by means of these two methods have similar compositions.

Table 3. Results of the assessment on the share of tracer in feed mixture

Fluorescent solution in %	Computer-aided image analysis[a], %	Gravimetric method[a] %	*t* value[b]
Tinopal			
0.3	2.98±0.61	3.05±0.64	0.23*
0.03	2.11±0.84	3.79±0.76	-4.23**
Fluorescein			
0.3	4.92±1.06	4.03±0.98	1.47*
0.03	9.02±1.79	4.20±1.27	6.28**
Rhodamine B			
0.3	10.01±2.52	4.03±0.85	6.44**
0.03	5.06±0.76	3.69±0.40	4.52**
0.01	5.48±1.15	5.70±1.11	-0.39*
0.001	6.18±1.4	6.32±1.54	0.18*
0.007	6.31±0.77	6.43±0.82	-0.31*
Eosin			
0.3	8.21±1.65	4.27±0.82	6.14**

[a] Mean of three analyses and then samples ± standard deviation.

[b] t value with the compare of two methods of mixture homogeneity assesment (n = 2, N = 60)

* Not significance difference beetwen populations at $p < 0.05$

** Significance difference beetwen populations at $p < 0.05$

For other solutions of fluorescent substances (0.03% Tinopal, 0.03% Fluorescein, 0.3% and 0.03% Rhodamine B, 0.3% Eosin) there is no reason to approve the null hypothesis. Therefore, it is concluded that the results obtained by means of these two methods are statistically different.

In case of Rhodamine B, satisfactory results were obtained for three different solutions: 0.01%, 0.007% and 0.001%, respectively. However, it seems that the 0.001% solution is the best (due to the results and economic aspects).

From the experiments and conducted computations, the following solutions of fluorescent substances can be used to assess the homogeneity of the maize-based feed: 0.3% Tinopal, 0.001% Rhodamine B.

The share of tracer in the grain mixture obtained by the fluorescence method can be subsequently applied for standard computations of homogeneity parameters (for example the CV value).

The tests were carried out as they should be in laboratory conditions. The specificity of fluorescent markers requires certain conditions during analysis. An example is the need to protect tags and samples of mixtures from external influences, excluding liquid additives for mixing and wear protective clothing. Fluorescent markers should be considered as chemical reagents that require appropriate conditions (information in safety data sheets). Therefore the possibility of applying the method in industrial scale is considerably reduced and certainly requires additional analysis. Additionally the authors are planning to do more tests with different multi-component grain mixtures of different dimensions of grains and grains after grinding. At this stage of research this method may be used to evaluate the homogeneity of selected granular feeds or granular mixtures before grinding.

4. CONCLUSIONS

It has been shown that there are no statistically significant differences in the share of the key component obtained by means of the two methods for the following fluorescent substances: 0.3% Tinopal, 0.3% Fluorescein, 0.01%, 0.001% and 0.007% Rhodamine. However, statistically significant differences in the share of the tracer were found for substances such as: 0.03% Tinopal, 0.03% Fluorescein, 0.3% and 0.03% Rhodamine B, 0.3% Eosin. The proposed solution can be applied for the determination of the share of the tracer for three-component grain mixtures. Two liquids, namely: Tinopal 0.3% and Rhodamine B 0.001%, are suggested in the methodology based on the analysis of the maize (as a tracer) content.

SYMBOLS

CV	coefficient of variation
H_0	null hypothesis
H_1	alternative hypothesis
p	probability value
α	significance level
μ	mean
r	number of population

REFERENCES

Aczel A., D., 2012. *Complete business statistics*. 8th edition, Wohl Publishing.

Alonso M., Alguacil F.J., 1999. Dry mixing and coating of powders. *Revista de Metalurgia*, 35, 315-328.

Berthiaux H., Mosorov V., Tomczak L., Gatumel C., Demeyre J.F., 2006. Principal component analysis for characterising homogeneity in powder mixing using image processing techniques. C*hem. Eng. Process.*, 45, 397-403. DOI: 10.1016/ j.cep.2005.10.005.

Boss J., Krótkiewicz M., Tukiendorf M., 2002. Porównanie metod oceny jakości stanu mieszaniny ziarnistej podczas mieszania w przesypie. *Inżynieria Rolnicza*, 4 (37), 27-32.

Çiftc I., Ercan A., 2003. Effects of diets of different mixing homogeneity on performance and carcass traits of broilers. *J. Anim. Feed Sci*., 12, 163–171. DOI: 10.22358/jafs/67693/2003.

Coppeta J.R., Rogers C.B., 1995. A quantitative mixing analysis using fluorescent dyes. *AIAA paper number 0539*, American Institute of Aeronautics and Astronautics.

Daumann B., Nirschl H., 2008. Assesment of the mixing efficiency of solid mixtures by means of image analysis. *Powder Technol*., 182, 415-423. DOI: 10.1016/j.powtec.2007.07.006.

Djuragic O., Levic J., Sredanovic S., Lević L., 2007. Evaluation of homogeneity in feed by method of microtracer®. *Archiva Zootechnica*, 12 (4), 85-91.

Eisenberg D., 2008. Measuring mixer variation- performance and cross-contamination validation. *16th Annual ASA-IM SEA Feed Technology and Nutrition Workshop*, Singapore 26-30 May 2008.

Hogg R., 2009. Mixing and segregation in powders: Evaluation, mechanisms and processes. *KONA Powder Part. J*., 27, 3-17. DOI: 10.14356/kona.2009005.

Karumanchi V., Taylor M.K., Ely K.J., Stagner W.S., 2011. Monitoring powder blend homogeneity using light-induced fluorescence. *AAPS PharmSciTech*. 2, 1031–1037. DOI: 10.1208/s12249-011-9667-1.

Królczyk J.B., 2016. Homogeneity assessment of multi-element heterogeneous granular mixtures by using Multivariate Analysis of Variance. *Tehnicki Vjesnik*, 23,383-388. DOI: 10.17559/TV-20151031183255.

Królczyk J., Tukiendorf M., 2006. Optymalizacja procesu sporządzania wieloskładnikowej paszy dla gołębi w pionowym mieszalniku z mieszadłem ślimakowym. *Agricultural Engineering*, 12 (87), 267-275.

Lai C.K., Holt D., Leung J.C., Raju G.K., Hansen P., Cooney C.L., 2001. Real-time and non-invasive monitoring of dry powder blend homogeneity. *AIChE J*. 47, 2618–2622. DOI: 10.1002/aic.690471124.

Matuszek D., 2015. Modelling selected parameters of granular elements in the mixing process. *Int. Agrophys*., 29, 75-81. DOI: 10.1515/intag-2015-0002.

Matuszek D., Szwedziak K., 2013. The use of fluorescent markers in assessing the feed homogeneity. Problems of intensification the animal production with regard to infrastructure, environmental protection and alternative energy production. *Monography*, Institute of Technology and Life Sciences Warsaw, 160-166 (in Polish).

Matuszek D., Tukiendorf M., 2007. Komputerowa analiza obrazu w ocenie mieszania niejednorodnych układów ziarnistych (system funnel-flow). *Agricultural Engineering*, 2 (90), 183-188.

Matuszek D., Tukiendorf M., 2008. Application of roof shaped and double cone inserts in mixing of granular elements in the flow process. *Int. Agrophysics*., 22, 147-150.

Poux M., Lescure M., Steinmetz D., Bertrand J., 1995. Optical sensors for the characterization of powder mixtures. *Sens. Actuators: A*, 47, 494-496.

Przeniosło-Siwczyńska M., Kwiatek K., 2010. Determination of active substances in medicated feedstuffs. *Krmiva* (Zagreb), 52 (3), 165-169.

Realpe A., Velazqez C., 2003. Image processing and analysis for determination of cencentrations of powder mixtures. *Powder Technol*., 134, 193-200. DOI: 10.1016/S0032-5910(03)00138-4.

Rocha A.G., Montanhini R.N., Dilkinb P., Tamiosso C.D., Mallmannb C.A., 2015. Comparison of different indicators for the evaluation of feed mixing efficiency. *Anim. Feed Sci. Technol.*, 209, 249–256. DOI: http://dx.doi.org/10.1016/ j.anifeedsci.2015.09.005.

Satoh M., Miyanami K., 1988. Continuous measurement of degree of mixing in powder mixer by an optical method. *Bulletin of University of Osaka Prefecture*. *Series A, Engineering and Natural Sciences*, 36 (2), 141-148. Available at: http://hdl.handle.net/10466/8456.

StatSoft, Inc. 2015. STATISTICA (data analysis software system), version 12. Available at: www.statsoft.com.

Walczyński S., Korol W., 2007. Inter-laboratory investigations on evaluation of industrial fodder mixtures homogeneity. *Pol J Food Nutr Sci.*, 2007, **57**, 2(A), 187-190.

Weinekötter R., Reh L., 1994. Characterization of particulate mixtures by in-line measurements. *Part. Part. Syst. Char.*, 11 (4), 284-290. DOI: 10.1002/ppsc.19940110403.

Zelko I., Lux A., Sterckeman,T., Martinka M., Kollárová K., Lišková D., 2012. An easy method for cutting and fluorescent staining of thin roots. *Ann. Bot.*, 110, 475 –478. DOI:10.1093/aob/mcs046.

Received 10 June 2016
Received in revised form 29 September 2017
Accepted 01 October 2017

www.czasopisma.pan.pl www.journals.pan.pl
Chemical and Process Engineering 2017, 38 (4), 513-521
DOI: 10.1515/cpe-2017-0040

COMPUTATIONAL FLUID DYNAMICS CALCULATION OF A PLANAR SOLID OXIDE FUEL CELL DESIGN RUNNING ON SYNGAS

Paulina Pianko-Oprych*, Tomasz Zinko, Zdzisław Jaworski

West Pomeranian University of Technology, Szczecin, Faculty of Chemical Technology and Engineering, Institute of Chemical Engineering and Environmental Protection Processes, al. Piastów 42, 71-065 Szczecin, Poland

The present study deals with modelling and validation of a planar Solid Oxide Fuel Cell (SOFC) design fuelled by gas mixture of partially pre-reformed methane. A 3D model was developed using the ANSYS Fluent Computational Fluid Dynamics (CFD) tool that was supported by an additional Fuel Cell Tools module. The governing equations for momentum, heat, gas species, ion and electron transport were implemented and coupled to kinetics describing the electrochemical and reforming reactions. In the model, the Water Gas Shift reaction in a porous anode layer was included. Electrochemical oxidation of hydrogen and carbon monoxide fuels were both considered. The developed model enabled to predict the distributions of temperature, current density and gas flow in the fuel cell.

Keywords: planar Solid Oxide Fuel Cells, Computational Fluid Dynamics, syngas

1. INTRODUCTION

Solid Oxide Fuel Cells, in contrast to PEMFCs, can be fed directly with hydrocarbon fuels containing methane, carbon monoxide or even carbon dioxide generated by reformers (Barelli et al. 2017; D'Andrea et al., 2017; Kang et al. 2008; Stoeckl et al., 2017). No need to eliminate CO through catalytic reactors makes that as a main advantage of using SOFCs. In addition, according to Park et al. (2012) an overall electrochemical reaction rate in the SOFC can vary up to 50% with the oxidation of CO in comparison to only oxidation of hydrogen. Therefore, both hydrogen oxidation and carbon monoxide oxidation should be included in a cell level study. Anode species composition exhibits notable amounts of CO (Tweedie and Lemcoff, 2014). Carbon monoxide oxidation was considered at the cell level modelling by Andersson et al. (2013), Ho et al. (2009), Iwai et al. (2011) as well as Razbani et al. (2013) and at the stack level by Gholaminezhad et al. (2017) and Papurello et al. (2017). Iwai et al. (2011) developed a numerical model for an anode supported, intermediate temperature direct internal reforming planar SOFC. In the simulations steam reforming reactions using methane, the Water-Gas-Shift (WGS) reaction and the electrochemical reactions of hydrogen and carbon monoxide were taken into account. Results showed that the endothermic steam reforming reaction led to a reduction in the local temperature near the inlet and limited the electrochemical reaction rates therein. However, it was found that the local temperature and current density distributions can be controlled by tuning the pre-reforming rate (Iwai et al., 2011). A multi-physics mathematical channel-level direct internal reforming methane fed Solid Oxide Fuel Cell model was presented by Gholaminezhad et al. (2017). The proposed model considered steady-state multi-component mass transport in fuel channel and its coupled effects on electrochemical phenomenon inside the anode porous electrode. Authors

*Corresponding authors, e-mail: paulina.pianko@zut.edu.pl

studied methane conversion, chemical reaction rates, inlet composition and carbon formation boundary as a function of pre-reforming rate, fuel utilisation, current density and temperature. However, Gholaminezhad et al. (2017) ignored in their study the electrochemical oxidation of CO due to the fact that the rate of CO conversion via Water Gas Shift, WGS, reaction was much higher than that with electrochemical oxidation of CO. Authors explained that due to the existence of a high amount of steam in the inlet stream, because of carbon deposition prevention, steam reforming was considered as the only reaction, in which methane was involved. Exclusion of CO from the electrochemical model had generated less accurate results.

Direct internal methane reforming in the high temperature SOFC was investigated by Ho et al. (2009) using Star-CD with in-house developed subroutines. Carbon monoxide produced by the reforming reaction was included in the electrochemical processes, while being in equilibrium with the WGS reaction. Co- and counter flow configurations were tested. For co-flow a sub-cooling effect manifests itself in the methane rich region near the fuel entrance, while for counter flow a super heating effect was noticed in the downstream, where all the methane was consumed.

A fully coupled 3D model was applied also by Razbani et al. (2013) to a planar electrolyte supported SOFC fed by methane free biogas using the COMSOL software. Simulation results showed that using the methane free biogas a more uniform current density profile was obtained due to the high CO_2 content and the reverse WGS reaction. It was noticed that the WGS reaction was faster than the electrochemical reactions. Razbani et al. (2013) explained this behaviour due to the endothermic reverse WGS reaction, when CO and H_2O were produced and caused fast consumption of H_2 and CO_2. The contribution of CO oxidation in the overall current productions ranges from 7% to 17% for cell voltage from 0.9 V to 0.7 V. Andersson et al. (2013) showed that a fuel mixture containing a high fraction of electrochemical reactants such as hydrogen and carbon monoxide enables a high Nernst potential in the region close to the inlet, which increases the current density there. Thus, the Nernst potential covering the electrochemical reaction with carbon monoxide had a stronger influence by changes in the operating temperature in comparison to the reaction with hydrogen only. This relationship will vary for different cell design and operating conditions when the fuel cell was designed. Therefore, the aim of this study was to apply an earlier developed three-dimensional numerical model for pure hydrogen (Pianko-Oprych et al., 2016) to a planar Solid Oxide Fuel Cell design fuelled by reformate mixtures. The idea was to check whether the model after adjustment for the presence of carbon monoxide will be able to predict thermal and electrochemical fuel cell performance. In order to visualise electrochemical and gas phase reaction regions the species and current density distributions were displayed. The obtained results will be used as guidelines for further investigations and identification of proper flow paths that increase the SOFC performance.

2. PHYSICAL AND NUMERICAL MODEL

In the SOFC, electrical and ionic conduction, heat transfer, gas phase mass transport as well as chemical reactions take place simultaneously. To include all the phenomena, conservation equations for momentum, mass, species and energy were applied to the SOFC domains. The Navier-Stokes equations were used to model the flow in the anode and cathode flow channels, while the Brinkman equations were utilised to model the flow in the porous electrodes. For the mass balances, the concentrated species transport equations were used assuming that species transport was dominated by the gas diffusion. Thermal energy was transferred by conduction and convection, while the radiative heat transfer was neglected due to its low impact (Pianko-Oprych et al., 2014). For the electronic and ionic charge balance the appropriate distributed charge transfer equations were applied. The electron transport was considered in order to collect current from the fuel cell. More details on the applied model can be found in (Pianko-Oprych et al., 2016).

In this study, the following electrochemical oxidation reactions of H_2 and CO were considered:

$$H_2 + O^{2-} \rightarrow H_2O + 2e^- \quad (1)$$

$$CO + O^{2-} \rightarrow CO_2 + 2e^- \quad (2)$$

$$½\ O_2 + 2e^- \rightarrow O^2 \quad (3)$$

Carbon monoxide can be oxidized in the electrochemical reaction (Eq. (2)), but can also react with water (Eq. (4)) in the Water Gas Shift (WGS) reaction:

$$CO + H_2O \rightarrow CO_2 + H_2 \quad (4)$$

The cell voltage was determined by setting boundary conditions such that the electrical potential, $\phi_{cell} = 0$ in the anode side, while $\phi_{cell} = E_{\text{cell}}$ in the cathode side (current tap surface). For the study, the cell voltage was varied from 1.1 to 0.3. To calculate the volumetric current densities, the Butler-Volmer equations were used (Eqs.(5-7)):

$$i_{H_2} = i_{0,an,H_2}\left[\exp\left(\frac{\alpha_{anode} n\eta_{act,an,H_2} F}{RT}\right) - \exp\left(\frac{\alpha_{cathode} n\eta_{act,an,H_2} F}{RT}\right)\right] \quad (5)$$

$$i_{CO} = i_{0,an,CO}\left[\exp\left(\frac{\alpha_{anode} n\eta_{act,an,CO} F}{RT}\right) - \exp\left(\frac{\alpha_{cathode} n\eta_{act,an,CO} F}{RT}\right)\right] \quad (6)$$

$$i_{O_2} = i_{0,cat,O_2}\left[\exp\left(\frac{\alpha_{anode} n\eta_{act,an,O_2} F}{RT}\right) - \exp\left(\frac{\alpha_{cathode} n\eta_{act,an,O_2} F}{RT}\right)\right] \quad (7)$$

where: i_{H_2}, i_{CO}, i_{O_2} are the current density, $i_{0,an,H_2}, i_{0,an,CO}, i_{0,cat,O_2}$, are the effective exchange current density, F is the Faraday's constant, n is the number of electrons that are released per reaction, R is the universal gas constant, T is the absolute temperature and α_{anode} and $\alpha_{cathode}$ are anodic and cathodic transfer coefficients, respectively.

The computational domain of a planar SOFC design consisted of three ceramic layers of membrane electrode assembly: anode, electrolyte, cathode and of two cross-flow bipolar plates with 26 ribs as shown in Fig. 1a. The gases flowed in part horizontally or vertically and diagonally in average. The fuel and air flows were cross-wise opposed on each bipolar plate side.

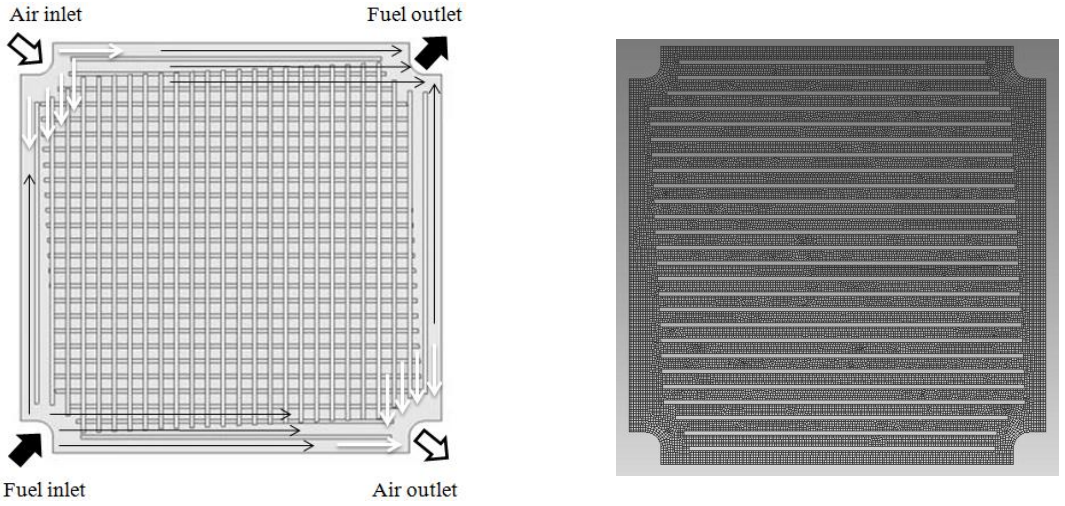

Fig. 1. A schematic of the planar Solid Oxide Fuel Cell design (a) and numerical mesh (b)

The mesh consisted of 890 thousand computational cells generated in the ANSYS Meshing 15.0 and it is presented in Fig. 1b. The physical properties of the SOFC are shown in Table 1, where YSZ means Yttria-Stabilized Zirconia, Ni - Nickel, LSM - Lanthanum Strontium Manganite. The operating conditions and input parameters for the SOFC model are listed in Table 2. All layers of the SOFC membrane-electrode assembly including a thin cathode were resolved in the model with one exception – a thin electrolyte was considered as electrode-electrolyte interfaces.

Table 1. Physical properties of the SOFC

Parameter	Anode	Electrolyte	Cathode	Current collectors
Material	Ni-YSZ	YSZ	LSM	-
Thickness, mm	0.25	0.01	0.06	1
Density, kg/m^3	7740	6000	5300	7450
Specified heat capacity, J/(kg·K)	595	400	607	600
Thermal conductivity, W/(m·K)	6.23	2.7	10	27
Resistivity, Ohm·m	-	0.1	-	-
Electronic conductivity, 1/(Ohm·m)	30300	-	12800	769000
Anode-current collectors contact resistance, Ohm·m^2	1×10^{-7}	-	1×10^{-8}	-
Porosity	0.3	-	0.3	-

Table 2. Boundary conditions of the SOFC model

Domain region	Parameter	Value
Air inlet	Flow rate:	0.25 l/min
	Temperature:	973 K
	Mass fraction of species:	23.3% O_2, 76.7% N_2
Fuel inlet	Flow rate:	0.075 l/min
	Temperature:	973 K
	Mass fraction of species:	75% H_2, 25% CO
Air outlet	Pressure:	1×10^5 Pa
Outer current collector (anode side) surface	Voltage tap surface:	0 V
Outer current collector (cathode side) surface	Current tap surface:	0.7 V
Anode	Exchange current density	7460 A·m^2
Cathode	Exchange current density	10090 A·m^2

In order to attain convergence for the momentum, energy and species differential equations the second order upwind discretisation scheme was used, while for the pressure equation the second order discretisation scheme was applied. Discretisation of the electric potential by the first order upwind scheme was considered, while for gradient estimations the Green Gauss node was used. The 3D computational model was developed in the commercial CFD code ANSYS Fluent 15.0 with an additional ANSYS Fuel Cell Tools module.

3. RESULTS AND DISCUSSION

The current - voltage curve was constructed and validated against the experimental data of Bossel (2015). A comparison of the calculated voltage vs. current curve with the experimental results for syngas is presented in Fig. 2. The CFD curve corresponds quite well with the experimental one for the operating voltage of 1.1 and 0.7 V, while at the lowest analysed voltage of 0.3 V significant deviation in the electrical current was noticed for the reformate. A sudden drop of power was observed at the highest current value and it can be explained by fuel starvation. Similar behaviour was observed in the previous paper (Pianko-Oprych et al., 2016), when pure hydrogen was used as a working fuel. This type of behaviour may result from the applied numerical procedure, in which the flow rates of the fuel and air for considered voltage values have to be kept constant, while during measurements the flow rate is adjusted according to the working conditions inside the fuel cell in order to avoid fuel cell destruction due to reagent starvation.

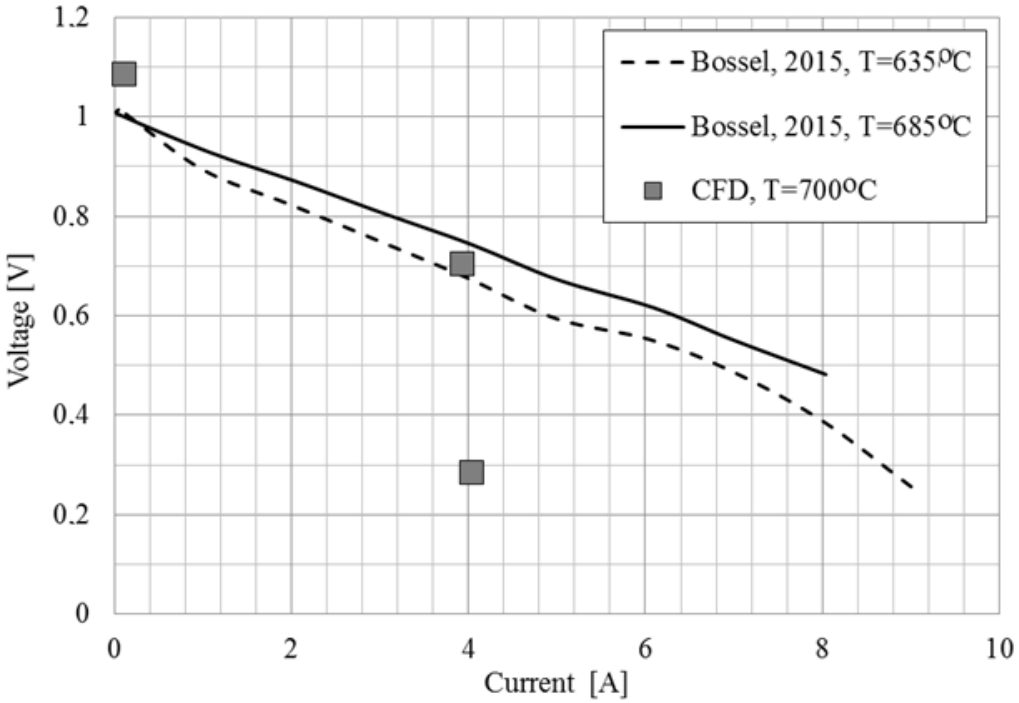

Fig. 2. Voltage [V] vs. current [A] curve for the single planar SOFC at temperature of 700 °C and fed by syngas

An attempt to explain such SOFC behaviour was undertaken. For this purpose, hydrogen, water, oxygen, CO and CO_2 mass fraction distributions were shown in Table 3, respectively. The fuel inlet of hydrogen and CO was located in the left bottom corner, while the air inlet was located in the upper left corner. The mean fuel and air flow directions were across the fuel cell and perpendicular to each other. The mass fractions of hydrogen and carbon monoxide significantly change diagonally between the fuel inlet and outlet. The simulation results indicate the regions where hydrogen and carbon monoxide were available electrochemically highly active and the fuel cell was locally able to produce current at the applied voltage, while in the areas where local fuel starvation can be noticed, the cell could not produce enough electrical current particularly at the cell voltage of 0.3 V. It can be noticed that the areas where hydrogen and carbon monoxide concentrations strongly decreased (Tables 3a and 3d) overlap with regions of the highest current density (Table 5). What was surprising the WGS reaction showed the most activity at the upper part of the cell in the regions close to the air inlet and fuel outlet surfaces, where a higher amount of CO_2 was noticed at the electrolyte interface from the anode side. On the other hand, increasing the mass fraction of water decreased the probability of carbon formation although temperature gradients across the fuel cell may contribute to its occurrence.

Table 3. Table 3. Species distributions [kg/kg] in the electrolyte from the anode side: (a) mass fraction of hydrogen, (b) mass fraction of water, (c) mass fraction of oxygen, (d) mass fraction of CO, (e) mass fraction of CO_2

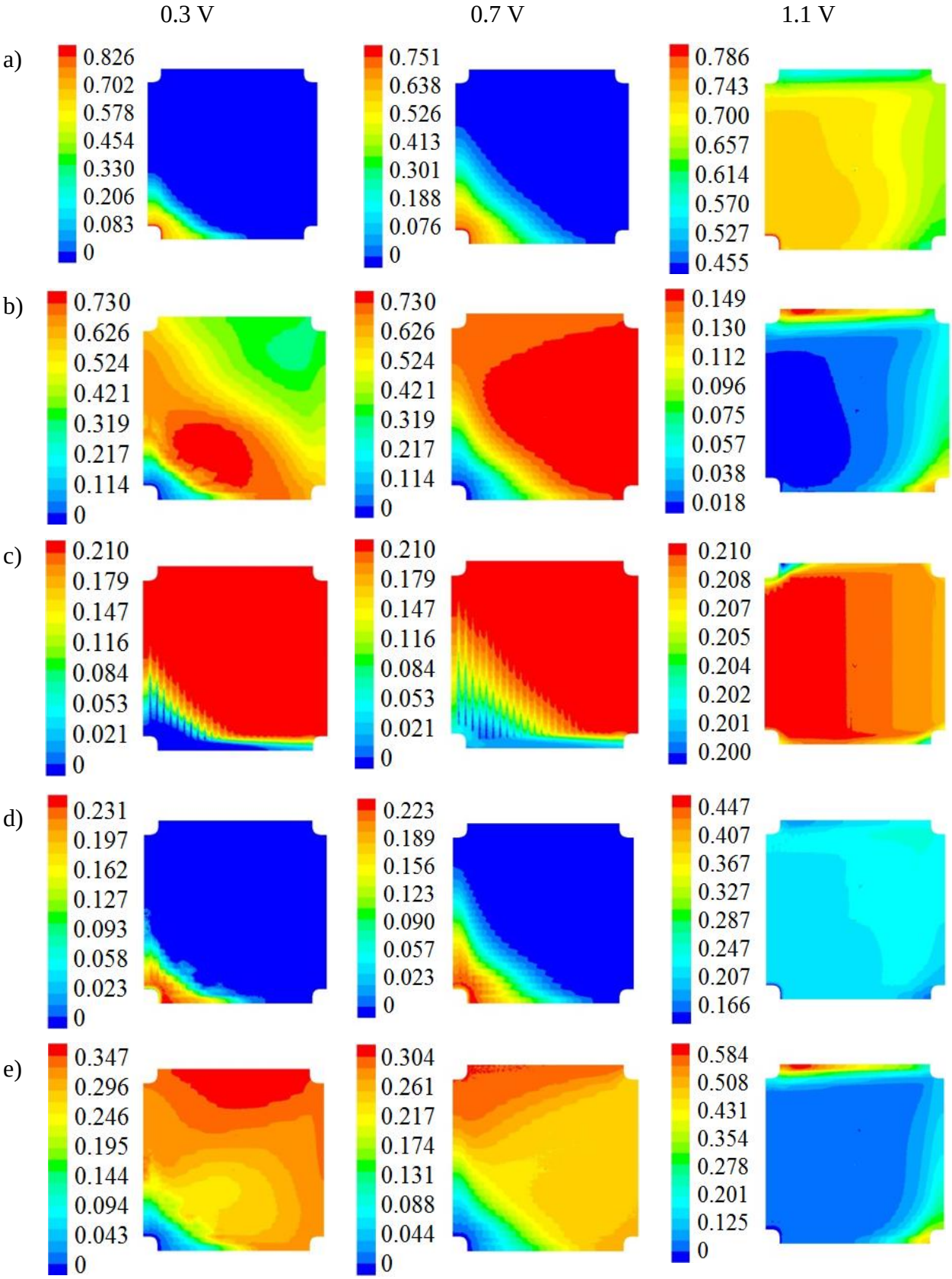

Therefore, the key parameter in the electrochemical analysis of the planar SOFC is temperature. Temperature distribution at the electrolyte from the anode side fuelled by syngas is shown in Table 4. The highest temperature was noticed at the lowest operating cell voltage of 0.3 V. This is likely due to the high concentrations of hydrogen and carbon monoxide at the inlet, which result in an increase in the electrochemical heat generation. Temperature distributions were highly non-uniform in the planar fuel cell and they differed quite significantly from each other for the operating voltage range values. Indication of hot spots was critical for the fuel cell safety reasons, because too high temperature gradients within the cell can lead to its damage.

The consumption rates of hydrogen, CO and oxygen as well as the formation rates of water and CO_2 affect the current density distributions presented in Table 5. Areas of the highest current density appear in the same regions where the highest formation rates were noticed.

Table 4. Distributions of temperature [K] at the electrolyte from the anode side of SOFC fed by syngas

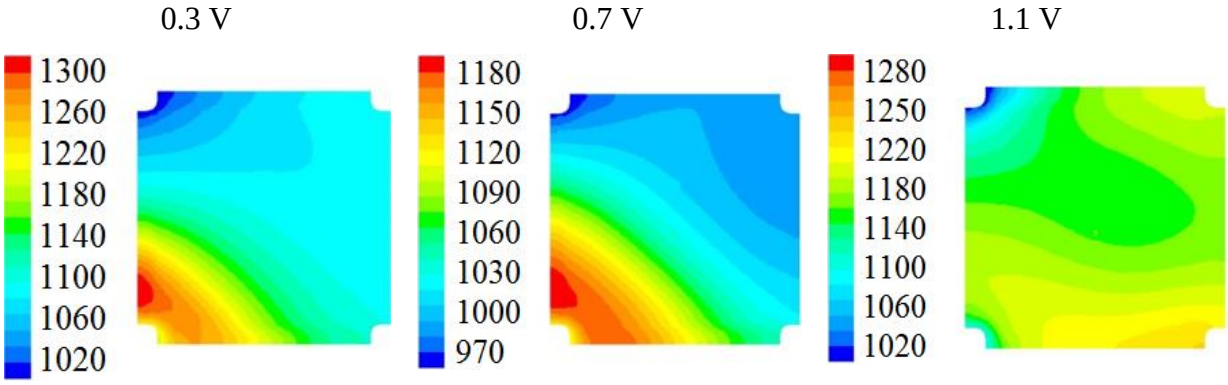

Table 5. Current density distributions [A/m^2] at the electrolyte from the cathode side of SOFC fed by syngas

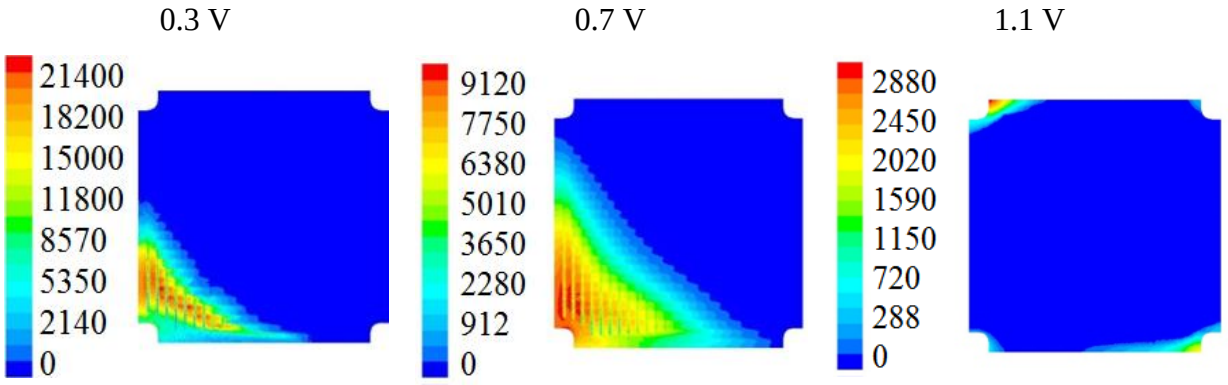

4. CONCLUSIONS

The presented modelling investigation was carried out to estimate the performance of the planar SOFC fuelled by a mixture of hydrogen and carbon monoxide and to provide a forecasting tool to predict fuel cell performance in relation to fuel composition changes. It was quantitatively shown that the fuel cell current density increased when the applied cell voltage decreased. The rule has been proven for the operating cell voltage of 1.1 V and 0.7 V, but then a sudden drop of the current value was noticed due

to probable lack of the fuel. In order to analyse the effect of fuel starvation as well as inlet concentrations of hydrogen and carbon monoxide further numerical studies need to be performed to estimate the impact of different feed compositions on SOFC performance. CFD results showed that the channel design plays an important role in the uniformity of mass fraction, temperature and current density distributions. It the areas where fuel was available, the fuel cell was electrochemically highly active and produced expected current at the applied voltage. In addition, it was demonstrated that the risk of hot spots decreased when a uniform distribution of mass fractions was assured. Therefore, providing a uniform distribution of the fuel cell operating parameters allows to reduce the risk of hot spots inside the fuel cell and as a consequence the fuel cell lifetime can be extended along with an increase of total power efficiency of the SOFC.

The research programme leading to these results received funding from the European Union's Seventh Framework Programme (FP7/2007-2013) for the Fuel Cells and Hydrogen Joint Undertaking (FCH JU) under grant agreement no [325323]. Information contained in the paper reflects only view of the authors. The FCH JU and the Union are not liable for any use that may be made of the information contained therein. The work was also financed from the Polish research funds awarded for the project No. 3043/7.PR/2014/2 of international cooperation within SAFARI in years 2014-2016.

SYMBOLS

F	Faraday's constant, C/mol
i	current density, A/m^2
i_0	effective exchange current density, A/m^2
n	number of electrons
R	universal gas constant, J/(kmolK)
T	absolute temperature, K

Greek symbols

α_{anode}	anodic transfer coefficient
$\alpha_{cathode}$	cathodic transfer coefficient
η_{act}	activation over-potential for H_2 and CO oxidation reaction or O_2 reduction reaction, V
ϕ_{cell}	electrical potential, V

Subscripts

an	anode
cat	cathode
CO	carbon monoxide
H₂	hydrogen
O₂	oxygen

REFERENCES

Andersson M., Yuan J., Sunden B., 2013, SOFC modeling considering hydrogen and carbon monoxide as electrochemical reactants. *J. Power Sources*, 232, 42-54. DOI: 10.1016/j.jpowsour.2012.12.122.

Barelli L., Bidini G., Cinti G., GAllorini F., Poniz M., 2017, SOFC stack coupled with dry reforming. *Appl. Energy*, 192, 498-507. DOI: 10.1016/j.apenergy.2016.08.167.

Bossel U., 2015, Small scale power generation for road trucks with planar SOFC system. *ECS Trans.*, 68, 1, 193-199. DOI: 10.1149/06801.0193ecst.

D'Andrea G., Gandiglio M., Lanzini A., Santarelli M., 2017, Dynamic model with experimental validation of a biogas-fed SOFC plant. *Energy Conversion and Management,* 135, 21-34. DOI: 10.1016/j.enconman.2016.12.063.

Gholaminezhad I., Paydar M. H., Jafarpur K., Paydar S., 2017, Multiscale mathematical modeling of methane-fueled SOFCs: predicting limiting current density using a modified Fick's model. *Energy Convers. Manage.*, 148, 222-237. DOI: 10.1016/j.enconman.2017.05.071.

Ho T. X., Kosinski P., Hoffman A. C., Vik A., 2009, Numerical analysis of a planar anode-supported SOFC with composite electrodes. *Int. J. Hydrogen Energy*, 34, 3488-3499. DOI: 10.1016/j.ijhydene.2009.02.016.

Iwai H., Yamamoto Y., Saito M., Yoshida H., 2011, Numerical simulation of intermediate temperature direct internal reforming planar solid oxide fuel cell. *Energy*, 36, 2225-2234. DOI: 10.1016/j.energy.2010.03.058.

Kang I., Kang Y., Yoon S., Bae G., Bae J., 2008, The operating characteristics of solid oxide fuel cells driven by diesel authothermal reformate. *Int. J. Hydrogen Energy*, 33, 21, 6298-6307. DOI: 10.1016/j.ijhydene.2008.07.123.

Papurello D., Iafrate Ch., Lanzini A. Santarelli M., 2017, Trace compounds impact on SOFC performance: experimental and modelling approach. *Appl. Energy*, 208, 637-654. DOI: 10.1016/j.apenergy.2017.09.090.

Park J., Li P, Bae J., 2012, Analysis of chemical, electrochemical reactions and thermo-fluid flow in methane feed internal reforming SOFCs: Part I – modeling and effect of gas concentrations. *Int. J. Hydrogen Energy*, 37, 10, 8512-8531. DOI: 10.1016/j.ijhydene.2012.02.110.

Pianko-Oprych P., Kasilova E., Jaworski Z., 2014, Quantification of the radiative and convective heat transfer processes and their effect on mSOFC by CFD modelling. *Polish J. Chem. Technol.*, 16, 2, 51-55. DOI: 10.2478/pjct-2014-0029.

Pianko-Oprych P. Zinko T., Jaworski Z., 2016, Simulation of the steady-state behaviour of a new design of a single planar Solid Oxide Fuel Cell. *Polish J. Chem. Technol.*, 18, 1, 64-71. DOI: 10.1515/pjct-2016-0011.

Razbani O., Assadi M., Andersson M., 2013, Three dimensional CFD modeling and experimental validation of an electrolyte supported solid oxide fuel cell fed with methane free biogas. *Int. J. Hydrogen Energy*, 38, 10068-10080. DOI: 10.1016/j.ijhydene.2013.05.153.

Stoeckl B., Subotic V., Reichholf D., Schroettner H., Hochenauer Ch., 2017, Extensive analysis of large planar SOFC: operation with humidified methane and carbon monoxide to examine carbon deposition based degradation. *Electrochim. Acta.* DOI: 10.1016/j.electacta.2017.09.026.

Tweedie M., Lemcoff N., 2014, CFD modeling and analysis of a planar anode supported intermediate temperature Solid Oxide Fuel Cell, *COMSOL conference*, Boston, USA, May 2014.

Received 10 November 2016
Received in revised form 17 October 2017
Accepted 03 November 2017

www.czasopisma.pan.pl www.journals.pan.pl
Chemical and Process Engineering 2017, 38 (4), 523-533
DOI: 10.1515/cpe-2017-0041

MATHEMATICAL MODELLING OF THERMAL AND FLOW PROCESSES IN VERTICAL GROUND HEAT EXCHANGERS

Sebastian Pater*, Włodzimierz Ciesielczyk

Cracow University of Technology, Department of Chemical and Process Engineering, Warszawska 24, 31-155 Kraków, Poland

The main task of mathematical modelling of thermal and flow processes in vertical ground heat exchanger (BHE-Borehole Heat Exchanger) is to determine the unit of borehole depth heat flux obtainable or transferred during the operation of the installation. This assignment is indirectly associated with finding the circulating fluid temperature flowing out from the U-tube at a given inlet temperature of fluid in respect to other operational parameters of the installation.

The paper presents a model of thermal and flow processes in BHE consisting of two analytical models separately-handling processes occurring inside and outside of borehole. A quasi-three-dimensional model formulated by Zeng was used for modelling processes taking place inside the borehole and allowing to determine the temperature of the fluid in the U-tube along the axis of BHE. For modelling processes occurring outside the borehole a model that uses the theory of linear heat source was selected. The coupling parameters for the models are the temperature of the sealing material on the outer wall of the borehole and the average heat flow rate in BHE. Experimental verification of the proposed model was shown in relation to BHE cooperating with a heat pump in real conditions.

Keywords: vertical ground heat exchanger, borehole, geothermal heat pumps, thermal and flow processes

1. INTRODUCTION

Under Polish conditions heating or cooling systems with so-called ground heat pumps often cooperate with a BHE (Wiśniewska and Forysiak, 2014). In vertical boreholes of depth from several tens to up to 200 m the single U-tube has been widely used. The empty space between the pipe and the wall of the borehole is filled with the sealing material. The heat transport medium flowing through the U-pipe extracts heat from the ground surrounding the borehole as well as from the groundwater (if present), and transports it to the refrigerant in an evaporator of the heat pump. If the heat pump works in cooling mode, the heat from the upper heat source is transmitted into the ground. Heat transport in BHE occurs by convection from the fluid to the wall of the U-tube and subsequently by sealing of the borehole to the ground mainly by conduction. In the areas of active groundwater exchange this process takes place also by convection.

The main task of mathematical modelling of thermal and flow processes in BHE is to determine the unit of borehole depth heat flux obtainable or transferred during the work of the installation (Kozioł, 2012). The analytical models describing the processes occurring in BHE most commonly separately examine the phenomena arising inside and outside the borehole (Rees, 2016; Salimshirazi, 2012).

*Corresponding authors, e-mail: sebapater@chemia.pk.edu.pl

The main area of modelling thermal and flow processes inside BHE is to determine the fluid temperature at the inlet and outlet of the U-tube, depending on temperature of the borehole wall and mass flow rate of a fluid, with the assumed physicochemical data of fluid, sealing material and U-tube pipe (Koohi-Fayegh and Rosen, 2014). For a rough computational analysis a simplified one-dimensional model shown at work (Gu and O'Neal., 1998) can be used. This model omits the axial changes of borehole material, heat capacity and also thermal interaction between the circulating medium flowing in U-tube. Hellström (1991) developed an analytical solution of thermal resistance between the pipes in U-tube in the cross-section perpendicular to the axis of the borehole. On the basis of this model a quasi-three-dimensional model formulated by Zeng (Zeng et al., 2003) was created, which takes into account temperature changes of the fluid along the axis of the borehole with neglected axial heat conduction.

One of the first analytical models for a quantitative description of the thermal and flow processes outside BHE was a model using the theory of linear heat source (Kelvin's line source) presented in (Ingersoll and Plass, 1948). In this model, soil is treated as a medium with an initial uniform temperature in the entire volume and the borehole with the U-tube is assumed to be an infinite line source. In the cylindrical source model (Wołoszyn, 2014) the borehole is considered as an infinite cylinder surrounded by a homogeneous material with properties being constant over time. Eskilson (1987) presented a model that takes into account the axial changes of ground temperature with time and depth. The temperature distribution on the outer wall of the borehole BHE was determined as so-called "*g*" function which represents a specific configuration of the boreholes (Rees, 2016). The finite line source model developed by Zeng's team (Zeng et al., 2002) uses the model proposed by Eskilson. The temperature distribution in the borehole can be obtained by solving analytical equations. Integration of these equations is faster than numerically solving this problem (Zeng et al., 2002).

In recent years, thanks to increased computing capacity, numerical models of thermal and flow processes in BHE are dynamically developing (Yang et al., 2010). These models offer the possibility to include, among others, heat flow inside and outside the borehole, the spatial changes of physicochemical properties of soil and sealing material of the borehole, interaction between the boreholes in BHE and also changes of boundary conditions in time and space (Wołoszyn, 2014). Due to the high slenderness ratio of BHE (small diameter compared to length) and a large number of elements in three-dimensional mesh calculations carried out in the simulation programs can be extremely time consuming. Publications by Śliwa et al. (2005, 2011, 2012) should also be mentioned.

Performing computations using numerical models despite the fact that they may offer a high degree of flexibility and accuracy is not justified if there is no reliable information on the physicochemical properties of the soil surrounding the borehole (Kozioł, 2012). Analytical models of thermal and flow processes in BHE are developed mainly for practical reasons, because they allow to perform calculations in a quick and relatively simple way in comparison to numerical models (Yang et al., 2010).

The paper presents a model of thermal and flow processes in BHE consisting of two analytical models separately handling processes occurring inside and outside of the borehole. For modelling processes taking place inside the borehole a quasi-three-dimensional model formulated by Zeng (Zeng et al., 2003) was used, which:

- allows determining the temperature of the fluid in the U-tube along the axis of BHE,
- takes into account the heat exchange between the pipes which are being arranged symmetrically in a borehole,
- assumes identical temperature on the external wall of borehole along its axis, which however can vary with time,
- assumes a homogeneous structure of the ground material and the sealing of the borehole, whose physicochemical properties are independent of temperature (Zeng et al., 2003).

The model does not take into account heat conducted in axial direction, heat transferred by convection from the groundwater and the phase transition of the moisture in the borehole sealing.

For modelling processes occurring outside the borehole a model that uses the theory of linear heat source (Ingersoll, 1948) was selected. It assumes:

- initial uniform temperature of soil (so called undisturbed ground temperature) and constant thermo-physical parameters in the entire volume,
- one-dimensional heat conduction without heat conduction in the axial direction (also from the surface above and below of the borehole),
- heat exchange between the outer wall of borehole and the surrounding soil.

The coupling parameters for models are the temperature of the sealing material on the outer wall of the borehole and the average heat flow rate in BHE. The average heat flow rate at specified intervals remains constant, but may vary between these intervals.

2. MODEL OF THERMAL AND FLOW PROCESSES IN BHE

Energy balance equations for the fluid flowing up and down in the U-tube (Zeng et al., 2003) were formulated as (1) and (2):

$$-\dot{m}_s c_s \frac{dT_{f1}}{dz} = \frac{T_{f1} - T_b}{R_1^{\Delta}} + \frac{T_{f1} - T_{f2}}{R_{12}^{\Delta}} \tag{1}$$

$$\dot{m}_s c_s \frac{dT_{f2}}{dz} = \frac{T_{f2} - T_b}{R_2^{\Delta}} + \frac{T_{f2} - T_{f1}}{R_{12}^{\Delta}} \tag{2}$$

Expressions R_1^{Δ}, R_2^{Δ} and R_{12}^{Δ} are calculated from Eqs. (3, 4, 5):

$$R_1^{\Delta} = \frac{R_{11}R_{22} - R_{12}^2}{R_{22} - R_{12}} \tag{3}$$

$$R_2^{\Delta} = \frac{R_{11}R_{22} - R_{12}^2}{R_{11} - R_{12}} \tag{4}$$

$$R_{12}^{\Delta} = \frac{R_{11}R_{22} - R_{12}^2}{R_{12}} \tag{5}$$

R_{11} and R_{22} represent a thermal resistance between the wall of the borehole and the fluid. R_{12} is the thermal resistance between the flowing fluids in the pipes (Fig. 1). Because the pipes in the borehole are located symmetrically it is assumed that $R_{11} = R_{22}$.

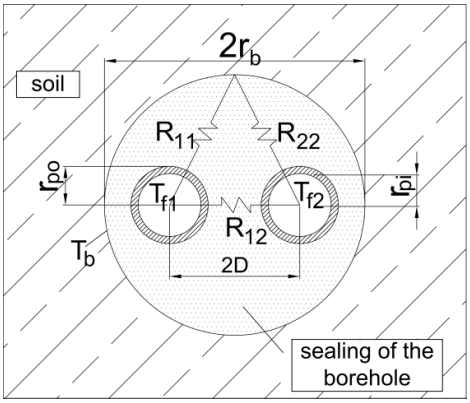

Fig. 1. The cross-section of borehole with U-tube

Hellstrom (1991) specified Eqs. (6) and (7) describing the thermal resistances R_{11} and R_{12} as follows:

$$R_{11} = \frac{1}{2\pi k_b}\left[\ln\left(\frac{r_b}{r_{po}}\right) + \frac{k_b - k_g}{k_b + k_g}\cdot\ln\left(\frac{r_b^2}{r_b^2 - D^2}\right)\right] + R_p \tag{6}$$

$$R_{12} = \frac{1}{2\pi k_b}\left[\ln\left(\frac{r_b}{2D}\right) + \frac{k_b - k_g}{k_b + k_g}\cdot\ln\left(\frac{r_b^2}{r_b^2 + D^2}\right)\right] \tag{7}$$

The value of the thermal resistance R_p from fluid to the outer pipe surface is determined (Zhang et al., 2015) from Eq. (8) as:

$$R_p = \frac{1}{2\, r_{pi}\pi h} + \frac{\ln\left(r_{po}/r_{pi}\right)}{2\,\pi k_p} \tag{8}$$

The coefficient h_f was estimated from Dittus-Boelter correlation (9):

$$h = 0.0115\,\mathrm{Re}^{0.8}\,\mathrm{Pr}^{n}\,\frac{k_f}{r_{pi}} \tag{9}$$

Depending on the operating mode of the heat pump factor n takes a value 0.40 for heating and 0.33 for cooling mode. To solve the energy balance Eqs. (1) and (2), the following boundary conditions were assumed (10):

$$\left.\begin{aligned} z = 0, \quad & T_{f1} = T_f^{'} \\ z = H, \quad & T_{f1} = T_{f2} \end{aligned}\right\} \tag{10}$$

Using the Laplace transform (Zeng et al., 2003) the solutions of Eqs. (1) and (2) are given by Eqs. (11) and (12):

$$\Theta_1(Z) = \cosh(\beta Z) - \frac{1}{\sqrt{1-P^2}}\left[1 - P\,\frac{\cosh(\beta) - \sqrt{\dfrac{1-P}{1+P}}\sinh(\beta Z)}{\cosh(\beta) + \sqrt{\dfrac{1-P}{1+P}}\sinh(\beta)}\right]\sinh(\beta Z) \tag{11}$$

$$\begin{aligned}\Theta_2(Z) = {} & \frac{\cosh(\beta) - \sqrt{\dfrac{1-P}{1+P}}\sinh(\beta)}{\cosh(\beta) + \sqrt{\dfrac{1-P}{1+P}}\sinh(\beta)}\cosh(\beta Z) + \\ & + \frac{1}{\sqrt{1-P^2}}\left[1 - P\,\frac{\cosh(\beta) - \sqrt{\dfrac{1-P}{1+P}}\sinh(\beta)}{\cosh(\beta) + \sqrt{\dfrac{1-P}{1+P}}\sinh(\beta)} - P\right]\sinh(\beta Z)\end{aligned} \tag{12}$$

Dimensionless coefficients used in Eqs. (11) and (12) are defined by:

$$\Theta = \frac{T_f(z) - T_b}{T_f^{'} - T_b} \tag{13}$$

$$\beta = \frac{H}{\dot{m} c_s \sqrt{(R_{11} + R_{12})(R_{11} - R_{12})}} \tag{14}$$

$$Z = \frac{z}{H} \tag{15}$$

$$P = \frac{R_{12}}{R_{11}} \tag{16}$$

The ground temperature depending on the distance from the linear heat source and time, for the average heat flux (Fang et al., 2002) is calculated from Eq. (17):

$$T_g(r,t) = T_\infty + \frac{\bar{q}}{4\pi H k_g}\,\mathrm{Ei}\left(\frac{r^2}{4t\alpha}\right) \tag{17}$$

The exponential integral in Eq. (17) can be approximated (Fang et al., 2002) by Eq. (18):

$$\mathrm{Ei}\left(\frac{r^2}{4t\alpha}\right) = \ln\left(\frac{4t\alpha}{r^2}\right) - \gamma \tag{18}$$

Under real conditions a value of the heat exchanged in BHE varies with time due to e.g. different demand for heating or cooling for industrial process or in the building construction. In order to apply the model under considerations to predict the operating parameters of BHE under varying conditions it must be assumed that at certain intervals the heat flux remains constant, while between these intervals, this heat flux may change. Using the technique of superposition (Fang et al., 2002) increase or decrease of the soil temperature can be determined from Equation (19):

$$T_g(r,t) = T_\infty + \sum_{i=1}^{n} \frac{(\bar{q}_i - \bar{q}_{i-1})}{4\pi H k_g}\left[\ln\left(\frac{4\alpha(t_n - t_{i-1})}{r^2}\right) - \gamma\right] \tag{19}$$

Precision of calculations based on Eq. (19) is dependent on the length of assumed intervals. If the value $5r_b^2/\alpha$ is smaller than the length of the time interval, the error of estimation of the soil temperature with respect to the accurate model (e.g. numerical model) and a model of a linear heat source is less than 10% (Salimshirazi, 2012). Increasing the time interval to a value greater than $20r_b^2/\alpha$, reduces the error to about 3% (Salimshirazi, 2012).

The coupling parameters for the models are the temperature of the sealing material on the outer wall of the borehole and the average heat flow rate in the BHE in a specified time interval. The calculation algorithm proposed in (Koohi-Fayegh and Rosen, 2014) is based on determining the soil temperature T_g from the linear source model for a given heat flux $\bar{q}$ in the time interval and distance from the source equal to r_b. Knowing the temperature T_b it is possible to determine T_{f2} using Eq. (20):

$$T_{f2}(0) = T_b + (T_f^{'} - T_b)\Theta_2(0) \tag{20}$$

Equation (12) simplifies to the form (21):

$$\Theta_2(0) = \frac{\cosh(\beta) - \sqrt{\dfrac{1-P}{1+P}}\sinh(\beta)}{\cosh(\beta) + \sqrt{\dfrac{1-P}{1+P}}\sinh(\beta)} \tag{21}$$

In Eq. (20) the temperature $T_f^{'}$ can be determined from Eq. (22):

$$T_f^{'} = T_{f2}(0) - \frac{\bar{q}}{\dot{m}_s c_s} \tag{22}$$

By combining Eqs. (20) and (22), Eqs. (23) and (24) were obtained enabling to calculate $T_f^{'}$ and $T_{f2}(0)$ in a given time step:

$$T_f^{'} = T_b - \frac{\bar{q}}{\dot{m}_s c_s \left[1 - \Theta_2(0)\right]} \tag{23}$$

$$T_{f2}(0) = T_b - \frac{\bar{q}\Theta_2(0)}{\dot{m}_s c_s \left[1 - \Theta_2(0)\right]} \tag{24}$$

Because the proposed model is intended for an analysis including a variable heating and cooling load of a building or installation within a year, as well as varying degrees of this load coverage by a heat pump, the value of the average heat flux at a given time interval for a different operating mode of the heat pump is determined from Eqs. (25) and (26):

$$\bar{q} = \frac{\left(Q_k - \frac{Q_k}{\mathrm{SPF}}\right)\phi}{t_k} \tag{25}$$

$$\bar{q} = -\frac{Q_{k,C}\phi}{t_k} \tag{26}$$

3. EXPERIMENTAL VERIFICATION OF MODEL

Experimental verification of the proposed model was shown in relation to BHE cooperating in real conditions with a compressor brine-water heat pump. The heat pump heating output was approx. 10 kW and the cooling output approx. 3 kW (in passive cooling mode). In the BHE three boreholes, each of which had a depth of 70 meters, were installed. The boreholes were made in one line, with seven meter intervals and six meters away from the northern wall of the building. In each borehole, a single polyethylene U-tube was mounted. The intermediate fluid which transmitted energy from the ground to the evaporator was aqueous propylene glycol solution.

Below 4 m in depth the soil surrounding the boreholes in the BHE was made of clays with low water permeability. In addition, by maintaining an appropriate distance between the boreholes limiting their thermal interaction, in the further part of the article heat-flow processes were considered for only one single borehole in BHE.

Table 1 presents the physicochemical properties of materials used in BHE and other data. Table 2 shows calculated values of the necessary parameters for the model verification. The value of T_∞ was determined based on the paper by Fidorów and Szulgowska-Zgrzywa (2015) in which the real temperature values of the soil surrounding BHE in the Polish climate were presented.

Table 1. The physicochemical properties of the materials used in single borehole and other data

Parameter	Value	Parameter	Value	Parameter	Value
H [m]	70	r_b [m]	0.0675	δ_s [kg/m^3]	1 045
D [m]	0.0338	r_{pi} [m]	0.0163	c_g [J/(kg·K)]	800
k_b [W/(m·K)]	1.000	r_{po} [m]	0.0200	c_s [J/(kg·K)]	3 636
k_f [W/(m·K)]	0.385	T_∞ [K]	285.15	μ_s [kg/(m·s)]	0.00935
k_g [W/(m·K)]	2.200	δ_g [kg/m^3]	1 800	$\dot{m}_s$ [kg/s]	0.198
k_p [W/(m·K)]	0.400				

Table 2. The calculated values of the necessary parameters for model verification

Parameter	Value	Parameter	Value
h [W/(m^2·K)]	351.9 (for heating) 257.2 (for cooling)	R_p [m·K/W]	0.109 (for heating) 0.119 (for cooling)
α [m^2/s]	1.53×10^{-6}	P [-]	0.0406 (for heating) 0.0406 (for cooling)
R_{11} [m·K/W]	0.318 (for heating) 0.328 (for cooling)	β [-]	0.306 (for heating) 0.296 (for cooling)
R_{12} [m·K/W]	1.33×10^{-2}	$\Theta_2(0)$ [-]	0.557 (for heating) 0.567 (for cooling)

Verification of the proposed model was conducted by determining the temperature of the brine flowing out from the U-tube at a given temperature of the fluid flowing into the U-tube for the time interval equal to 6 h. Due to the fact that in the considered installation the time of continuous operation of the heat pump usually does not exceed a few hours, only for over a dozen days in several years of heat pump operation data were available and used for further calculations.

Figure 1 shows measured changes of fluid temperature at the inlet and the outlet of U-tube on 16 February 2012 during the operation of the heat pump in heating mode. Figure 3 presents theoretical changes of fluid temperature at the inlet and the outlet of U-tube on 16 February 2012. The theoretical change of fluid temperature in U-tube was determined from 6.00 to 12.00 and was equal to 3.39 ºC. The average experimental temperature difference of fluid at the inlet and the outlet of BHE (dotted rectangle in Fig. 2) was 3.48 ºC. The absolute value of the relative error of the determination of the fluid temperature difference was 2.6%.

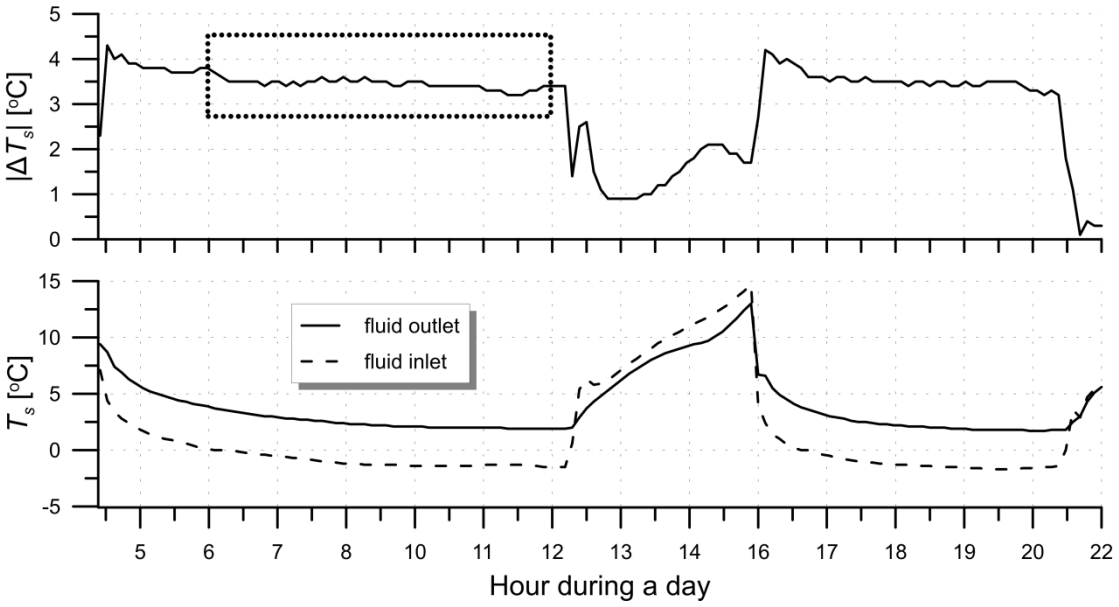

Fig. 2. Experimental changes of fluid temperature in inlet and outlet of U-tube on 16 February 2012

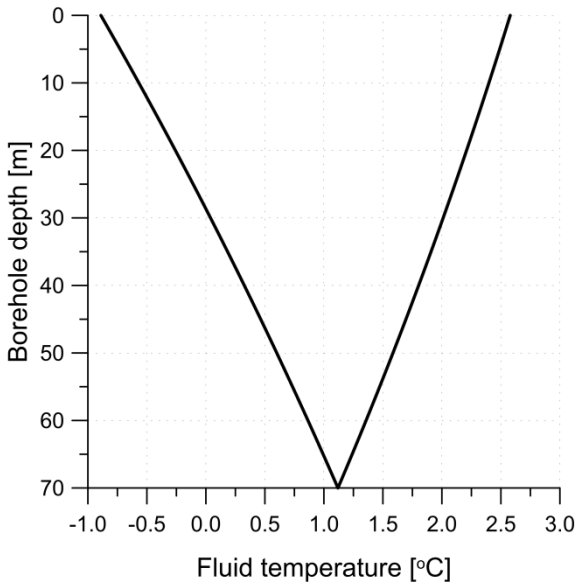

Fig. 3. Theoretical changes of fluid temperature in U-tube on 16 February 2012

The described procedure was carried out for several time periods in different years of BHE operation. For given time intervals the real average temperature difference of the fluid at the inlet and the outlet of the U-tube in BHE (Fig. 4) was determined. Then, using the developed mathematical model the temperature of soil on the inner surface of borehole and the fluid temperature at the outlet of U-tube was calculated. The absolute value of the relative error calculated theoretically does not exceed 16% of the measured value.

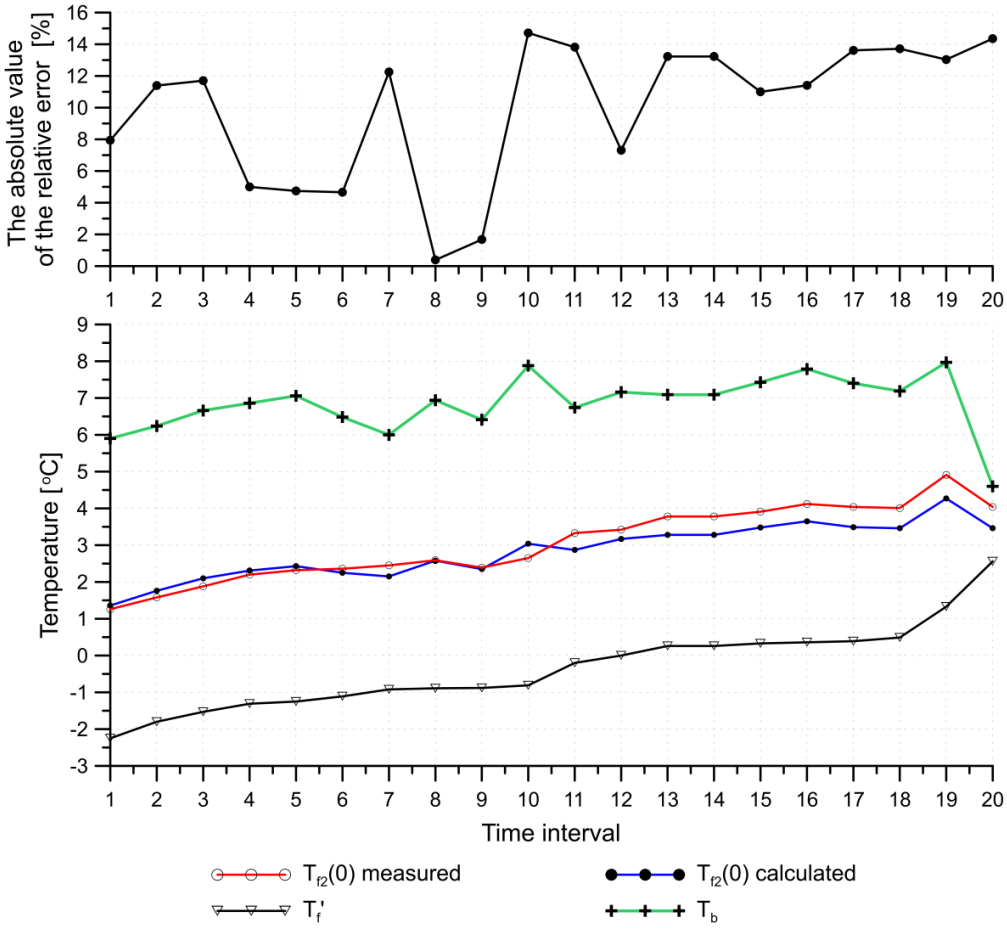

Fig. 4. Comparison of theoretical calculations with measurement data

4. CONCLUSIONS

The proposed model of the thermal and flow processes in BHE allows to perform analyses involving long-term cooperation of the heat pump with BHE during heating seasons, the natural thermal regeneration of soil, regeneration of soil by accumulating the heat from the cooling process, as well as supplied from e.g. solar collectors, variable heating and cooling load of a building over the years and different degree of coverage of the heat demand for the building by the heat pump. The model allows to perform calculations related to the BHE in a relatively simple and quick way compared with numerical models. By using equations possible to be analytically solved obtaining the results of multivariate simulations of the operating conditions does not take much time.

Since the model does not take into account the thermal interaction between multiple boreholes which are in close proximity, its use is limited to a single borehole BHE. This model can be used for analysis of BHE with more boreholes if:

- in BHE the minimum distances between the boreholes which limit their thermal interaction are maintained,
- they are of equal depth,
- the ground surrounding the boreholes is additionally characterised by low permeability.

Experimental verification of the model proved that it is quantitatively in good agreement with experiments. Calculations were performed on a computer with an AMD Turion X2 Ultra clocked at 2.20 GHz, 3 GB of RAM and a graphics card Radeon HD 3450. Calculation of the soil temperature at a distance $r = r_b$ for 1216 time intervals lasting 24 h has been done in Microsoft Excel in a few seconds.

SYMBOLS

c	specific heat of the fluid, J/(kg·K)
D	distance between the pipes in a borehole, m
Ei	exponential integral
h	coefficient of heat transfer from the brine to the surface of the pipe, W/(m^2·K)
H	depth of the borehole, m
k	thermal conductivity, W/(m·K)
$\dot{m}$	mass flow rate, kg/s
n	coefficient depending on the operating mode of the heat pump
P	dimensionless coefficient
Pr	Prandtl number
$\bar{q}$	average heat flux, W
Q	amount of heat exchanged, J
r	radius, m
Re	Reynolds number
t	time, s
T	temperature, K
z	coordinate axis, m
Z	dimensionless coefficient
A	constant

Greek symbols

α	soil thermal diffusivity, m^2/s
β	dimensionless coefficient

γ	Euler–Mascheroni constant
ΔT	temperature difference, K
Θ	dimensionless temperature of the fluid
ϕ	coverage of demand for heating or cooling by heat pump in the time interval

Superscripts

‘	inlet

Subscripts

1	fluid flowing down in U-tube
2	fluid flowing up in U-tube
b	outer wall of borehole
c	cool
g	soil surrounding the borehole
f	fluid
k	time interval
m	material filling the borehole
p	pipe wall
pi	inner wall of the pipe in a borehole
po	outer wall of the pipe in a borehole
s	fluid in U-tube
∞	undisturbed ground

Abbreviations

SPF	Seasonal Performance Factor of Heat Pump
BHE	Borehole Heat Exchanger

REFERENCES

Eskilson P., 1987. *Thermal analysis of heat extraction boreholes*. PhD thesis, University of Lund, Sweden.

Fang Z., Diao N., Cui P., 2002. Discontinuous operation of geothermal heat exchangers. *Tsinghua Sci. Technol*., 7, 194-201.

Fidorów N., Szulgowska-Zgrzywa M., 2015. The influence of the ground coupled heat pump's labor on the ground temperature in the boreholes – Study based on experimental data. *Appl. Therm. Eng.*, 82, 237-245. DOI: 10.1016/j.applthermaleng.2015.02.035.

Gu Y., O'Neal D. L., 1998. Development of an equivalent diameter expression for vertical U-Tubes used in ground-coupled heat pumps. *ASHRAE Trans.*, 104, 347–55.

Hellstrom G., 1991. *Ground heat storage: Thermal analyses of duct storage systems*. PhD thesis, University of Lund, Sweden.

Ingersoll L.H., Plass H.J., 1948. Theory of the ground pipe heat source for the heat pump. *ASHVE Trans*., 47, 339–348.

Koohi-Fayegh S., Rosen M., 2014. An analytical approach to evaluating the effect of thermal interaction of geothermal heat exchangers on ground heat pump efficiency. *Energ. Convers. Manage.*, 78, 184-192. DOI: 10.1016/j.enconman.2013.09.064.

Kozioł J., 2012. *Przegląd uwarunkowań i metod oceny efektywności wykorzystania odnawialnych źródeł energii w budownictwie*. Wydawnictwo Politechniki Śląskiej, Gliwice.

Rees S., 2016. *Advances in ground-source heat pump systems*. Woodhead Publishing, Duxford.

Salimshirazi A., 2012. *Transient heat transfer in vertical ground heat exchanger*. PhD thesis, Polytechnique Montreal, Canada.

Śliwa T., Gonet A., 2005. Theoretical model of borehole heat exchanger. *J. Energy Resour. Technol*., 127, 142-148. DOI:10.1115/1.1877515.

Śliwa T., Gonet A., 2011. Analiza efektywności wymiany ciepła w wymiennikach otworowych o różnej konstrukcji. *Wiertnictwo Nafta Gaz*, 28, 555-570.

Śliwa T., Gołaś A., Wołoszyn J., Gonet A. (2012). Numerical model of borehole heat exchanger in ANSYS CFX software. *Arch. Min. Sci.*, 57, 375–390. DOI 10.2478/v10267-012-0024-3.

Wołoszyn J., 2014. *Badania wpływu rozmieszczenia wymienników na efektywność podziemnych magazynów energii*. PhD thesis, AGH University of Science and Technology, Poland.

Wiśniewska M., Forysiak J., 2014. Źródła ciepła niskotemperaturowego dostępnego dla gruntowych pionowych wymienników ciepła. Uwarunkowania środowiskowe i techniczne. *Acta Universitatis Lodziensis, Folia Geographica Physica*, 13, 65-77.

Yang H., Cui P., Fang Z., 2010. Vertical-borehole ground-coupled heat pumps: A review of models and systems. *Appl. Energy*, 87, 16-27. DOI: 10.1016/j.apenergy.2009.04.038.

Zeng H., Diao N., Fang Z., 2002. A finite line-source model for boreholes in geothermal heat exchangers. *Heat Tran. Asian. Res.*, 31, 558-567. DOI: 10.1002/htj.10057.

Zeng H., Diao N., Fang Z., 2003. Efficiency of vertical geothermal heat exchangers in the ground source heat pump system. *J. Thermal Sci.*. 12, 77-81. DOI: 10.1007/s11630-003-0012-1.

Zhang C., Chen P., Liu Y., Sun S., Peng D., 2015. An improved evaluation method for thermal performance of borehole heat exchanger. *Renew. Energy*, 77, 142-151. DOI: 10.1016/j.renene.2014.12.015.

Received 14 September 2016
Received in revised form 06 November 2017
Accepted 10 November 2017

www.czasopisma.pan.pl www.journals.pan.pl
Chemical and Process Engineering 2017, 38 (4), 535-541
DOI: 10.1515/cpe-2017-0042

THE INFLUENCE OF SUPERCRITICAL FOAMING CONDITIONS ON PROPERTIES OF POLYMER SCAFFOLDS FOR TISSUE ENGINEERING

Katarzyna Kosowska, Marek Henczka*

Warsaw University of Technology, Faculty of Chemical and Process Engineering, Waryńskiego 1, 00-645 Warsaw, Poland

The results of experimental investigations into foaming process of poly(ε-caprolactone) using supercritical CO_2 are presented. The objective of the study was to explore the aspects of fabrication of biodegradable and biocompatible scaffolds that can be applied as a temporary three-dimensional extracellular matrix analog for cells to grow into a new tissue. The influence of foaming process parameters, which have been proven previously to affect significantly scaffold bioactivity, such as pressure (8-18 MPa), temperature (323-373 K) and time of saturation (1-6 h) on microstructure and mechanical properties of produced polymer porous structures is presented. The morphology and mechanical properties of considered materials were analyzed using a scanning electron microscope (SEM), x-ray microtomography (μ-CT) and a static compression test. A precise control over porosity and morphology of obtained polymer porous structures by adjusting the foaming process parameters has been proved. The obtained poly(ε-caprolactone) solid foams prepared using $scCO_2$ have demonstrated sufficient mechanical strength to be applied as scaffolds in tissue engineering.

Keywords: supercritical fluids, supercritical foaming, poly(ε-caprolactone), tissue engineering, scaffold

1. INTRODUCTION

Bone defects being the result of injuries or diseases are a serious problem posing enormous challenge for modern regenerative medicine. The development of methods aiming at regeneration of damaged tissue, as opposed to their replacement, is an alternative to surgical therapy (Gloria et al., 2012). Tissue engineering is an interdisciplinary, rapidly evolving area of research which draws upon materials engineering, chemistry, biology and medicine (Tarabasz and Henczka, 2016). In recent years the development of modern technologies has been mainly focused on the advancement in research of innovative, efficient, cost-effective and environmentally safe methods of the production of functional porous structures. New products may be useful for a wide range of applications, for example as biodegradable scaffolds for the culture of bone cells (Curia et al., 2015; Gualandi et al., 2010; Karimi et al., 2012; Kweon et al., 2003). There are numerous production methods of polymer porous materials applicable to biomedical practices, such as solvent casting-particle leaching, thermally induced phase separation, injection molding, extrusion, foaming and electrospinning (Guan et al., 2005). Some of these techniques require processing of the polymer material at relatively high temperature, which prevents embodiment of thermosensitive compounds, such as medicaments or growth factors into foam structure during the production process (Liao et al., 2012; Markočič et al., 2013; Tsivintzelis et al., 2006; Tsivintzelis et al., 2007).

The polymer foaming process with the use of supercritical fluids is an alternative to traditional methods of production of functional porous structures, carried out with the application of environmentally

*Corresponding authors, e-mail: Marek.Henczka@pw.edu.pl

harmful, volatile organic solvents, which may also lead to a reduction in the activity of processed biodegradable polymers (Gualandi et al., 2010; Tayton et al., 2012). The exercitation of a safe medium such as supercritical carbon dioxide in the process allows to eliminate the above mentioned disadvantages. Supercritical carbon dioxide ($scCO_2$) is the most commonly used supercritical fluid, possessing such attributes as moderate values of critical parameters, chemical passivity, non-flammability, non-toxicity, wide availability and low cost (Nalawade et al., 2006). Its unique characteristics, such as gas like low kinematic viscosity, liquid like density, high compressibility and pressure-dependent solubility of various substances, are beneficial for applications of $scCO_2$ in industrial technologies (Curia et al., 2015; Guan et al., 2005; Karimi et al., 2012). Carbon dioxide applied as a supercritical process medium can be easily removed from porous products simply by depressurization. However, it should be mentioned that in some cases the contact of polymer material with supercritical carbon dioxide may lead to unfavorable changes in its structure and properties (Tarabasz et al., 2016). Poly(ε-caprolactone) (PCL) is a polymer commonly used in tissue regenerative engineering. It is a biodegradable aliphatic semi-crystalline polyester of a low melting temperature of about 333 K (Curia et al., 2015; Guan et al., 2005; Karimi et al., 2012; Kweon et al., 2003). In the foaming process of PCL using $scCO_2$ one can distinguish the following stages: melting and saturating the polymeric material with $scCO_2$ at appropriate parameters, cooling and depressurization of saturated polymer matrix, and finally nucleation and growth of gas cells which leads to formation of the final porous structure (Gualandi et al., 2010; Jacobs et al., 2007; Karimi et al., 2012; Reverchon et al., 2008). The course of these stages strongly affects the final properties of the obtained porous structures, which must meet certain specific characteristics when applied as scaffolds. In particular, appropriate pore size, sufficient porosity and defined mechanical properties are considered to be fundamental parameters in the field of tissue engineering and they should be accustomed to the type of regenerated tissue (Gloria et al., 2012; Gualandi et al., 2010; Guan et al., 2005; Karimi et al., 2012; Markočič et al., 2013). Pertinent control of the properties of produced scaffolds is executed with the appropriate definition of the foaming process parameters and with the use of adequate composite materials.

The purpose of this work was to identify the effect of supercritical foaming process parameters on the properties of obtained poly(ε-caprolactone) porous structures and to establish the key features affecting their usability for bone tissue engineering. In particular, the effects of pressure, temperature and time of $scCO_2$ polymer saturation on 3D microstructure and mechanical properties of the polymer porous product are presented.

2. METHODS

Commercially available poly(ε-caprolactone) in form of pellets (D~ 3 mm) with Mn = 80,000 manufactured by Sigma Aldrich (Italy) was used as a model polymeric material. The melting temperature and density of the material was equal to 333 K and 1.19 g/cm3, respectively. Carbon dioxide (purity of 4.5) was purchased from Linde Gaz (Poland) and used in experiments as the foaming agent. In the first part of experimental investigations, $scCO_2$ - based foaming polymer process was carried out. A scheme of experiment setups including a $scCO_2$ pump, a high pressure cell and a process parameter control unit was reported previously (Tarabasz and Henczka, 2016). The foaming experiments were conducted using the procedure presented subsequently. The high pressure cell was filled with 1.5 g of polymer, which was melted, contacted and saturated with $scCO_2$ in batch mode. This stage of the process was carried out in the following conditions: temperature in the range of 323 - 373 K, pressure 8 - 18 MPa, and saturation time of 1 - 6 h. Consecutively, the carbon dioxide-polymer mixture was cooled to 298 K, kept over 30 min under a constant pressure and finally rapidly decompressed to atmospheric pressure. In the second part of experiments the morphology and mechanical properties of obtained porous structures were identified. Scanning electron microscope (SEM) examination and x-ray microtomography (μ-CT) were applied in the analysis of the

microstructure of the produced polymer porous materials. The morphology of side surface and cross-section fracture of the porous structure at different magnifications was analyzed with the use of Phenom scanning electron microscope SEM (FEI COMPANY, Netherlands). The samples were first sectioned using a stainless steel scalpel and then a coat of gold was applied for 2 min in argon atmosphere with the use of EMITECH K550X sputter coater (Quorum Technologies, Warsaw). The porosity and the interconnectivity of the pores were evaluated with the use of microtomography X-ray scanning (μ-CT, SkyScan 1172, Bruker). Static compression tests to evaluate the mechanical properties of the polymer foams were conducted using the universal testing machine Instron 5566 (Instron, USA). Prior to the compression testing, the obtained structures were cut into cuboids of identical dimensions: 5.0 mm×5.0 mm×10.0 mm. The Young's modulus and compression strength of solid foams were determined on the basis of stress–strain profiles.

3. RESULTS AND DISCUSSION

Scanning electron microscope examination allowed the identification of the microstructure of polymer porous materials obtained under different foaming process conditions. In Fig. 1a and Fig. 1b the effect of experimental conditions on morphology of solid - gas structures is presented. The microstructure of foam strongly depends on the process parameter.

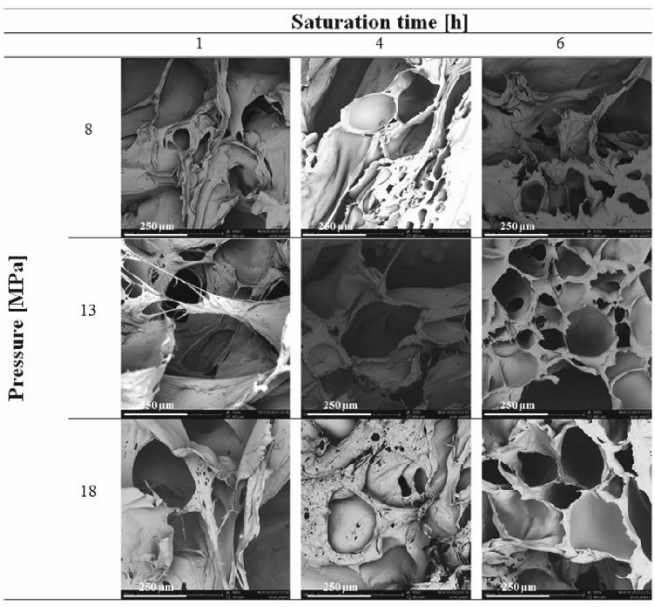

Fig. 1a. Effect of saturation time on morphology of porous structures

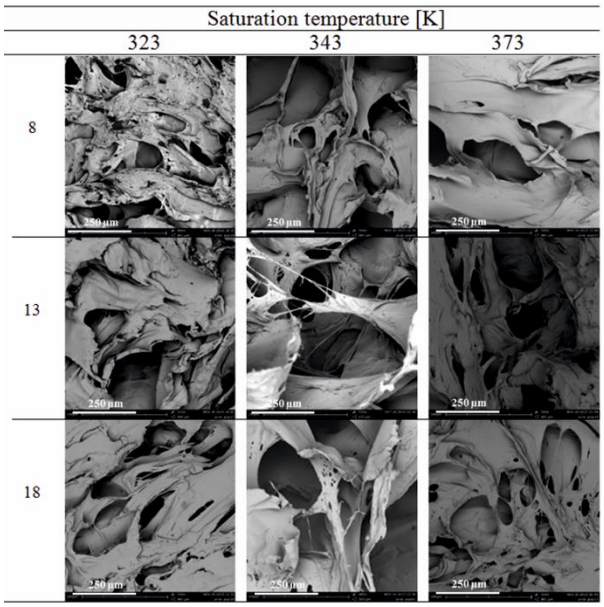

Fig. 1b. Effect of saturation temperature on morphology of porous structures

On the basis of SEM microphotographs, the pore sizes and pore size distribution of solid foams were defined, with the use of image analysing software. The performed analysis showed that the foaming method applied in this procedure resulted in generating a porous structure with partially closed pores. The effect of pressure and $scCO_2$ polymer saturation time on the pore size distribution of porous structures acquired by polymer foaming is shown in Fig. 2. Frequency distribution indicates the index in percentage of the number of pores occurring in respective pore size intervals after the range of target pore sizes is divided into separate intervals.

For a relatively short saturation time of 1 hour the increase of pressure results in obtaining a more uniform porous structure which forms small pores of size of 10 μm order, whereas for a long saturation time the opposite effect is observed. An increase in pressure of $scCO_2$ polymer saturation performed for

6 hours leads to creation of larger pores and significant homogeneity reduction of obtained porous structure. The effects of pressure and temperature of scCO$_2$ polymer saturation on the pore size distribution is shown in Fig. 3.

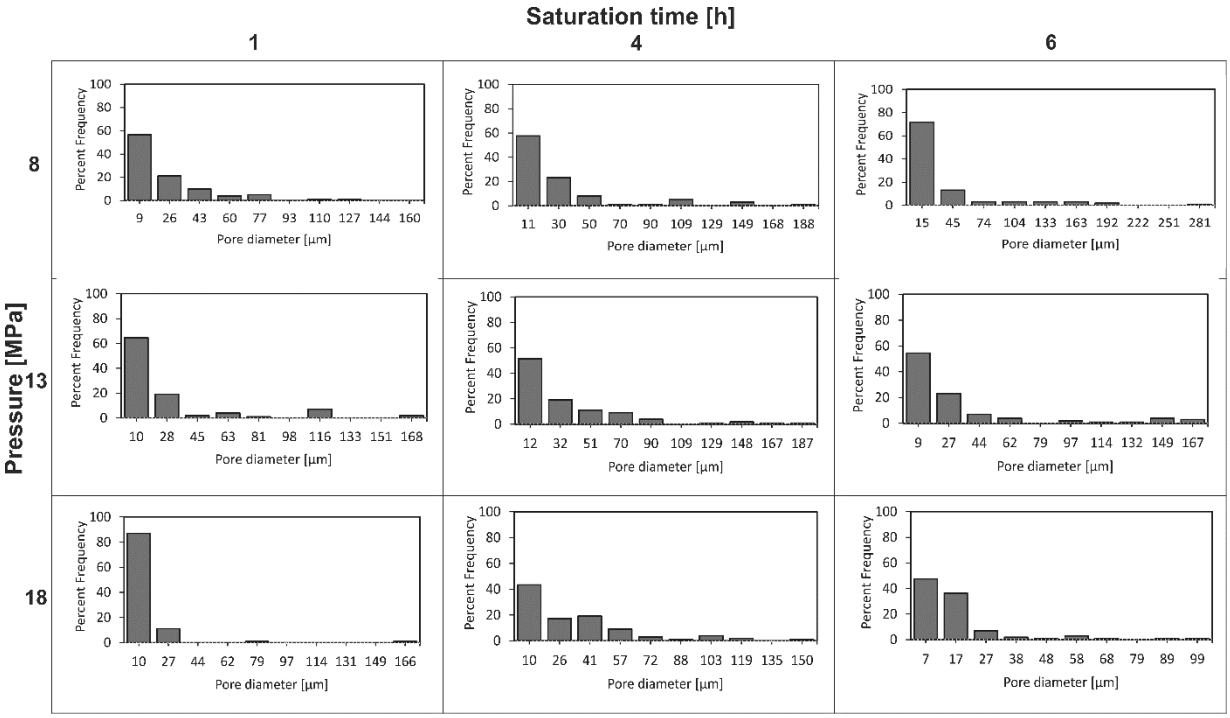

Fig. 2. The effect of pressure and time of saturation on pore size distribution of porous polymer in saturation temperature of 343 K

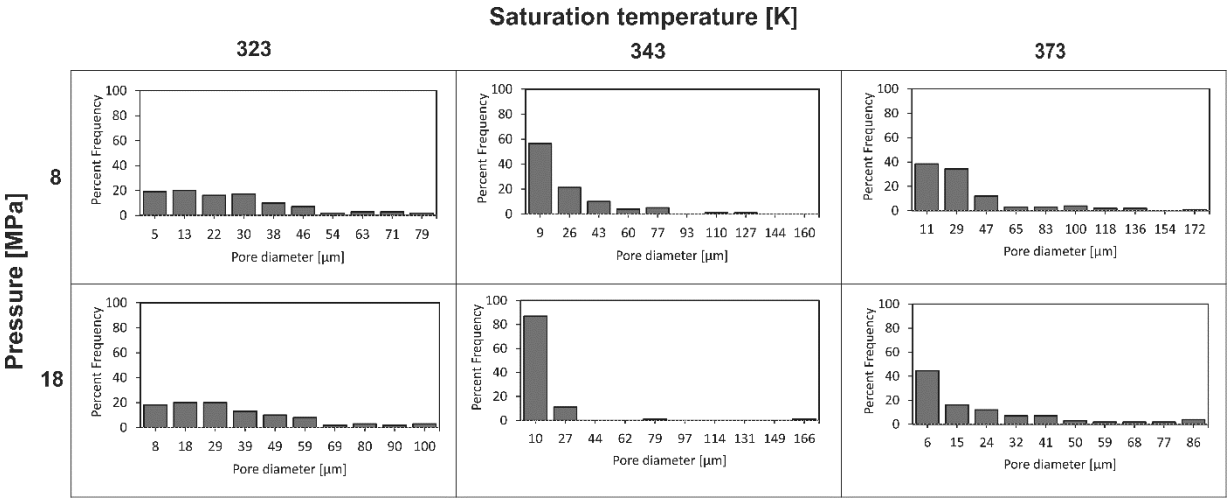

Fig. 3. The effect of pressure and temperature of saturation on pore size distribution of porous polymer for saturation time of 1 hour

In general, execution of the foaming process with the application of high pressure and short saturation time and with moderate pressure and long saturation time promotes the formation of uniform microstructure in polymer material, being the result of the melting qualities of polymer under moderate and high pressure. On the other hand, performing saturation of polymer at the temperature of 343 K leads to production of highly non-uniform porous structures. Increasing solubility of CO_2 in polymer matrix leads to the decrease of melting temperature, whereas the hydrostatic pressure causes this temperature to increase. Reportedly, CO_2 rapidly dissolves into polymers at moderate pressures, and the solubility of CO_2 increases linearly with rising pressure. The solubility effect is dominant in the

moderate pressure range, while the hydrostatic pressure effect becomes significant under higher pressures when the polymer becomes saturated and the solubility of CO_2 reaches a constant value (Takahashi et al., 2012).

The microstructure of a porous scaffold should be defined in accordance with the kind of tissue or organ being regenerated. The values of an average pore size and surface pore density characterizing the porous polymer obtained under different conditions and identified with the use of the AxioVision software are presented in Table 1. The application of supercritical fluids in the foaming process allowed to obtain polymer structures with the average pore size in the range from 15 to 45 μm and density oscillating between 2×10^4 and 12×10^4 pores/cm^2 of various uniformity.

Table 1. The effect of foaming conditions on average pore size and surface pore density of porous polymer

Pressure [MPa]		Average pores size [μm]			Average surface density of pores [10^4 pores/cm^2]		
		8	13	18	8	13	18
t sat [h]	1	25.38 (± 2.83)	26.97 (± 3.62)	11.75(± 1.99)	3.62 (± 1.21)	3.49 (± 0.69)	10.42 (± 2.40)
	4	31.33 (± 3.77)	37.84 (± 3.72)	35.70 (± 3.06)	4.04 (± 1.41)	2.83 (± 0.51)	2.19 (± 0.71)
	6	35.16 (± 5.22)	33.13 (± 4.29)	18.83 (± 1.74)	4.61 (± 1.24)	5.63 (± 1.89)	8.31 (± 2.55)
T sat [K]	323	27.28 (± 1.86)	29.38 (± 1.97)	36.91 (± 2.43)	5.41 (± 1.03)	4.21 (± 0.94)	2.95 (± 0.36)
	343	25.38 (± 2.83)	26.97 (±3.62)	11.75 (±1.99)	3.62 (±1.21)	3.49 (±0.69)	10.42 (±2.40)
	373	36.73 (± 3.34)	46.52 (± 3.07)	23.30 (± 2.16)	1.75 (± 0.18)	2.35 (± 0.41)	5.07 (± 0.67)

Table 2. Compression test results of the polymer foams

T_{sat} [K]	P_{sat}/P_{foam} [MPa]	T_{sat} [h]	Young's modulus [MPa]	Compressive strength [MPa]	Maximum strain [%]
323	8	1	20.20 (±6.62)	5.001 (±0.95)	70.022 (±0.003)
	13		4.307 (±0.38)	1.460 (±0.21)	70.007 (±0.01)
	18		19.480(±7.71)	4.686 (±1.51)	70.011 (±0.01)
343	8		2.671 (±0.72)	0.776 (±0.13)	70.014 (±0.005)
	13		1.794 (±0.47)	0.380 (±0.15)	57.742 (±12.33)
	18		1.626 (±0.54)	0.499 (±0.17)	70.007 (±0.01)
	8	4	1.908 (±0.54)	0.367 (±0.09)	61.317 (±8.67)
	13		1.302 (±0.41)	0.374 (±0.11)	58.925 (±8.07)
	18		1.763 (±0.66)	0.597 (±0.20)	57.890 (±12.12)
	8	6	1.033 (±0.62)	0.330 (±0.08)	69.997 (±0.01)
	13		7.337 (±1.82)	1.517 (±0.47)	65.184 (±4.84)
	18		2.974 (±0.31)	0.856 (±0.09)	70.019 (±0.01)
373	8	1	3.931 (±0.86)	1.032 (±0.12)	68.168 (±1.84)
	13		5.241 (±1.48)	1.346 (±0.38)	70.003 (±0.01)
	18		1.403 (±0.30)	0.309 (±0.08)	48.565 (±15.77)

The microstructure of scaffolds was defined with non- destructive x-ray microtomography. The performed μ-CT studies resulted in identification of the key properties of the obtained porous polymer, such as the interconnectivity of the pores, the porosity and foam microstructure. It was

observed that pores inside of foams were interconnected with irregular shape and porosity of structure ranging from 57 to 84 % which is optimal for bone growth (Chen Chuan-Xin et al., 2016; White et al., 2012). Moreover, the mechanical properties of scaffolds were analyzed with the static compression tests. The results of the compressive mechanical test of polymer foams obtained under different foaming conditions are summarized in Table 2.

The values of Young's modulus and compressive strength of these scaffolds depend on density and porosity of foams. The obtained porous structures were compressed to total strain of 70 % using a compression speed of 0.4 $mm \cdot min^{-1}$. Significant differences in measured mechanical parameters of the porous structures obtained at different foaming conditions could be observed. This phenomenon makes it possible to prepare scaffolds with properties correlated with specific biomedical applications. In particular, both Young's modulus and compressive strength decreased with increasing porosity and pore size. Moreover, the most rigid structure was obtained in the lowest temperature of polymer saturation. The values of these parameters in the lower range seem to be analogous to natural bone. The compression test results ensure that obtained porous structures are suitable for potential applications in bone tissue engineering (Mathieu et al., 2016).

4. CONCLUSIONS

The study findings demonstrate that $scCO_2$ application with moderate pressures and temperatures during the foaming process results in attainment of poly(ε-caprolactone) scaffolds of three-dimensional homogeneous morphologies with porosities in the order of almost 85% and pore sizes ranging from 10 to 45 μm. The influence of process parameters of supercritical carbon dioxide polymer saturation on the final attributes of obtained polymer porous structures has been identified. The most uniform porous structures with the smallest pores of average size of 11.75 μm were obtained in the foaming process carried out with polymer saturation performed at the temperature of 343 K and under the pressure of 18 MPa for the period of 1 hour. The applied method allows production of solid foams with well-controllable internal microstructure and mechanical properties favorable for cell proliferation and differentiation, and consequently tissue regeneration.

The authors gratefully acknowledge Maciej Dębowski and Andrzej Plichta (Warsaw University of Technology, Faculty of Chemistry) for their help and assistance during realization of the analytical investigation.

REFERENCES

Chen Chuan-Xin, Liu Qian–Qian, Xin Xin, Guan Yi-Xin, Yao Shan-Jing, 2016. Pore formation of poly(ε-caprolactone) scaffolds with melting point reduction in supercritical CO_2 foaming. *J. Supercrit. Fluids*, 117, 279-288. DOI: 10.1016/j.supflu.2016.07.006.

Curia S., De Focatiis D.S.A., Howdle S.M., 2015. High-pressure rheological analysis of CO_2-induced melting point depression and viscosity reduction of poly (ε-caprolactone). *Polymer*, 69, 17–24. DOI: 10.1016/j.polymer.2015.05.026.

Gloria A., Causa F., Russo T., Battista E., Della Moglie R., Zeppetelli S., De Santis R., Netti P.A., Ambrosio L., 2012. Three-dimensional poly (ε-caprolactone) bioactive scaffolds with controlled structural and surface properties. *Biomacromolecules*, 13, 11, 3510–3521. DOI: 10.1021/bm300818y.

Gualandi C., White L.J., Chen L., Gross R.A., Shakesheff K.M., Howdle S.M., Scandola M., 2010. Scaffold for tissue engineering fabricated by non-isothermal supercritical carbon dioxide foaming of a highly crystalline polyester. *Acta Biomater.*, 6, 1, 130–136. DOI: 10.1016/j.actbio.2009.07.020.

Guan J., Fujimoto K. L., Sacks M. S., Wagner W. R., 2005. Preparation and characterization of highly porous, biodegradable polyurethane scaffolds for soft tissue applications. *Biomaterials*, 26, 3961-397. DOI: 10.1016/j.biomaterials.2004.10.018.

Jacobs L.J.M., Danen K.C.H., Kemmere M.F., Keurentjes J.T.F., 2007. A parametric study of polystyrene-co-methylmethacrylate foams using supercritical carbon dioxide as a blowing agent. *Polymer*, 48, 3771-3780. DOI: 10.1016/j.polymer.2007.05.002.

Karimi M., Heuchel M., Weigel T., Schossig M., Hofmann D., Lendlein A., 2012. Formation and size distribution of pores in poly(ε-caprolactone) foams prepared by pressure quenching using supercritical CO_2. *J. Supercrit. Fluids*, 61, 175-190. DOI: 10.1016/j.supflu.2011.09.022.

Kweon H.Y., Yoo M.K., Park I.K., Kim T.H., Lee H.C., Lee H.-S., Oh J.-S., Akaike T., Cho C.-S., 2003. A novel degradable polycaprolactone networks for tissue engineering. *Biomaterials*, 24, 5, 801–808. DOI: 10.1016/S0142-9612(02)00370-8.

Liao X., Zhang H., He T., 2012. Preparation of porous biodegradable polymer and its nanocomposites by supercritical CO_2 foaming for tissue engineering. *J. Nanomaterials*, 2012, Article ID 836394. DOI: 10.1155/2012/836394.

Markočič E., Škerget M., Knez Ž., 2013. Effect of temperature and pressure on the behavior of poly (ε-caprolactone) in the presence of supercritical carbon dioxide. *Ind. Eng. Chem. Res*., 52, 15594-15601. DOI: 10.1021/ie402256a.

Mathieu L.M., Mueller T.L., Bourban P.E., Pioletti D.P., Muller R., Manson J.A.E., 2006. Architecture and properties of anisotropic polymer composite scaffold for bone tissue engineering. *Biomaterials*, 27, 905-916. DOI: 10.1016/j.biomaterials.2005.07.015.

Nalawade S.P., Picchioni F., Janssen L.P.B.M., 2006. Supercritical carbon dioxide as a green solvent for processing polymer melts: Processing aspects and applications. *Prog. Polym. Sci.*, 31, 19-43. DOI: 10.1016/j.progpolymsci.2005.08.002.

Reverchon E., Cardea S., Rapuano C., 2008. A new supercritical fluid-based process to produce scaffolds of tissue replacement. *J. Supercrit. Fluids*, 45, 365-373. DOI: 10.1016/j.supflu.2008.01.005.

Takahashi S., Hessler J.C., Kiran E., 2012. Melting behaviour of biodegradable polyesters in carbon dioxide at high pressures. *J. Supercrit. Fluids*, 72, 278-287. DOI: 10.1016/j.supflu.2012.09.009.

Tarabasz K., Henczka M., 2016. Experimental investigations into foaming of biodegradable polymers using $scCO_2$. *Inż. Ap. Chem*., 55, 40-41.

Tarabasz, K., Krzysztoforski, J., Szwast, M., Henczka, M., 2016. Investigation of the effect of treatment with supercritical carbon dioxide on structure and properties of polypropylene microfiltration membranes. *Matt. Letters*, 163, 54-57. DOI: 10.1016/j.matlet.2015.10.010.

Tayton E., Purcell M., Arvold A., Smith J.O., Kalra S., Briscoe A., Shakesheff K., Howdle S.M., Dunlop D.G., Oreffo R.O.C., 2012. Supercritical CO_2 fluid-foaming of polymers to increase porosity: a method to improve the mechanical and biocompatibility characteristics for use as a potential alternative to allografts in impaction bone grafting? *Acta Biomater*., 8, 1918-1927. DOI: 10.1016/j.actbio.2012.01.024.

Tsivintzelis I., Angelopoulou A.G., Panayiotou C., 2007. Foaming of polymers with supercritical CO_2: An experimental and theoretical study. *Polymer*, 48, 5928-5929. DOI: 10.1016/j.polymer.2007.08.004.

Tsivintzelis I., Pavlidou E., Panayiotou C., 2006. Biodegradable polymer foams prepared with supercritical CO_2-ethanol mixtures as blowing agent. *J. Supercrit. Fluids*, 42, 265-272. DOI: 10.1016/j.supflu.2007.02.009.

White L.J., Hutter V., Tai H., Howdle S.M., Shakesheff K.M., 2012. The effect of processing variables on morphological and mechanical properties of supercritical CO_2 foamed scaffolds for tissue engineering. *Acta Biomater*., 8, 61-71. DOI: 10.1016/j.actbio.2011.07.032.

Received 10 April 2017
Received in revised form 07 November 2017
Accepted 08 November 2017

www.czasopisma.pan.pl www.journals.pan.pl
Chemical and Process Engineering 2017, 38 (4), 543-554
DOI: 10.1515/cpe-2017-0043

DETERMINATION OF DIFFUSION COEFFICIENT AND PERMEABILITY THROUGH THE BARRIER OF SUBSTANCE IN SIMULATED BIOMEDICAL SYSTEMS

Anna Adach*[1], Natalia Kister[2], Andrzej Skassa[1], Aleksandra Bugalska[1]

[1]Warsaw University of Technology, Faculty of Chemical and Process Engineering, Waryńskiego 1, 00-645 Warsaw, Poland

[2]Warsaw University of Technology, Faculty of Chemistry, Noakowskiego 3, 00-645 Warsaw, Poland

The investigations deal with mass transfer in simulated biomedical systems. The modification of classical diffusion chamber, sequential unit (SU) system, imitated different biomedical setups, boundary conditions. The experiments simulated: diffusion chamber (also with two barriers), transport through the membrane to the blood stream, transport from the stent eluting drug simultaneously to the vessel cells and to the blood stream. The concentrations of substances and the relative mass increases/decreases for SU systems indicate that the order of the curves follows the order of mass transfer resistances. The strong dependence of mass transfer rates versus type of diffusing substance was confirmed. The calculated drug fluxes, diffusion coefficients, permeation coefficients are convergent with literature. Permeation coefficients for complex sequential systems can be estimated as parallel connexion of constituent coefficients. Experiments approved functionality of the SU for investigations in a simulated biomedical system. Obtained data were used for numerical verification.

Keywords: drug release, substance transfer, diffusion chamber, biomedical systems

1. INTRODUCTION

Substance transport in biomedical systems applies to many processes in living organisms e.g. drug transport in tissues, the diffusion through biological membranes. In an ideal system, the drug would migrate to the proper organ quickly and in the optimal concentration (within therapeutic window), acting actively by the determined period of time, without any negative side effects and finally would be removed from organism. However, real processes undergoing in biomedical systems are very complex and it is difficult to obtain such a perfect scheme. Therefore experimental tests and studies on mathematical model simulations are carried out simultaneously for determining the drug transfer in such systems, which would help in predicting and controlling drug release.

The basic mechanism of mass transport in biomedical systems is diffusion in porous bodies or liquids, and transport by selective membranes. Previously designed systems were applied in Franz cells (Franz, 1975) and Ussing chambers (Ussing, 1947). Nowadays there are several methods of determining drug transfer in biomedical systems (Siepmann and Siepmann, 2008; Siepmann and Siepmann, 2012). The classical diffusion chamber is built of two chambers (donor and acceptor ones) separated by a membrane or another mass transfer barrier. The ideal mixing in both chambers allows to determine the diffusion coefficient by the membrane or/and the mass transfer rate (Bartosova and Bajgar, 2012; Cu

*Corresponding authors, e-mail: anna.adach@pw.edu.pl

and Saltzman, 2009; Desai and Vadgama, 1991). The submerged chamber acts analogically, however the donor chamber is immersed in a bigger acceptor chamber, through which the pure dissolvent flows (Addicks et al., 1987). Another modification is the dialysis sac method (or reversed dialysis) in which the dissolved drug fulfils the internal of the sac, while the concentration of the substance is measured in the circulating fluid (Lovich et al., 1998). Diffusion through the medium can also be determined by the so-called "infinite layer" method. The layer of active substance or its concentrated solution is contacted with the "mass transfer barrier", e.g. hydrogel of much bigger dimension. After a certain period of time the concentration of drug can be evaluated in the thin sliced layers of "barrier". Due to the conditions, the process is considered as unsteady, one-dimensional transport (Cu and Saltzman, 2009). Non-invasive methods allow determining of diffusion rate without intervention in the experimental system (e.g. without the destruction of sample or probing). The methods consist of the radioactive or fluorescent particle cracking. The feedback from experiments is very convenient but modification of active substances molecules is necessary (Cu and Saltzman, 2009; Groo and Lagarce, 2014). Substances like proteins or DNA can be traced using holographic interferometry and the phenomenon of light dispersion, diffusion of substances in gels can be determined by NMR spectroscopy. Spectroscopy FC or FRAP are used for visualization of transport of fluorescently tagged viruses, proteins, peptides or polymer nanoparticles in different media (Cu and Saltzman, 2009; Groo and Lagarce, 2014).

The aim of research was to investigate active substance migration in simulated biomedical systems with the use of a self-designed experimental Sequential Unit system. The arrangements were to imitate mass transfer in different natural conformations. The parameters characterizing mass transfer in examined systems were to be obtained: diffusion coefficients, rates of diffusion, permeation coefficients.

2. EXPERIMENTS WITH SEQUENTIAL UNIT

The structure of the Sequential Unit (SU) is a self-designed modification of the classical diffusion chamber described above. The unique attribute of SU is the possibility of optional mounting of several modules made of acrylic glass, of different dimensions (cylindrical shape), which can be jointed in "parallel" sets. The unit, depending on the conducted experiment consisted of a donor chamber (with the examined medium), an acceptor chamber, a flow chamber etc. The units are bounded by medium or membrane constituting a mass transfer "barrier". Therefore many various geometrical combinations can be constructed, which could simulate different biomedical systems. This enables to determine mass transfer of the active substance under diverse initial and boundary conditions and process parameters (e.g. viscosity).

2.1. Sequential Unit system SU1

In the simplest setup, similar to Diffusion Chamber, the dissolved drug is transported from the donor chamber through the membrane (or other mass transfer barrier) to the acceptor chamber. The solutions in both chambers are mixed. The mass transfer barrier is mechanically supported and divided from the solutions by membranes characterized by great permeability and small mass transfer resistances. The concentration of substance in both units can be measured in proper periods of time. Diffusion coefficient can be determined using Diffusion Chamber in two ways. The known drug concentrations in the acceptor and donor chamber enable to calculate the substance flux and therefore the diffusion coefficient. The value of this coefficient can also be obtained according to lag time, i.e. when drug appears in the acceptor chamber (Cu and Saltzman, 2009). This setup corresponds to a biomedical system in which the active ingredient is contacted directly with the organ to which it is transported.

This arrangement allows to determine diffusion coefficients as well as permeation coefficients through the media constituting mass transfer barriers. Thanks to the fragmented construction of SU, the migration of the active substance in simulated complex systems e.g. through two (or more) media being mass transfer barriers can also be studied.

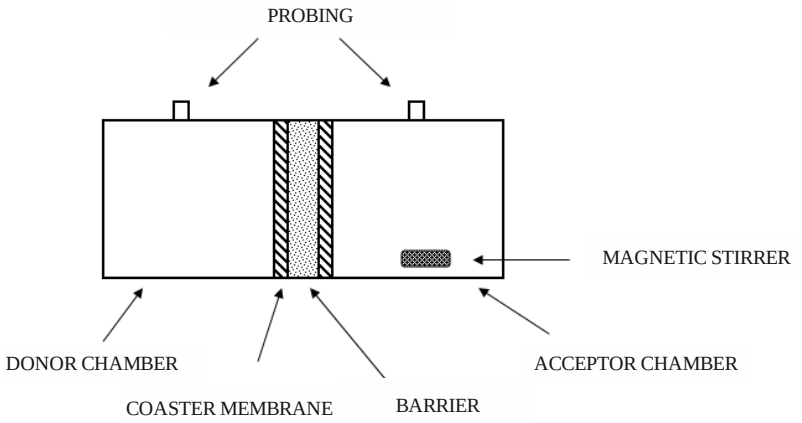

Fig. 1. SU1: Sequential Unit system, set up as Diffusion Chamber; diffusion through mass barrier e.g. membrane, hydrogel etc.

2.2. Sequential Unit system SU2

The next geometrical SU configuration consists of a donor chamber (with a solution of substance), mass transfer barrier and flow unit which the pure solvent flows through. The volumetric flow of liquid can be regulated. In the conducted experiments it was adjusted at the levels of blood flow in blood vessels.

Such conformations deal with the system, where the drug is transported from a dosing unit (donor chamber) through the biological membrane to the blood (flow unit = acceptor chamber).

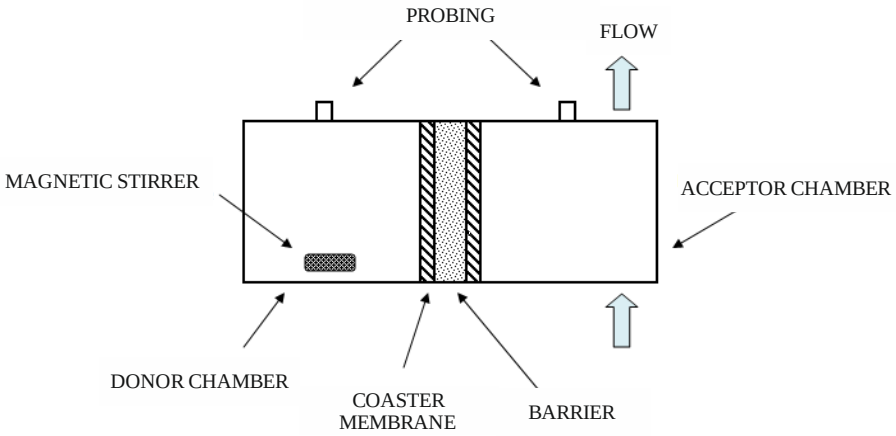

Fig. 2. SU2: Sequential Unit system with the flow chamber

2.3. Sequential Unit system SU3

The next system includes: a donor unit, a mass transfer barrier and a flow unit with recirculation. This system simulates the situation, when the substance transported to blood is accumulated in this liquid and is circulating internally in blood vessels (external reservoir).

The above arrangement can respond also to the process of supplementation of drug circulating in blood vessels (solution of drug in external reservoir) to body organs.

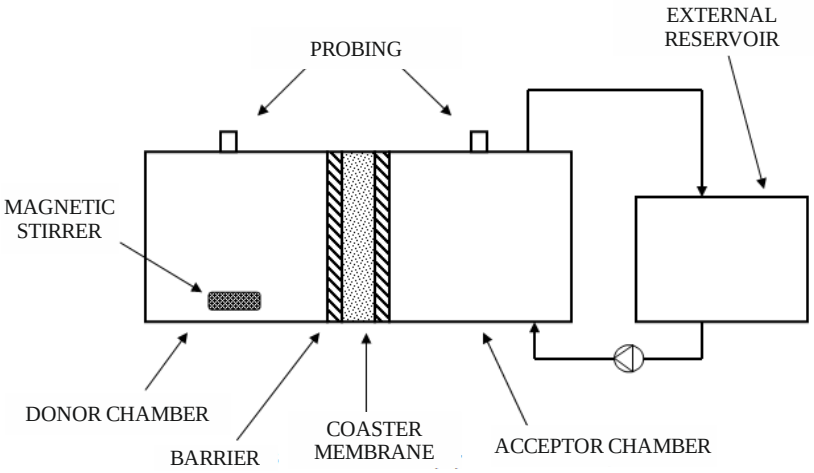

Fig. 3. SU3: Sequential Unit system with the flow chamber and recirculation

2.4. Sequential Unit system SU4

The system of SU presented below contains a donor chamber (with the solution of drug) located between the acceptor and flow units (with or without recirculation). The consecutive ventricles are separated by the following mass transfer barriers.

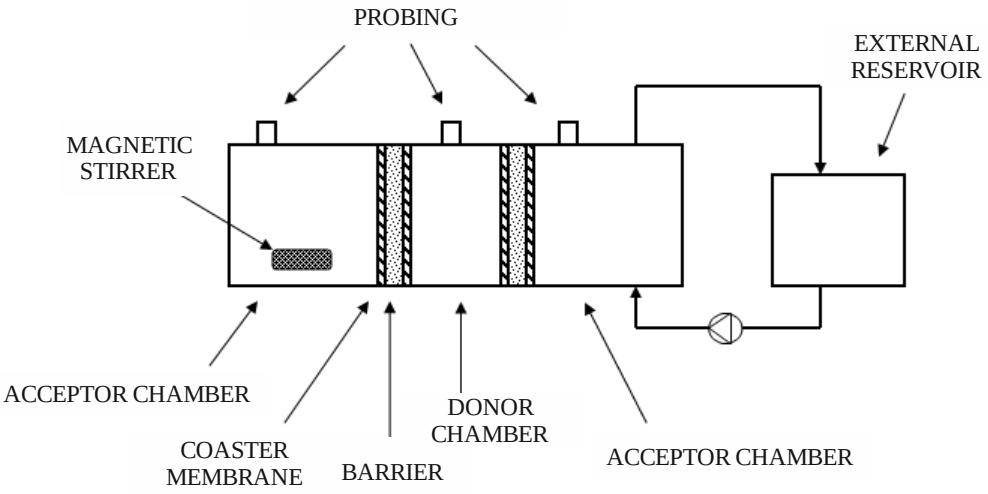

Fig. 4. SU4: Sequential Unit system imitating drug-eluting stent placed within the blood vessel

Stents implemented into blood vessels constitute a kind of scaffold for the sunken vessel. However, the use of stent frequently results in hyperplasia as a side effect (excessive increase of the amount of vessel cells), resulting in the thickening of arterial walls and decreased arterial lumen space.

The described geometry corresponds to the stent (with drug immobilized on it), inserted inside the blood vessel. While such situation occurs, the active substance deposited on the stent is simultaneously transported to the pellicle of the blood vessel (acceptor chamber) and swept away by the flowing blood (flow unit with circulation). Therefore the drug-eluting stents show promise with marked reduction in intimal hyperplasia compared to bare, metal stents. The above theme was the subject of investigations (Hirata et al., 2013; Kleinedler, 2012; Ziętek et al., 2013).

3. EXPERIMENTS

Experiments were carried out in sequential systems described above. These different geometric configurations of SU, in a simplified way, simulated processes of drug transport in various biomedical systems (Bugalska, 2015; Kister, 2015; Skassa, 2015).

The experiments differed from each other in several parameters. Substances used to simulate the active ingredient of drugs were: Cochineal Red A (Ponceau 4 R, Acid Red 18), Dopamine hydrochloride and Rhodamine B (Sigma Aldrich). Various concentrations of these substances were employed: from 0.01% mass. to 1% mass. Several media were examined as mass barrier in respective cases: gelatine as the simplest example of hydrogel, synthetic saliva and solutions of Sodium Carboxymethyl Cellulose (CMCNa).

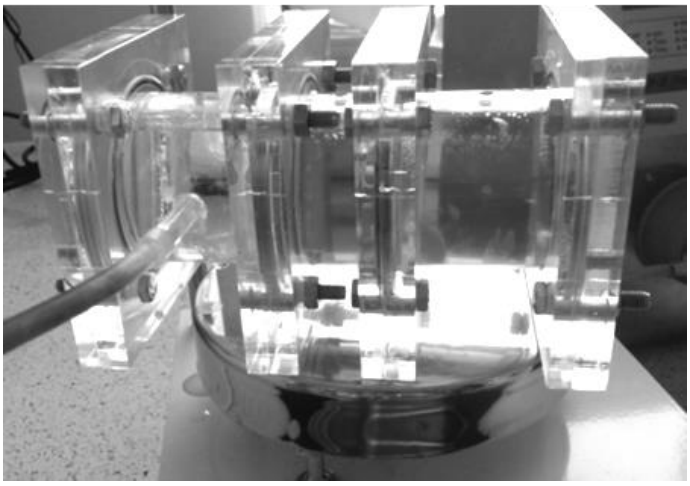

Fig. 5. The photograph of SU4 system

As „base", mechanical coasters of hydrophilic PES membranes (Polyethersulphone Membranes) were used due to big permeability and small mass transport resistance (Pall Corporation).

Different volumetric flows of liquid in a flow unit were applied. Always, however, being within the scope of velocity of blood flow in blood vessels, volumetric flow range: Q = 83.5 cm^3/min – 300 cm^3/min. The influence of liquid viscosity on mass transfer was also studied using different CMC solutions.

Samples were analysed by spectrophotometry (Hitachi U-2900), studies were conducted in the range of a linear function of absorbance limited by ABS < 2.5, thus fulfilling the Lambert-Beer law. The calibration curves were used for examined active substances allowing to calculate percentage and molar concentration as a function of absorbance (Bugalska, 2015; Kister, 2015; Pawlak, 2013).

4. ANALYSIS OF THE RESULTS

The initial (total) mass of substance (donor chamber) was calculated as below:

$$m_0 = V_D \cdot c_0 \cdot \frac{\rho_r}{100\%} \tag{1}$$

In acceptor chambers without the flow, mass of substance which migrated to this unit was calculated from the following equation:

$$m_{acc} = \frac{V_A \cdot \rho_r \cdot c_A}{100\%} \tag{2}$$

Mass of substance in the donor chamber in the given moment was computed from the measured values of absorbance (and therefore concentration) or as a difference between the total mass of substance and the mass which migrated to acceptor/flow chamber:

$$m_{don} = \frac{V_D \cdot \rho_r \cdot c_A}{100\%} \tag{3}$$

$$m_{don} = m_0 - m_{acc} \quad \text{or} \quad m_{don} = m_0 - m_{flow} \quad \text{or} \quad m_{don} = m_0 - m_{acc} - m_{flow} \tag{4}$$

Relative mass of drug respectively in acceptor/donor chambers was also evaluated:

$$\Delta m_A = \frac{m_{acc}}{m_0} \cdot 100\% \tag{5}$$

$$\Delta m_D = \frac{m_{don}}{m_0} \cdot 100\% \tag{6}$$

The mass of substance flowing out of SU system was calculated based on the current concentration of the drug in the flowing flux:

$$m_{flow} = \frac{\int_0^t c_{flow}(t) \cdot \rho_r \, Q \, dt}{100\%} \tag{7}$$

The total mass of substance in the SU systems with the external reservoir must fulfil the equation (for SU3 system):

$$m_{don} + m_{reserv} = m_0 - m_{acc} \tag{8}$$

or the formulation below for SU4 system:

$$m_{don} + m_{reserv} = m_0 - (m_{acc1} + m_{acc2}) \tag{9}$$

The results of the investigations are presented in the form of graphs illustrating relative mass gain/loss of an active ingredient in the acceptor/donor compartment for exemplary systems. Strong dependence of mass transfer rates versus type of diffusing substance was shown in Fig. 6.

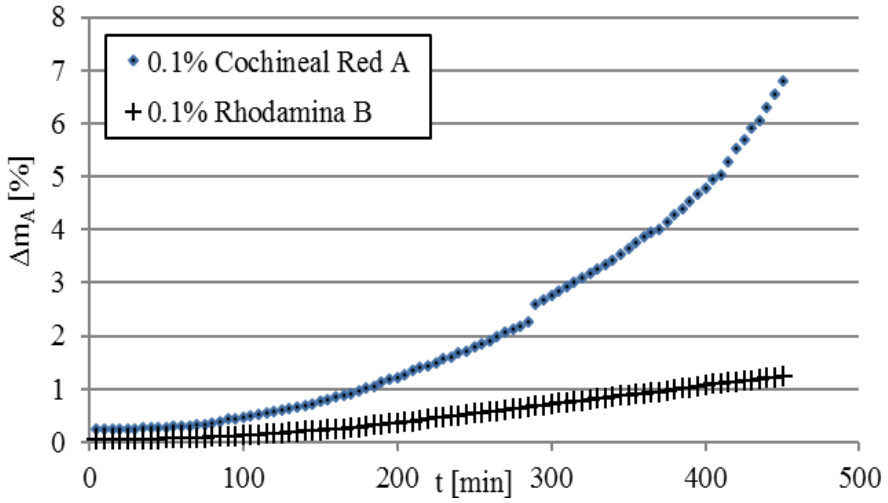

Fig. 6. The relative mass increase of substance in SU4 system (imitating stent) in acceptor chamber; diffusion through gelatin as mass transfer barrier

With an increase of the initial concentration of the active ingredients the mass transfer rate increased, due to the greater driving force of the process. The strong dependence of mass transfer rates versus concentration of diffusing substance was confirmed in the previous investigations (Bugalska, 2015; Kister, 2015; Skassa, 2015).

One of the main factors that determines the rate of substance transport is the type of the barrier medium (Fig. 7). The rate of diffusion through the PES membrane was a few times greater than that of hydrogel. The diffusion rate significantly decreased when a solution of higher viscosity was used as a solvent (viscosity of 1% solution of CMC was μ = 25 [mPa·s] while the viscosity of 2% solution of CMC was about μ = 300 [mPa·s]).

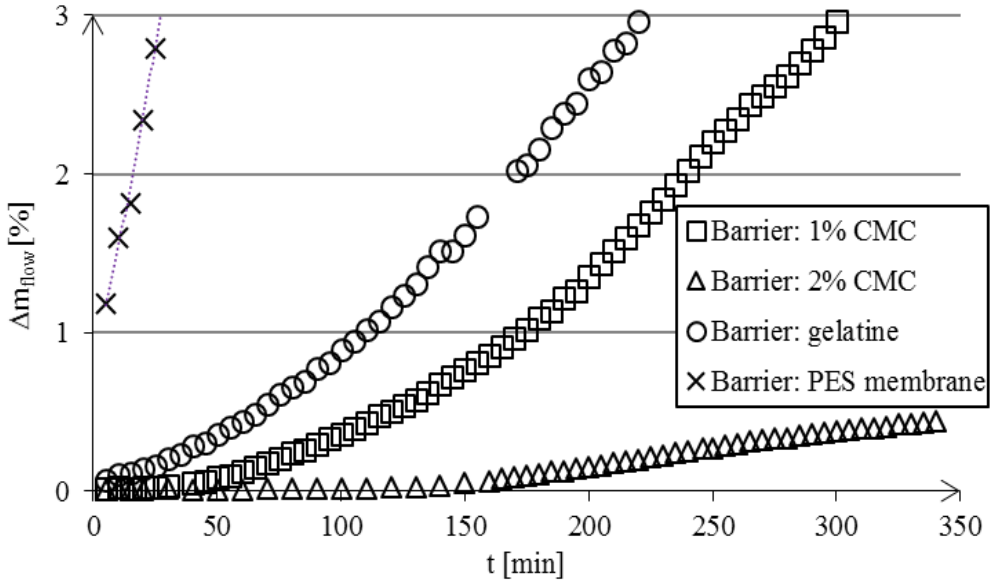

Fig. 7. The relative mass increase of substance in SU2 system (with flow) in acceptor chamber; diffusion through different mass transfer barriers, solution of Cochineal Red A (1%)

The impact of the volume flow on propulsive force and speed of the process is noticeable in Fig. 8. With increasing volumetric flow the mass transfer rate was growing.

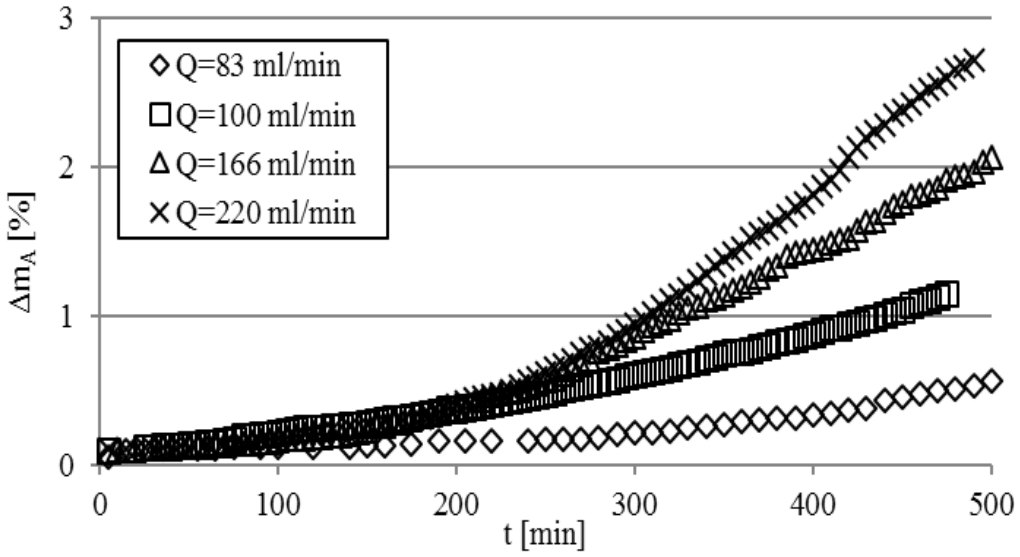

Fig. 8. The relative mass increase of substance in acceptor chamber in SU3 system (flow with recirculation); diffusion of Cochineal Red A (0,03%) through gelatin as mass transfer barrier

The relative amounts of active substance used during experiments conducted in SU4 system (imitating stent) is illustrated in Fig. 9.

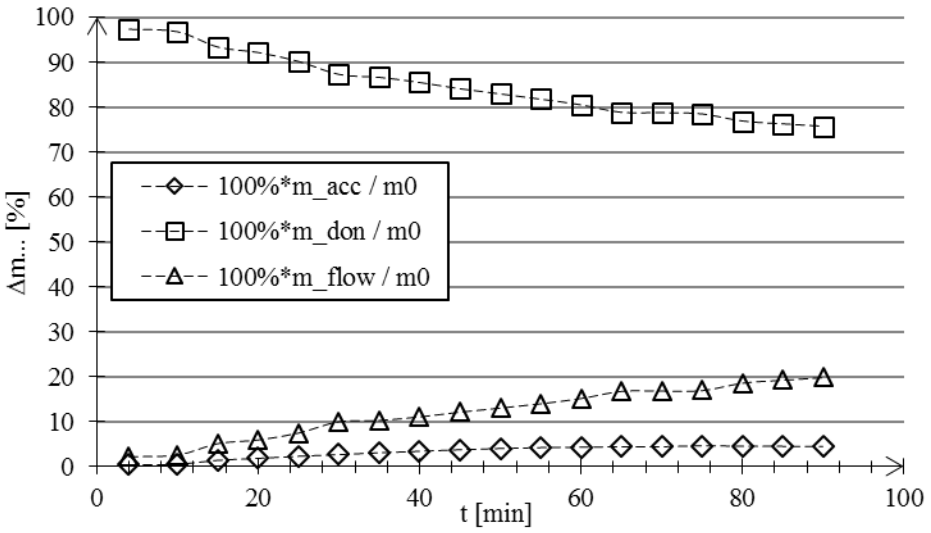

Fig. 9. The relative mass amounts of substance in chambers in adequate SU4 system (flow with recirculation); diffusion of Cochineal Red A (1%) through gelatin as mass transfer barrier

The flux of an active substance A (per unit area) could be calculated from the equations:

$$J_A = \frac{\partial n}{\partial t \cdot A} \tag{10}$$

$$J_A = -D\frac{\partial c_A}{\partial x} \tag{11}$$

The effective diffusion coefficients can be obtained as:

$$D = -\frac{J_A}{\frac{\partial c_A}{\partial x}} \tag{12}$$

The permeability coefficients κ were evaluated:

$$\kappa = \frac{J_A}{c_{AD}} \tag{13}$$

The exemplary values of the calculated coefficients are listed below in Table 1.

Table 1. Exemplary values of diffusion and permeability coefficients for different mass barrier media

Substance	Subst. molecular mass [g/mol]	Type of mass barrier	Diffusion coeff. D [m^2/s]	Permeability coeff. κ [m/s]
Dopamine hydrochloride	189.64	Gelatin	3.46×10^{-11}	0.42
Rhodamine B	479.01	Gelatin	4.10×10^{-12}	0.29
Cochineal Red A	604.47	Gelatin	7.62×10^{-11}	0.49
Cochineal Red A	604.47	Synthetic saliva	7.19×10^{-10}	1.81
Cochineal Red A	604.47	CMC 0,5%	6.85×10^{-10}	1.63
Cochineal Red A	604.47	CMC 1%	6.25×10^{-10}	1.29
Cochineal Red A	604.47	CMC 2%	2.51×10^{-10}	0.61
Cochineal Red A	604.47	CMC 3%	4.05×10^{-11}	0.097
Cochineal Red A	604.47	CMC 4%	2.00×10^{-11}	0.051

The obtained results were consistent with the literature data (Giannola et al., 2007; Ansari et al., 2006; Serra et al., 2006).

The calculations indicated that the permeation coefficients for complex sequential systems (e.g. two media being the mass transfer barriers) can be estimated as a sum of two constituent permeation coefficients connected in parallel:

$$\frac{1}{\kappa_{1+2}} = \frac{1}{\kappa_1} + \frac{1}{\kappa_2} \tag{14}$$

For example, the effective permeation coefficient for the complex SU1 system gelatine/synthetic saliva calculated from Eq. (14) resulted in $\kappa_{gelat/saliva} = 0.3859$ m/s while the experimental permeation coefficient for the system where both gelatine and synthetic saliva constituted mass transfer barrier was $\kappa_{gelat/saliva} = 0.3488$ m/s. Franke et al. (2000) also assumed that the total resistance of the system is additively composed of two parallel resistances: that of the cell monolayer and that of the filter. It should be underlined that Eq. (14) is valid when both mass transfer resistances are linear versus concentration.

The exemplary fluxes (per unit area) of an active substance given below were calculated at the steady state.

Table 2. Exemplary values of fluxes (per unit area) of active substance for different mass barrier media (molecular mass of Cochineal Red A is 604.47 [g/mol]).

Substance	Type of mass barrier	J_A [mol/m2s]
0.01% solution of Cochineal Red A	gelatine	1.10×10^{-8}
0.03% solution of Cochineal Red A	gelatine	1.83×10^{-8}
0.10% solution of Cochineal Red A	gelatine	6.20×10^{-8}
0.25% solution of Cochineal Red A	gelatine	2.85×10^{-7}
1.00% solution of Cochineal Red A	gelatine	1.24×10^{-6}
1.00% solution of Cochineal Red A	CMC 1%	7.18×10^{-7}
1.00% solution of Cochineal Red A	CMC 2%	2.12×10^{-7}
1.00% solution of Cochineal Red A	CMC 3%	1.94×10^{-8}
1.00% solution of Cochineal Red A	membrane PES	1.15×10^{-5}

The paper belongs to a wide range of studies on migration of substances in simulated biomedical systems. The results serve as an input values for numerical calculations (presented in another article).

5. CONCLUSIONS

The presented investigations concern mass transfer in simulated biomedical systems. An originally designed Sequential Unit (SU) system was set up. The unique attribute of SU is a possibility of the optional joining of different elements in sequential, "parallel" sets and therefore the migration of the active substance in simulated complex systems could be studied, imitating different biomedical conditions and various boundary conditions.

Apart from the diffusion investigations provided in a classical diffusion chamber, other unit sets, simulating different biomedical systems were analysed. The conducted experiments simulated e.g. the situation when the active substance migrates through the permeable membrane to the blood stream and

is accumulated in the liquid (or is not, in other experiments). Another system simulated the situation when the active substance from the drug eluting stent was transported to the blood vessel cells and simultaneously was drifted by the blood stream. The substance migration from the donor chamber through at least two media (e.g. selective synthetic saliva/gelatine) to the pure solvent was also investigated. Experimental studies were performed with several biomedical media and active substances.

The substance concentrations in the chambers as a function of time as well as the relative mass increase for different SU systems indicate the correctness of the results. The order of the curves follows the order of mass transfer resistances. The issues confirm a strong dependence of the mass transfer rate versus type of diffusing substance while the influence of substance concentration was discussed in earlier works (Bugalska, 2015; Kister, 2015; Skassa, 2015).

The drug fluxes and the effective diffusion coefficients in the examined media were calculated as well as the permeation coefficients for different systems. The computed values of coefficients are in agreement with literature data. The calculations indicate that the permeation coefficients for the complex sequential systems (two media being the mass transfer resistances) can be estimated as a sum of two constituent permeation coefficients connected in parallel.

The conducted experiments confirmed the functionality of the sequential system for studying the mass transfer in simulated biomedical systems. The obtained data were used for the experimental verification of the mathematical model of the process.

The bases for this work have been carried out within the financial support of the National Science Centre Grant No. N N209 132640.

SYMBOLS

A	area of mass transfer, m^2
c	concentration of the diffusing substance, $\%_{mass}$
c_0	initial concentration of the diffusing substance, $\%_{mass}$
c_A	concentration of the diffusing substance, mol/dm^3
c_{AD}	concentration of the diffusing substance in donor chamber, mol/dm^3
$c_{flow}(t)$	concentration of the diffusing substance in flow unit, $\%_{mass}$
C_{MD}	concentration of the diffusing substance, mol/dm^3
D	diffusion coefficient, m^2/s
J_A	flux of substance A per unit area, $mol/(m^2 \cdot s)$
M	molar mass of substance A, g/mol
m_0	initial (total) mass of the diffusing substance (donor chamber), g
Δm_0	relative increase of mass of the diffusing substance in acceptor chamber, $\%_{mass}$
m_{acc}	mass of the diffusing substance in acceptor chamber, g
m_{don}	mass of the diffusing substance in donor chamber, g
Δm_D	relative decrease of mass of the diffusing substance in donor chamber, $\%_{mass}$
m_{flow}	mass of the diffusing substance drifted from flow chamber, g
m_{reserv}	mass of the diffusing substance in external reservoir, g
n	number of moles of substance A, mol
Q	volumetric flow of the solution, dm^3/s
t	time, s
V_A	volume of the acceptor chamber, dm^3
V_D	volume of the donor chamber, dm^3

x coordinate parallel to the diffusion flux direction, ranging from 0 to the mass barrier thickness, m

Greek symbols

κ permeation coefficient, m/s

ρ_r density of solution, g/dm^3

REFERENCES

Addicks W.J., Flynn G.L., Weiner N., 1987. Validation of a flow-through diffusion cell for use in transdermal research. *Pharm. Res.*, 4, 337-341. DOI: 10.1023/A:1016405506028.

Ansari M., Kazemipour M., Aklamli M., 2006. The study of drug permeation through natural membranes. *Int. J. Pharm.*, 327, 6-11. DOI: 10.1016/j.ijpharm.2006.07.034.

Bartosowa L., Bajgar J., 2012. Transdermal drug delivery in vitro using diffusion cells. *Curr. Med. Chem.*, 19, 4671–4677. DOI: 10.2174/092986712803306358.

Bugalska A., 2015. *Badanie szybkości migracji składnika aktywnego w symulowanych układach biomedycznych dla różnych warunków początkowych i brzegowych*. MSc thesis, Warsaw University of Technology, Warsaw.

Cu Yen, Saltzman W. M., 2009. Mathematical modelling of molecular diffusion through mucus. *Adv. Drug Delivery Rev.*, 61, 101-114. DOI: 10.1016/j.addr.2008.09.006.

Desai M.A., Vadgama P., 1991. Estimation of effective diffusion coefficients of model solutes through gastric mucus: assessment of a diffusion chamber technique based on spectrophotometric analysis. *Analyst*, 116, 1113-1116. DOI: 10.1039/AN9911601113.

Franke H., Galla H.J., Beuckmann C.T., 2000. Primary cultures of brain microvessel endothelial cells: a valid and flexible model to study drug transport through the blood–brain barrier in vitro. *Brain Res. Protoc.*, 5, 248–256. DOI: 10.1016/S1385-299X(00)00020-9.

Franz T. J., 1975. Percutaneous absorption on the relevance of in vitro data. *J. Invest. Dermatol*. 64(3), 190–195. DOI: 10.1111/1523-1747.ep12533356.

Giannola L.I., De Caro V., Giandalia G., Siragusa M.G., Campisi G., Florena A. M., Ciach T., 2007. Diffusion of naltrexone across reconstituted human oral epithelium and histomorphological features. *Eur. J. Pharm. Biopharm.*, 65, 238-246. DOI: 10.1016/j.ejpb.2006.07.004.

Groo A.C., Lagarce F., 2014. Mucus models to evaluate nanomedicines for diffusion. *Drug Discovery Today*, 19, 1097-1108. DOI: 10.1016/j.drudis.2014.01.011.

Hirata, Y., Kurobe, H., Nishio, C., Tanaka, K., Fukuda, D., Uematsu, E., Nishimoto, S., Soeki, T., Harada, N., Sakaue, H., Kitagawa, T., Shimabukuro, M., Nakaya, Y., Sata, M., 2013. Exendin-4, a glucagon-like peptide-1 receptor agonist, attenuates neointimal hyperplasia after vascular injury. *Eur. J. Pharmacol.*, 669, 106-111. DOI: 10.1016/j.ejphar.2012.11.057.

Kister N., 2015. *Wyznaczanie szybkości dyfuzji w biomedycznych*. MSc thesis, Warsaw University of Technology, Warsaw.

Kleinedler J.J., 2012. Novel nanocomposite stent coating releasing resveratrol and quercetin reduces neointimal hyperplasia and promotes re-endothelialization. *J. Controlled Release*, 125, 27-33. DOI: 10.1016/j.jconrel.2012.01.008.

Lovich M.A., Philbrook M., Sawyer S., Weselcouch E., Edelman E.R., 1998. Arterial heparin deposition: role of diffusion, convection, and extravascular space. *American Journal of Physiology - Heart and Circulatory Physiology*, 275 (6), 2054-2087.

Pawlak A., 2013. *Badanie szybkości migracji substancji z dodatnich źródeł masy*. MSc thesis, Warsaw University of Technology, Warsaw.

Serra L., Domenech J., Peppas N.A., 2006. Drug transport mechanism and release kinetics from molecularly designed poly(acrylic acid-g-ethylene glycol) hydrogels. *Biomaterials*, 27, 5440-5451. DOI: 10.1016/j.biomaterials.2006.06.011.

Siepmann J., Siepmann F., 2008. Mathematical modelling of drug delivery (Review). *Int. J. Pharm.*, 364, 328-343. DOI: 10.1016/j.ijpharm.2008.09.004.

Siepmann J., Siepmann F., 2012. Modelling of diffusion controlled drug delivery. *J. Controlled Release*, 161, 351-362. DOI: 10.1016/j.jconrel.2011.10.006.

Skassa A., 2015. *Badanie szybkości migracji składnika aktywnego w symulowanych układach biomedycznych o różnych geometriach.* MSc thesis, Warsaw University of Technology, Warsaw.

Ussing H. H. 1947. Interpretation of the exchange of radio-sodium in isolated muscle. *Nature*, 160, 262. DOI: 10.1038/160262a0.

Ziętek P., Butruk B., Ciach T., 2013. Endothelial cells adhesion on modified polyurethane surface as the way to fabricate a novel material for cardiosurgery, In: Santos R., Aldred N., Gorb S., Flammang P. (Eds.), *Biological and biomimetic adhesives. Challenges and opportunities*. RSC Publishing Cambridge, UK, 149-163. DOI: 10.1039/9781849737135-00149.

Received 07 April 2017
Received in revised form 09 November 2017
Accepted 10 November 2017

www.czasopisma.pan.pl www.journals.pan.pl
Chemical and Process Engineering 2017, 38 (4), 555-565
DOI: 10.1515/cpe-2017-0044

INVESTIGATION OF MIXING TIME IN LIQUID UNDER INFLUENCE OF ROTATING MAGNETIC FIELD

Alicja Przybył *[1], Rafał Rakoczy[1], Maciej Konopacki[1], Marian Kordas[1], Radosław Drozd[2], Karol Fijałkowski[2]

[1]West Pomeranian University of Technology Szczecin, Faculty of Chemical Technology and Engineering, Institute of Chemical Engineering and Environmental Protection Processes, al. Piastów 42, 71-065 Szczecin, Poland

[2]West Pomeranian University of Technology Szczecin, Faculty of Biotechnology and Animal Husbandry, Department of Immunology, Microbiology and Physiological Chemistry, al. Piastów 45, 70-311 Szczecin, Poland

The aim of the study was to present an experimental investigation of the influence of the RMF on mixing time. The obtained results suggest that the homogenization time for the tested experimental set-up depending on the frequency of the RMF can be worked out by means of the relationship between the dimensionless mixing time number and the Reynolds number. It was shown that the magnetic field can be applied successfully to mixing liquids.

Keywords: rotating magnetic field, mixing time, hydrodynamics, mixing effect

1. INTRODUCTION

The mixing process is very often applied in chemical engineering systems and is the subject of many experimental investigations. This process is often realised by means of the mixing tank or stirred vessel and it may be described by various parameters (Zlotarnik, 2001).

The mixing time and power consumption of the agitator or mixing time are important parameters for a mixer or reactor design (Harnby et al., 2000; Stręk, 1981). Power consumption is a basic quantity in a mixing process that, in part, determines other process quantities, e.g. mixing time. It should be also noticed that the cost of a process depends on the power consumption (King et al., 1988). In many situations, the correct knowledge of the power consumption and the mixing time are needed for better design and operation of the various types of mixers (Hiraoka et al., 2001).

The mixing time can be compared with mass transfer time or reaction time when evaluation of the controlling mechanism of the process is of interest (Bouaifi and Rousatn, 2001). This parameter represents one the most useful criteria for characterization of the mixing system design, scaling-up and optimization of the mixing process (Jaworski et al., 2000; Karcz et al., 2005). This parameter contains information about hydrodynamics and mixing within the mixer and can be useful for the scaling up (Cascaval et al., 2004). The design process of a novel type of mixer closely depends on knowledge of hydrodynamics in the mixing vessel. Therefore, the mixing time is often used as an indication of the effectiveness of a mixing system (Kordas et al., 2013). The mixing time denotes the time required for the tank composition to achieve a specified level of homogeneity following the addition of a tracer pulse at a single point in a mixer (Hadjiev et al., 2006). This parameter is also defined as the time

*Corresponding authors, e-mail: alicja.przybyl@zut.edu.pl

needed to reach a given mixing intensity when starting from the completely segregated situation (Oniscu et al., 2002).

The mixing performance of stirred tanks equipped with various types of agitators has been analyzed by many researchers (Masiuk and Rakoczy, 2007; Masiuk et al., 2008). Most investigations have examined the mixing time and power consumption of agitation systems resulting in empirical correlations (Bouaifi and Roustan, 2001; Manjula et al. 2009; Szoplik and Karcz, 2008; Woziwodzki et al., 2010; Zadghaffari et al., 2006).

A novel approach to the mixing process focuses on the application of a rotating magnetic field (RMF). This kind of magnetic field may be used to augment the process intensity instead of mechanical intensity (Rakoczy, 2013). It should be noticed that RMF may act as a non-instructive mixing device (Moffat, 1965; Moffat, 1991).

The main motivation for the present work was to investigate the possibility of the mixing system provided with a generator of RMF for the mixing process of various types of liquids, including water, NaCl solutions, Hestrin–Schramm medium (as an example of the microbiological medium used in the biotechnological process of bacterial cellulose production). The interaction of the applied magnetic field (MF) with liquids can be described by the relation between the mixing time and the Reynolds numbers. These dimensionless numbers allow for quantitative representation and characterization of the influence of the hydrodynamic condition under the RMF action on the mixing process.

2. THEORETICAL BACKGROUND

The mixing time, defined as the time needed to reach a specific degree of homogeneity, is defined by means of a dimensionless mixing time defined by the formula (Rakoczy, 2013):

$$\Theta = f\left(\mathrm{Re}_{RMF}\right) \tag{1}$$

The above relation includes a non-dimensional group characterizing the mixing time problem, expressed in the formula (Kordas, 2013):

$$\Theta = \frac{t_{95}\,\nu}{D^2} \tag{2}$$

To characterize the mixing process under the action of the magnetic field, the Reynolds number based on the frequency of the RMF may be used in the following form (Story et al., 2016):

$$\mathrm{Re}_{RMF} = \frac{\Omega_{RMF}\,D^2}{\nu} \tag{3}$$

The parameter Ω_{RMF} may be expressed as follows (Moffat, 1965):

$$\Omega_{RMF} = \frac{w_\varphi\big|_{\max}}{D} \tag{4}$$

The maximum peripheral speed of the mixed liquid under the action of the RMF may be expressed as (Dahlberg, 1972):

$$w_\varphi\big|_{\max} = B_{\max} D \sqrt{\frac{\omega_{RMF}\,\sigma_e}{\rho}} \tag{5}$$

3. MATERIALS AND METHODS

3.1. Experimental apparatus

Investigations were performed using the experimental apparatus shown in Fig. 1. The experimental apparatus consisted of a cooling jacket (1) and a generator of RMF (2). The RMF was generated by the 3-phase stator of the squirrel cage induction motor. The power of the stator winding used 3-phase alternating current. The container (3) was axially aligned with the RMF generator. The mixing system consisted of a vessel of 145 mm inner diameter and 415 mm height. The a.c. transistorized inverter (4) was used to adjust the RMF frequency, *f*, in the range of 10-50 Hz, and to regulate the maximum voltage in the range of 10-100 V. This inverter was connected with a personal computer (5) equipped with software to control the RMF generator. Additionally, recorders (6) with electrodes (7) were used to measure the mixing time.

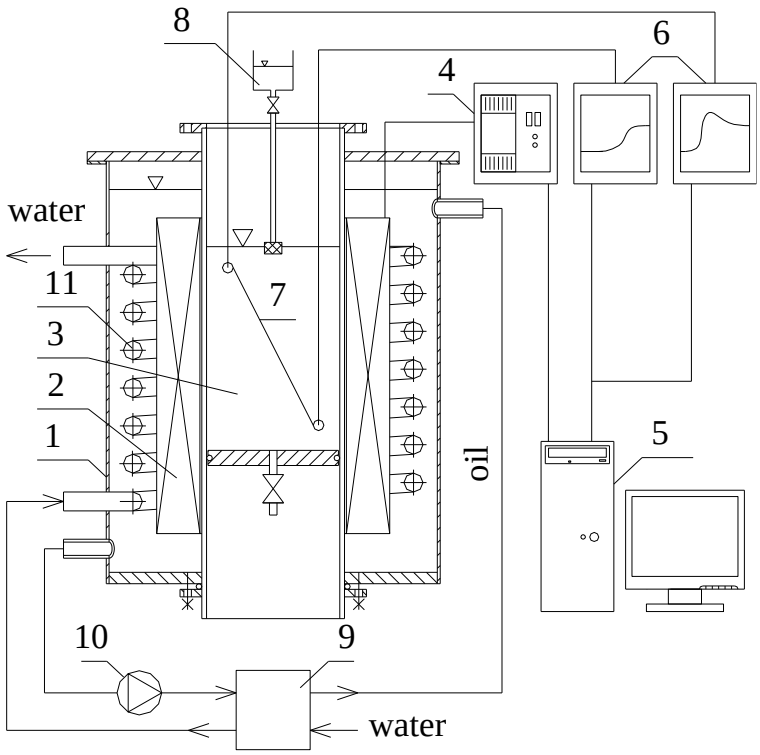

Fig. 1. Scheme of experimental apparatus: 1 - cooling jacket, 2 - RMF generator, 3 – vessel, 4 - a.c. transistorized inverter, 5 - personal computer, 6 – recorders (CX-701), 7 – electrodes, 8 – batcher, 9 – heat exchanger, 10 – pump, 11 – internal coil

The tracer, (sodium hydroxide solution; 1 mol·dm^{-3}) was introduced into the working liquid using the batcher (8). The temperature of the analyzed liquids during the exposition to the RMF was controlled by an additional cooling system based on oil circulation (in a heat exchanger (9) and a pump (10) and water circulation system in an internal coil (11).

3.1.1. Working liquids

A total of 5 dm^3 liquid was introduced into the glass container. Aqueous solutions of NaCl brine, distilled water and Herstin-Schramm (HS) medium composed of glucose (2 w/v%), yeast extract (0.5 w/v%), bacto-pepton (0.5 w/v%), citric acid (0.115 w/v%,) Na_2HPO_4 (0.27 w/v%), $MgSO_4 \cdot 7H_2O$ (0.05 w/v%) and ethanol (1 v/v%) (Ciechańska et al., 1998). The HS medium is an example of the

microbiological growth medium used in the biotechnological process of bacterial cellulose production (Fijałkowski et al., 2015). The temperature of the analyzed liquids was equal to 20°C. This parameter was monitored using the special temperature sensors cooperating with the recorder.

The physical parameters of the applied fluids are given in Table 1.

Table 1. Physical properties of tested liquids (for temperature T = 20°C)

Medium	ρ, kg·m^{-3}	η, Pa·s	σ_e, A^2·s^3·kg^{-1}·m^{-3}
distilled water	998	0.001002	0.05
4% w/w NaCl brine	1027	0.001068	6.35
8% w/w NaCl brine	1056	0.001145	14.00
Hestrin–Schramm (HS) medium*)	986	0.000944	0.65

*) *Viscosity of H-S medium was obtained using a capillary viscometer*

3.1.2. Mixing time measurements

The mixing time was determined using the pH tracer method (Kushalkar and Pangarkar, 1994). The values of this parameter were determined by means of top injections of 1 M NaOH used as a tracer. The top injection means that the tracer is added at the top of the vessel, 1 cm under the liquid surface and in the middle of the tested apparatus. All injections were performed with a batcher. The time injection was equal to 6 s.

Two pH electrodes were used as follows: one probe mounted at 10 mm from the vessel bottom; another probe was mounted opposite the bottom pH electrode. Both were connected to the recorder (CX-701). The localization of the electrodes and the injection point are shown in Fig. 2.

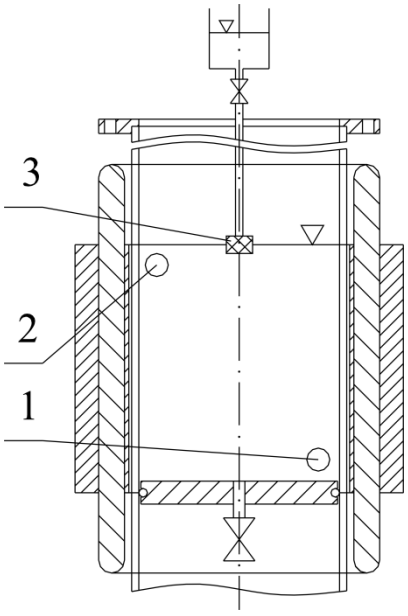

Fig. 2. Localization of the pH electrodes (1, 2) and the injection point (3)

As a tracer, 50 ml of sodium hydroxide solution (1 mol·dm^{-3}) was injected. The pH tracer method was based on measurements of pH difference response caused by the tracer (1 M NaOH). The mixing process was completed when the pH of the mixed liquid stopped changing. The time to reach, $t_{95,}$ (95% of the concentration step change from starting point to end point concentration) was defined as the

mixing time, that is, the time necessary to render the liquid well-mixed. This parameter is defined as a time required for the system to mix the liquid to a prescribed final state and can be represented by the following relationship:

$$Y = \frac{\left|pH\left(t\right) - pH_0\right|}{\left|pH_\infty - pH_0\right|} \tag{6}$$

where pH_0 and pH_∞ are the initial and the final pH values; pH(t) is the value of pH at some instant in time t.

A typical example of the pH transient process is shown in Fig. 3. As shown in this figure, the mixing time t_{95} for distilled water is much higher in comparison with the H-S medium.

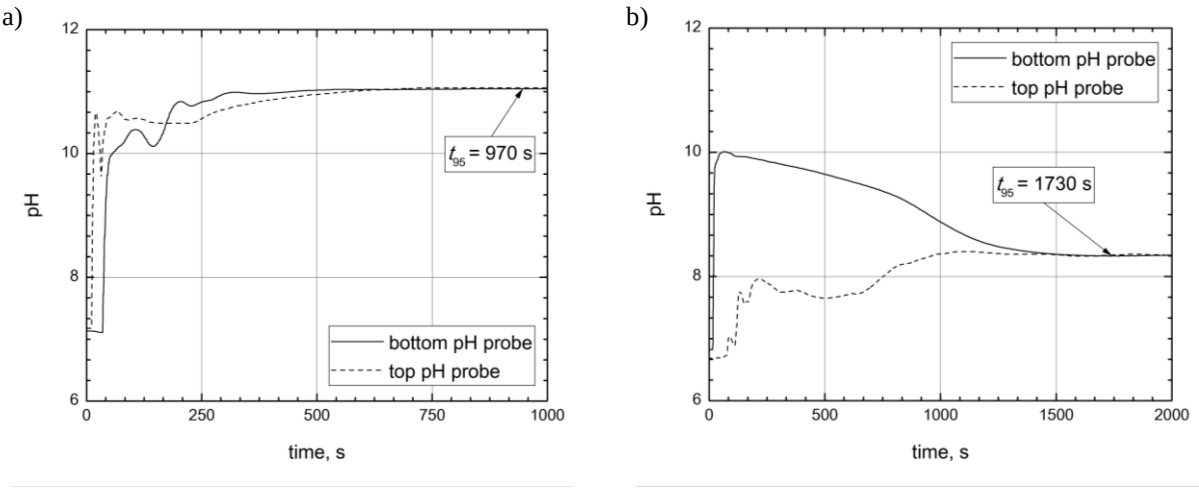

Fig. 3. Typical example of pH transient processes (pH changes during mixing time investigation) at f = 30 Hz for: a) H-S medium, b) distilled water

The mixing time is defined as the time required for the normalized probe output to reach and remain between 95 and 105% (±5%) of the final equilibrium value. This value is called the 95% mixing time or t_{95} (Magelli et al., 2013). To obtain an overall mixing time for the system, two probe responses must be combined and must be weighted toward the probe showing the largest concentration deviation to ensure that all regions of the vessel are mixed. This is achieved by means of the RMS variance (Paul et al., 2004).

3.1.3. Magnetic field patterns

The values of magnetic induction at different points inside the vessel are detected by means of microprocessor magnetic induction sensors connected with Hall probe. The measuring points were located on a plane that coincides with the axial section of the RMF generator. It should be noticed that the values of magnetic induction were recorded for about 110 points. Then, the averaged values of the magnetic field, B_{avg}, were calculated as the arithmetic mean of these measurements.

As follows from the analysis of experimental data, the values of magnetic induction are spatially distributed in the volume of the RMF generator and may be presented in a system of coordinates (R^*, H^*) in the form of iso-contour patterns (see Fig. 4). The normalized values of the radius, R^*, and the height, H^*, of a glass container, were defined as $R^* = R / R_{max} \rightarrow R^* = R / 0.075$ m and $H^* = H / H_{max} \rightarrow H^* = H / 0.2$ m.

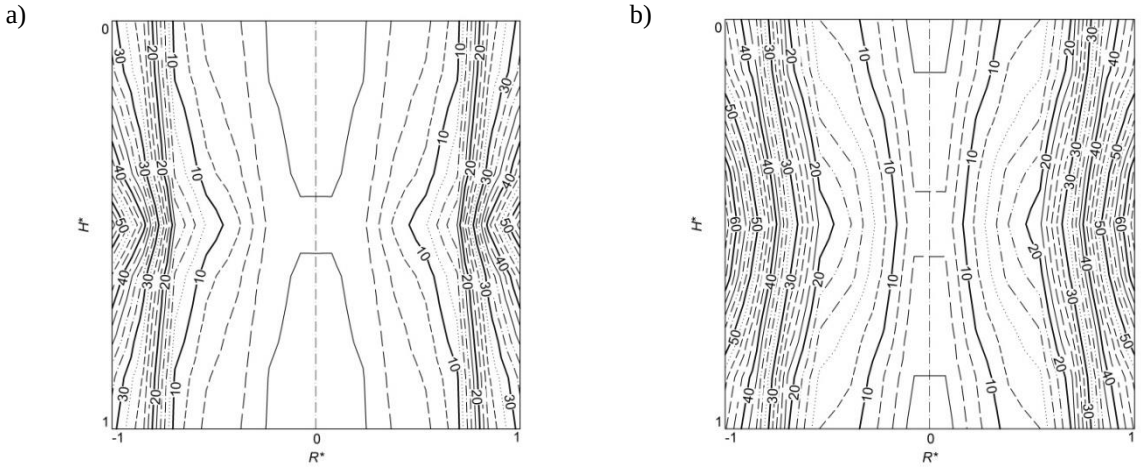

Fig. 4. A typical example of magnetic field patterns: a) f = 10 Hz, b) f = 50 Hz

As follows from the experimental database, the values of the magnetic induction, B, are spatially distributed. This distribution is depended on the RMF frequency, f. On the basis of the experimental measurements, the maximum values of magnetic induction, B_{max}, were obtained. These values were recorded at the point (R^* = -1 or 1; H^* = 0.5) inside the RMF generator. In order to establish the effect of the maximum and the averaged values of the magnetic field, the obtained results are graphically shown in Fig. 5.

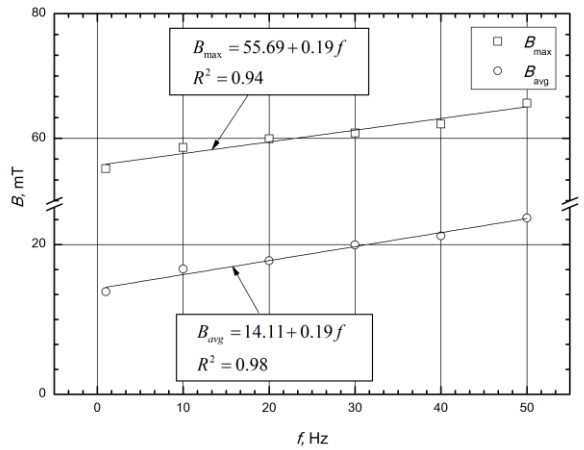

Fig. 5. Graphical presentation of relations between the maximum and averaged values of magnetic induction and RMF frequency

4. RESULTS AND DISCUSSION

Taking into account Eq. (1) and the basic parameters from Eqs (2) and (3), the following relationship was obtained:

$$\Theta = f\left(\mathrm{Re}_{RMF}\right) \Rightarrow \left(\frac{t_{95}\nu}{D^2}\right) = f\left(\frac{\Omega_{RMF} D^2}{\nu}\right) \Rightarrow \left(\frac{t_{95}\nu}{D^2}\right) = f\left(\frac{w_\varphi\big|_{max}}{D}\frac{D^2}{\nu}\right)$$
$$\Rightarrow \left(\frac{t_{95}\nu}{D^2}\right) = f\left(B_{max} D\sqrt{\frac{\omega_{RMF}\sigma_e}{\rho}}\frac{D}{\nu}\right) \quad (7)$$

According to Eq. (7), the plot of the data obtained in the current work was presented in coordinates (Θ, Re_{RMF}) of the log-log system in Fig. 6.

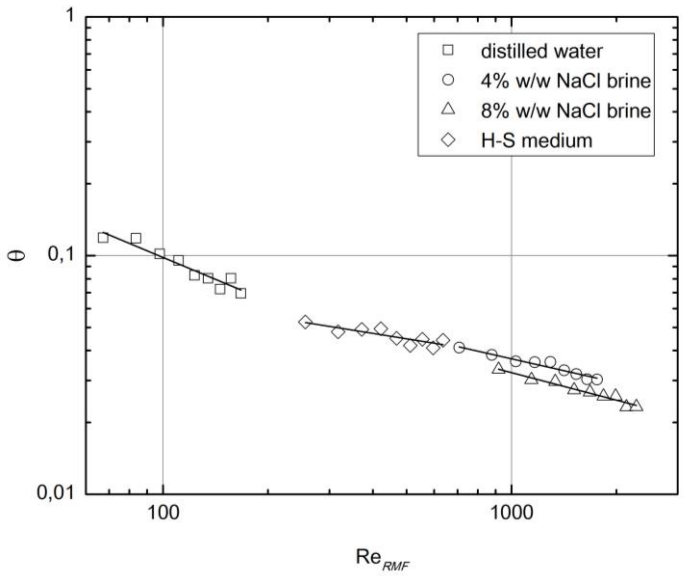

Fig. 6. The dependence of $\Theta = f(Re_{RMF})$ for the analyzed liquids

The experimental results presented in Fig. 6 indicate that the dimensionless mixing number versus the dimensionless Reynolds number may be defined by the following formula

$$\Theta = p_1 \left(Re_{RMF} \right)^{p_2} \tag{8}$$

The constants and exponents were computed by means of Matlab software and the principle of least-squares. These values are collected in Table 2.

Table 2. Physical properties of tested liquids (for temperature T = 20°C)

Medium	p_1	p_2	R^2
distilled water	1.62	-0.60	0.91
4% w/w NaCl brine	0.36	-0.33	0.94
8% w/w NaCl brine	0.46	-0.38	0.96
Hestrin–Schramm (HS) medium	0.19	-0.23	0.74

According to Fig. 6, the scatter of experimental points for the various types of liquids may be described by the same relationship using various values of the coefficients (see Table 2). The results presented in Figure 6 show the influence of the dimensionless Reynolds number on the dimensionless mixing number. Figure 6 indicates also that the mixing time decreases moderately with the increase in the dimensionless Reynolds number. It was found that as the intensity of the magnetic field increased, the time duration of the mixing process under the action of the RMF decreased. Moreover, Fig. 6 shows a strong influence of the liquid on the analyzed mixing process. The dimensionless mixing time obtained for distilled water was consequently higher than that for the HS medium and NaCl solutions. Moreover, a significant decrease took place in the region of large values of the Reynold number. The obtained relationships (see Fig. 6 and data in Table 2) indicate that the mixing time is more sensitive to the dimensionless Reynolds number for distilled water ($\Theta \propto Re^{-0.60}$) than for HS medium ($\Theta \propto Re^{-0.23}$) and both NaCl brine solutions ($\Theta \propto Re^{-0.33}$; $\Theta \propto Re^{-0.38}$).

Following these considerations, RMF may be successfully applied for enhancement of mixing process for various kinds of liquids. It should be noticed that RMF may induce electromagnetic forces in the mixed liquid due to interactions between the induced electric currents and the applied magnetic field (Mehedintu and Berg, 1997). The application of time-varying magnetic field (e.g. RMF) involves the induction of eddy currents in liquids, which are highly conductive due to additional ions added. These eddy currents create their own magnetic field that in a co-operation with the MF used for the exposure, creates small dynamos mixing the liquid at micro-level. Such microscopic dynamos can enhance the mixing process (Hristov, 2010).

The obtained results may also be analytically described by a unique monotonic function. The plot of data obtained in the current work is presented in Fig. 7a. The calculated values from the proposed relationship (see Fig. 7a) for the mixing process under the action of the RMF and the values obtained from the experimental procedures are graphically compared in Fig. 7b. Fig. 7b shows that most results do not exceed the ±15% maximum error.

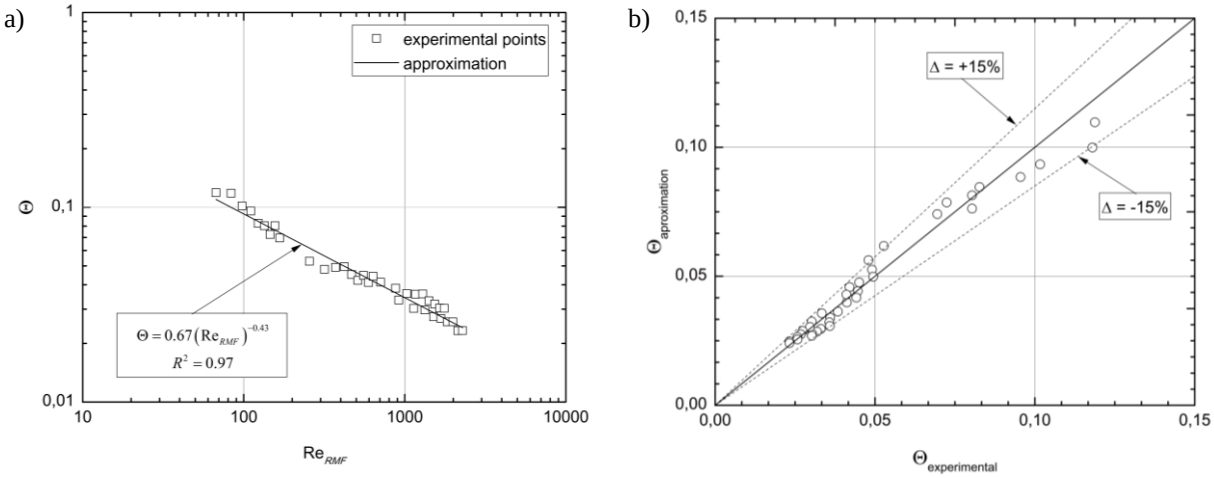

Fig. 7. The dependence of $\Theta = f(\mathrm{Re}_{RMF})$ (a) and comparison of the experimental and calculated values or the dimensionless mixing time number (b)

It should be noticed that the mixing time can be considered as a criterion for comparison of mixing performance of different studied configurations of mixing devices. Therefore, a comparison between the presented results (see Fig. 7) with experimental findings reported in relevant literature should be done. A comparison of the dimensionless mixing time data from this work and previous studies is given in Fig. 8.

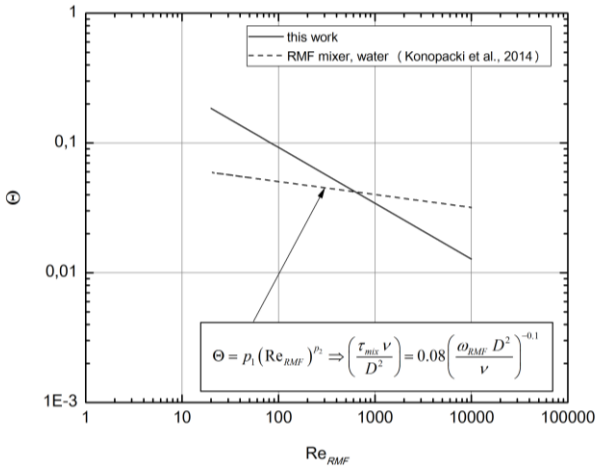

Fig. 8. A comparison of the dimensionless mixing time for systems enhanced by RMF and the RMF mixer (Konopacki et al., 2014)

Konopacki et al. (2014) studied the effect of RMF and various types of magnetic particles on the mixing time. This study has shown that the mixing time for distilled water (working volume equal to 3.3 dm^3) under the action of the RMF (with the variation of the maximum value of the MF in the range between 23 mT and 34 mT) decreases with increasing the dimensionless Reynold number. It can be seen that the obtained values of mixing time are consistent with the information from relevant literature.

The values of the dimensionless mixing time for the tested RMF mixer are higher in comparison with the data given in the previously mentioned literature for the dimensionless Reynolds number $Re_{RMF} < 600$ (Konopacki et al., 2014). A possible explanation for this might be that the applied RMF generator and the working volumes of liquids for the analyzed mixers were different. Manna (1997) proposed that the definition of the mixing time highly depends on the measurement methods, the geometrical configurations of mixers, the system homogeneity and the tool by which the tracer is injected and its location. Therefore, different results of the dimensions mixing time may be explained by the difference between the mixing systems and the use of different methods for mixing time investigations. The current study found that RMF may enhance the mixing process of various types of liquids, e.g.: HS medium, aqueous solutions of brine. As was mentioned above, the magnetic field creates dynamos mixing the liquid at micro-level. These dynamos may be converted into micro-stirrers when the liquid with ions is subjected to RMF. Moreover, micro-stirrers may generate liquid eddies including enhancement of liquid transport properties (Rakoczy, 2013).

5. CONCLUSIONS

The analysis of experimental mixing time for the vessel equipped with a RMF generator in the present study leads to the following conclusions:

- The mixing system with the RMF generator may be successfully applied as a mixer for liquids. The experimental data indicated that the influence of RMF on the mixing intensity strongly depends on the physical parameters of liquids.
- The established mathematical correlations describe unitary of the dependence between the mixing time and the modified Reynolds number. The proposed relationship takes into consideration the operational parameters, which define hydrodynamic state and the intensity of the magnetic effects in the tested apparatus.
- The values obtained for the dimensionless mixing time may be used to compare the mixing process performed by various types of mixing systems. It should be noticed that the values of the dimensionless mixing time number for the mixing system with the RMF generator in the region of the lowest Reynolds numbers are much lower than those for STR with the Rushton turbine.

This study was supported by the National Centre for Research and Development in Poland (Grant no. LIDER/011/221/L-5/13/NCBR/2014).

SYMBOLS

B_{max}	maximum magnetic induction, $kg \cdot A^{-1} \cdot s^{-2}$
D	diameter of container, m
f	frequency of electrical current, s^{-1}
H^*	normalized height of a glass container
pH_0	initial pH values
pH_∞	final pH values

$pH(t)$	value of pH at some instant in time t
R^*	normalized radius of a glass container
Re_{RMF}	Reynolds number for the RMF mixing system
t_{95}	mixing time, s
$w_\varphi\|_{\max}$	maximum peripheral velocity of the mixed liquid under the RMF action, $m \cdot s^{-1}$

Greek symbols

η	dynamic density, $Pa \cdot s^{-1}$
Θ	mixing time number
ν	kinematic viscosity, $m^2 \cdot s^{-1}$
ρ	density, $kg \cdot m^{-3}$
σ_e	electrical conductivity, $A^2 \cdot s^3 \cdot kg^{-1} \cdot m^{-3}$
τ_{mix}	mixing time, s
ω_{RMF}	angular velocity of RMF, $rad \cdot s^{-1}$
Ω_{RMF}	angular velocity of liquid under the action of the RMF, $m \cdot s^{-1}$

REFERENCES

Bouaifi M., Roustan M, 2001. Power consumption, mixing time and homogenisation Energy in dual-impeller agitated gas-liquid reactors. *Chem. Eng. Process.*, 40, 87-95. DOI: 10.1016/S0255-2701(00)00128-8.

Bouaifi M., Roustan M., 2001. Power consumption, mixing time and homogenization energy in dual-impeller agitated gas-liquid reactors. *Chem. Eng. Process.*, 40, 87-95. DOI: 10.1016/S0255-2701(00)00128-8.

Cascaval D., Galaction A.-I., Oniscu C., Ungureanu F., 2004. Modeling of mixing in stirred bioreactors 4. Mixing time for aerated bacteria, yeasts and fungus broths. *Chem. Indust.*, 58, 128-137. DOI: 10.2298/HEMIND0403128C.

Ciechańska D., Struszczyk H., Gruzińska K., 1998. Modification of bacterial cellulose. *Fibres Text. East. Eur.*, 4(23), 61-65.

Dahlberg E., 1972. *On the action of a rotating magnetic field on a conducting liquid.* Aktiebolaget Atomenergi, Studsvik, Nyköping, Sweden.

Fijałkowski K., Żywicka A., Drozd R., Niemczyk A., Junka A.F, Peitler D., Kordas M., Konopacki M., Szymczyk P., El Fray M., Rakoczy R., 2015. Modification of bacterial cellulose through exposure to the rotating magnetic field. *Carbohyd. Polym.*, 133, 52-60. DOI: 10.1016/j.carbpol.2015.07.011.

Gaafar E.-S.A., Hanafy M.S., Tohamy E.Y., Ibrahim M.H., 2008. The effect of electromagnetic field on protein molecular structure of E. coli and its pathogenesis. *Rom. J. Biophys.*, 18, 145–169.

Hadjiev D., Sabiri N.E., Zanati A., 2006. Mixing time in bioreactors under aerated conditions. *Biochem. Eng. J.*, 27, 323-330. DOI: 10.1016/j.bej.2005.08.009.

Harnby N., Edwards M.F., Nienow A.W. *Mixing in the process industries*. Butterworth-Heinemann, Bosotn, 2000.

Hiraoka S., Kato Y., Tada Y., Ozaki N., Murkami Y., Lee Y.S., 2001. Power consumption and mixing time in an agitated vessel with double impeller. *Chem. Eng. Res. Des.*, 79, 805-810. DOI: 10.1205/02638760152721613.

Hristov J., 2010. Magnetic field assisted fluidization—a unified approach. Part 8. Mass transfer: Magnetically assisted bioprocess. *Rev. Chem. Eng.*, 26, 55–128. DOI: 10.1515/REVCE.2010.006.

Jaworski Z., Bujalski W., Otomo N., Nienow A.W., 2000. CFD study of homogenization with dual Rushton turbines — Comparison with experimental results. Part I: Initial studies. *Chem. Eng. Res. Des.*, 78, 327–333. DOI: 10.1205/026387600527437.

King R.L., Hiller R.A., Tatterson G.B., 1988. Power consumption in a mixer. *AIChE J.*, 34, 506-509. DOI: 10.1002/aic.690340320.

Konopacki M., Frąckowiak A., Tabero P., Fijałkowski K., Rakoczy R., 2014. Studies of a mixing process by using the various types of magnetic particles as micro-stirrers. *Technical Transactions. Chemistry*, 24, 45-54.

Kordas M., Story G., Konopacki M., Rakoczy R., 2013. Study of mixing time in a liquid vessel with rotating and reciprocating agitator. *Ind. Eng. Chem. Res.*, 52, 13818-13828. DOI: 10.1021/ie303086r.

Kushalkar K.B., Pangarkar V.G., 1994. Particle — liquid mass transfer in a bubble column with a draft tube. *Chem. Eng. Sci.*, 49, 139-144. DOI:10.1016/0009-2509(94)85041-0.

Magelli F., Montante G., Pinelli D., Paglianti A., 2013. Mixing time in high aspect ratio vessels stirred with multiple impellers. *Chem. Eng. Sci.*, 101, 712-720. DOI: 10.1016/j.ces.2013.07.022.

Manjula P., Kalaichelvi P., Dheenathayalan K., 2010. Development of mixing time correlation for a double jet mixer. *J. Chem. Technol. Biot.*, 85, 115-120. DOI: 10.1002/jctb.2274.

Manna L., 1997. Comparison between psychical and chemical methods for the measurement of mixing time. *Chem. Eng. J.*, 67, 167–173. DOI: 10.1016/S1385-8947(97)00059-4.

Masiuk S., Rakoczy R., 2007. Power consumption, mixing time, heat and mass transfer measurements for liquid vessels that are mixed using reciprocating multiplates agitators. *Chem. Eng. Process.*, 46, 89–98. DOI: 10.1016/j.cep.2006.05.002.

Masiuk S., Rakoczy R., Kordas M., 2008. Comparison density of maximal energy for mixing process using the same agitator in rotational and reciprocating movements. *Chem. Eng. Process.*, 47, 1252–1260. DOI: 10.1016/j.cep.2007.04.004.

Mehedintu M., Berg H., 1997. Proliferation response of yeast Saccharomyces cerevisiae on electromagnetic filed parameters. *Bioelectroch. Bioener.*, 43, 67–70. DOI: 10.1016/S0302-4598(96)05184-7.

Moffatt H.K., 1965. On fluid flow induced by rotating magnetic field. *J. Fluid. Mech.*, 22(3), 521-528. DOI: 10.1017/S0022112065000940.

Moffatt H.K., 1991. Electromagnetic stirring. *Phys. Fluids A*, 3(5), 1336-1343. DOI: 10.1063/1.858062.

Oniscu C., Galaction A-I., Cascaval D., Ungureanu F., 2002. Modeling of mixing in stirred bioreactors: 2. Mixing time for non-aerated broths. *Biochem. Eng. J.*, 12, 61-69. DOI: 10.1016/S1369-703X(02)00042-6.

Rakoczy R., 2013. Mixing energy investigations in a liquid vessel that is mixed by using a rotating magnetic field. *Chem. Eng. Process.*, 66, 1-11. DOI: 10.1016/j.cep.2013.01.012.

Rivera Ch., Foucault S., Heniche M., Espinosa-Solares T., Tanguy P. A., 2006. Mixing analysis in a coaxial mixer. *Chem. Eng. Sci.*, 61, 2895-2907. DOI: 10.1016/j.ces.2005.11.045.

Story G., Kordas M., Rakoczy R., 2016. Correlations for mixing energy in processes using Rushton turbine mixer. *Chem. Pap.*, 70, 747-756. DOI: 10.1515/chempap-2016-0008.

Stręk F. *Mieszanie i mieszalniki*. WNT, Warszawa, 1981.

Szoplik J., Karcz J., 2008. Mixing time of a non-Newtonian liquid in an unbaffled agitated vessel with an eccentric propeller. *Chem. Pap.*, 62, 70-77. DOI: 10.2478/s11696-007-0081-9.

Woziwodzki Sz., Broniarz-Press L., Ochowiak M., 2010. Effect of Eccentricity on transitional mixing in vessel equipped with turbine impellers. *Chem. Eng. Res Des.*, 88, 1607-1614. DOI: 10.1016/j.cherd.2010.04.007.

Zadghaffari R., Moghaddas J. S., Revstedt J., 2007. A mixing study in a double-Rushton stirred tank. *Comput. Chem. Eng.*, 33, 1240-1246. DOI: 10.1016/j.comp-chemeng.2009.01.017.

Zlotarnik M. *Stirring: Theory and practice*. Wiley-VCH, Weinheim, 2001.

Received 28 September 2016
Received in revised form 16 November 2017
Accepted 18 November 2017

www.czasopisma.pan.pl www.journals.pan.pl
Chemical and Process Engineering 2017, 38 (4), 567-576
DOI: 10.1515/cpe-2017-0045

MODIFICATION OF A RECUPERATOR CONSTRUCTION WITH CFD METHODS

Wojciech Ludwig*[1], Daniel Zając[2]

[1]Wroclaw University of Science and Technology, Faculty of Chemistry, Department of Chemical Engineering, Norwida 4/6, 50-373 Wroclaw, Poland

[2]Opole University of Technology, Faculty of Mechanical Engineering, Department of Environmental Engineering, Mikołajczyka 5, 45-271 Opole

The purpose of the work was initial modification of the construction of a commercially produced heat exchanger – recuperator with CFD (computational fluid dynamics) methods, based on designs and process parameters which were provided. Uniformity of gas distribution in the space between the tubes of the apparatus as well as the pressure drop in it were taken as modification criteria. Uniformity of the gas velocity field between the tubes of the heat exchanger should cause equalization of the local individual heat transfer coefficient values and temperature value. Changes of the apparatus construction which do not worsen work conditions of the equipment, but cause savings of constructional materials (elimination or shortening some parts of the apparatus) were taken into consideration.

Keywords: recuperator, modification, CFD, gas flow

1. INTRODUCTION

Finned tube heat exchangers are devices being very commonly used in chemical and power industry, as well as in a number of technological processes. Most often, they are part of another device designed for carrying out required process (Yang et al., 2015). When designing a heat exchanger, it is necessary to calculate the flow resistance of the fluid flowing through the device (Pal et al., 2016). Values of the resistances affect proper selection of the required pressure level for pumping the medium through the exchanger and thus, the selection of pumping device. Application of increased flow velocities intensifies the heat exchange process; the convective transfer coefficient is being increased, which allows reduction of the device's dimensions, thereby reducing the capital costs. However, the increase of velocity means increased resistance to flow, which leads to higher consumption of energy ensuring adequate pressure, and this can even imply the need for buying bigger pumping device, which generates higher operating and capital costs. The problem of calculating flow resistance in inter-pipe space is sophisticated, due to the complex nature of the flow (Wen et al., 2015). Besides the above-mentioned, ensuring uniform flow of the medium in the tube bundle is an extremely important task from the perspective of utilizing the widest possible heat exchange surface area, and prolonging the lifetime of pipes. In case of improper flow distribution of the working fluid stream, some of the pipes in bundle can be insufficiently surrounded with the fluid flowing at uniform velocity, which reduces the overall efficiency of the heat exchanger. The second problem of irregular fluid flow distribution is formation of dead zones, and this, in case of high fluid temperatures, can increase the risk of thermal damage to individual pipes (Goodarzi and Nouri, 2016).

*Corresponding authors, e-mail: wojciech.ludwig@pwr.edu.pl

Recuperators are the types of heat exchangers being frequently used as an element of heat recovery systems in a variety of technological processes. Location for this type of devices and the available space for mounting them are most often limited by the specific process requirements. It is extremely important that the described exchangers will be possibly characterized by small dimensions and low weight. These characteristics enable installing them in locations inaccessible for traditional units, that often have oversized constructions. Examples of such difficult locations may be ceilings with a small load capacity, some areas of chimneys or even gas transport channels (Gil et al., 2015).

After the review of the current state of knowledge on flow dynamics in heat exchangers, it can be concluded that no work on inlet and outlet unit design optimization deals with the subjects of minimizing flow resistances and distribution of the fluid in particular rows in a tube bundle. There is a lack of research works dealing with inlet and outlet shape optimization in heat exchangers and that is the reason why it is necessary to carry out numerical experiments. One should perform experimental verification of results obtained from numerical calculations in order to optimize the shape of the exchanger parts, so as to reach the assumptions made in the research work.

The purpose of the study was to develop an initial concept of recuperator design modification. The conceptual works were focused on determining new geometrical parameters to ensure uniform gas flow in the inter-pipe space or to reduce the size and weight of the applied device. Computational fluid dynamics (CFD) was used during research, which at current state of computer development is a very useful alternative to classical methods of optimization and design, especially for one phase flows (Jaworski, 2005; Chang et al., 2015).

2. FLOW AND DESIGN ASSUMPTIONS FOR CFD ANALYSIS

The data base for CFD calculations were: a design of the device being manufactured (Fig. 1) and limit values of gas operating parameters in the inter-pipe space, which were supplied by the producer: temperature: 500 – 100 ^{o}C, velocity 2 - 6 m/s, overall pressure drop 100 - 500 Pa. Air was the medium that flowed through the apparatus.

Because the modeling of heat transfer in the test device was not envisaged, a number of simplifications were made in the geometry of the CFD model. The spaces inside the tubes were omitted, as well as their gas inflow areas. Such fastening elements as flanges, screws, etc. were not included. The calculation domain has been limited to the main body of the device with a short section of the inlet and outlet pipes (Fig. 2).

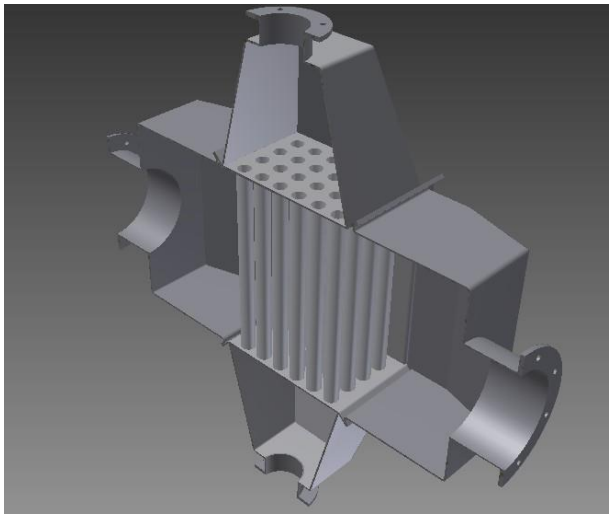

Fig. 1. Pictorial drawing of the produced recuperator design

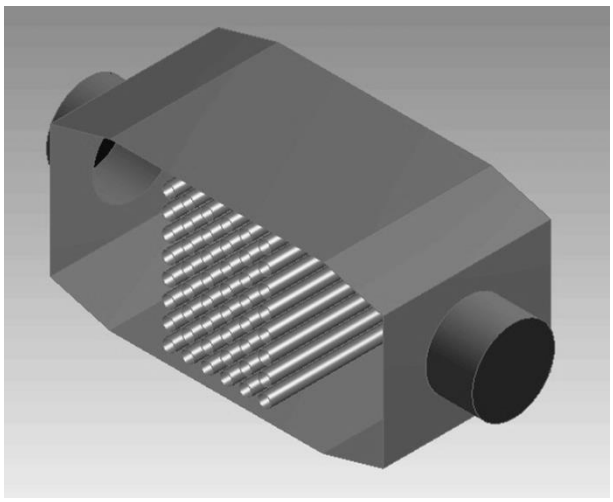

Fig. 2. The simplified geometry of the recuperator used in the CFD model

The research began with tests on numerical meshes of different densities and cell distributions. Finally, a hybrid mesh, mostly with tetrahedral cells was applied inside the device. Moreover, in order to maintain proper density and adequate values of the wall functions in the boundary zone, a high density five-layer mesh with hexahedral cells was introduced (Fig. 3).

A test for checking solution independence on mesh density was carried out. For the mesh with three times greater density (three times more cells), the values of volume integrals of velocity, pressure, k and ε changed on average by about 10%, which was considered as a satisfactory value for quality calculations.

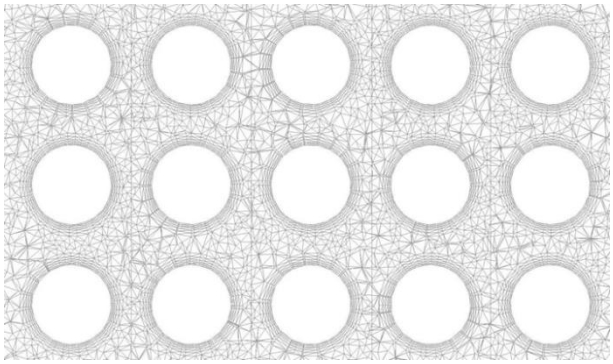

Fig. 3. Part of longitudinal section of numerical mesh in the pipe area used in standard recuperator

Table 1. Basic parameters of the numerical mesh used in calculations of the standard device

Parameter of the mesh	Value
Number of cells	2259620
Number of nodes	787718
Minimum volume of the cell	1.723365×10^{-9}
Maximum volume of the cell	8.623437×10^{-7}
Maximum skewness	0.95

Based on the values of the Reynolds number, it was found, that the turbulent flow was present in the device, for the description of which standard k-ε model was used. The initial stage of the research study also covered the optimization for solver settings (Ansys Fluent 15). Finally, a set of values was gained

(Table 2). It allowed obtaining a stable solution at the lowest number of iterations (1000). Calculations were continued until scaled residuals reached the values below 10^{-4} and the volume integrals of pressure, velocity, k and ε were constant. The impact of temperature on the hydrodynamics of flow was taken into account by changing physical properties of the air, constant in the entire volume of the devices. The air density and viscosity for a given temperature were computed from the ideal gas and Sutherland equations, respectively.

Table 2. Solver parameter constants in all simulations

Simulation parameter	Value
Solver	3D, pressure based
Turbulence model	k-ε standard constants
Boundary layer description	standard wall function
Boundary condition at the inlet	velocity inlet
Boundary condition at the outlet	pressure outlet
Boundary condition for walls	wall, no slip, no heat exchange
Relaxation coefficients	all 0.1
Discretization	second order upwind

The velocity at the inlet of the device was set in such a way that the mean velocity calculated for the empty inter-pipe space was in the range listed in hydrodynamics specifications (2 - 6 m/s).

3. RESULTS IN THE STANDARD APPARATUS

At the beginning of the analysis of the standard equipment work a number of simulations were done for changing temperature of gas in the device (100 – 500 °C). Velocity and pressure fields were obtained for extreme but possible gas velocities in the space between the tubes (2 - 6 m/s). In the entire range of the air flow velocity, the pressure drop was below the permissible value (500 Pa) (Fig. 4), but non-uniform flow of gas around the tubes of the heat exchanger occurred (Figs. 5 and 6).

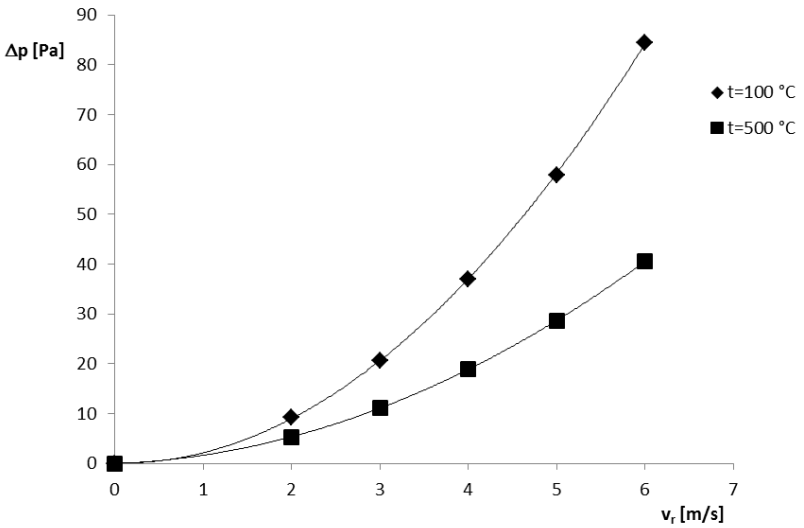

Fig. 4. Pressure drop in the standard device as a function of the average velocity in inter-pipe space

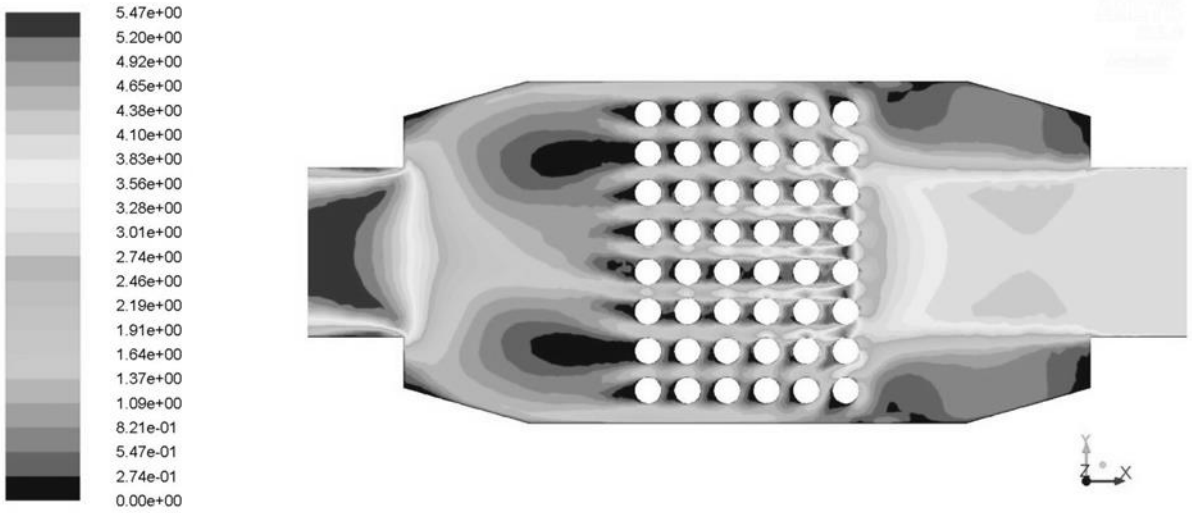

Fig. 5. Air velocity (in m/s) contours inside the longitudinal section of the standard apparatus (t = 100°C, v_r = 2 m/s, inlet on the right)

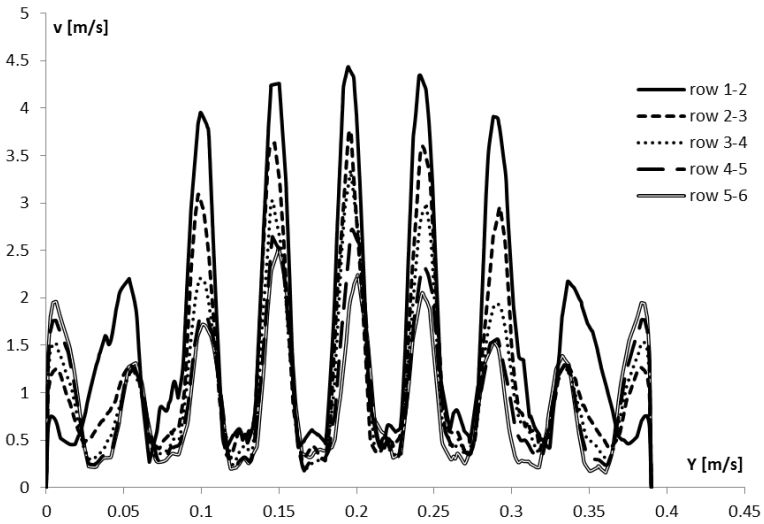

Fig. 6. Gas flow velocity in the cross section of the produced recuperator between different pipe rows in the heat exchanger (v_r = 2 m/s, t = 100 °C)

Inter-pipe flow velocities are the highest in rows opposite the inlet pipe (Fig. 5). At these areas, velocities are often above the assumed maximum values (in front rows, they are more than doubled) (Fig. 6). The greater the distance from the inlet tube, the lower the air velocity in a given row. This is caused by poor inlet air stream flow distribution, which does not cover the entire inter-pipe cross-section. As the distance from the inlet of the device in subsequent inter-pipe gaps in the exchanger is increasing, the gas velocity field is becoming more uniform. The gas passes from rows opposite the inlet tube to rows located closer to the solid walls of the device (Figs. 5 - 6).

The examined device is characterized by irregular gas flow around pipes of the heat exchanger. Air stream flowing from the narrow inlet pipe into the wide chamber of the equipment has not got space to increase its cross section. Almost the whole of air flows through the width of exchanger comparable to the diameter of the inlet pipe. Therefore, in further sections of the research study several design approaches are suggested to eliminate or to reduce the impact of the abovementioned adverse phenomena.

4. HEAT EXCHANGER MODIFICATION PROPOSITIONS AND CFD ANALYSIS

Based on the performed CFD analysis, work was undertaken for formulating modification proposals for the recuperator: the change of inlet and outlet pipe diameter, decreased length of inlet and outlet section, systems of baffles extending the inlet air stream on all rows of pipes. Among all of the tested designs, five were selected, which are characterized either by improvement in gas flow parameters (more homogenous inter-pipe air flow in the heat exchanger) or by causing weight reduction of the units without flow quality-decrease, when compared to the standard device.

Table 3. Comparison of flow parameters for different modification propositions for recuperator designs (v_r = 6 m/s, t = 100 °C, average velocity for profile between the 1st and 2nd row of pipes)

No.	Short description	Δp [Pa]	w [m/s]	Figure
X	Standard device d_r = 200 mm	84	4.9	5
1	Best solution, considering pressure drop and uniform flow throughout the device with extended diameter of inlet pipe of d_r = 300	33	2.9	7
2	Size reduction of the unit's body (without the connecting pipes and flanges) from 782 mm to 582 mm by removing the element with fixed cross-section area	88	5.4	8
3	Size reduction of the unit's body (without the connecting pipes and flanges) from 782 mm to 500 mm by removing the element with variable cross-section area	90	5.1	9
4	Adding flow guide in perpendicular direction to pipes of the exchanger	89	4.4	10
5	Adding two flow guides in perpendicular and parallel direction to pipes of the exchanger	106	4.1	11

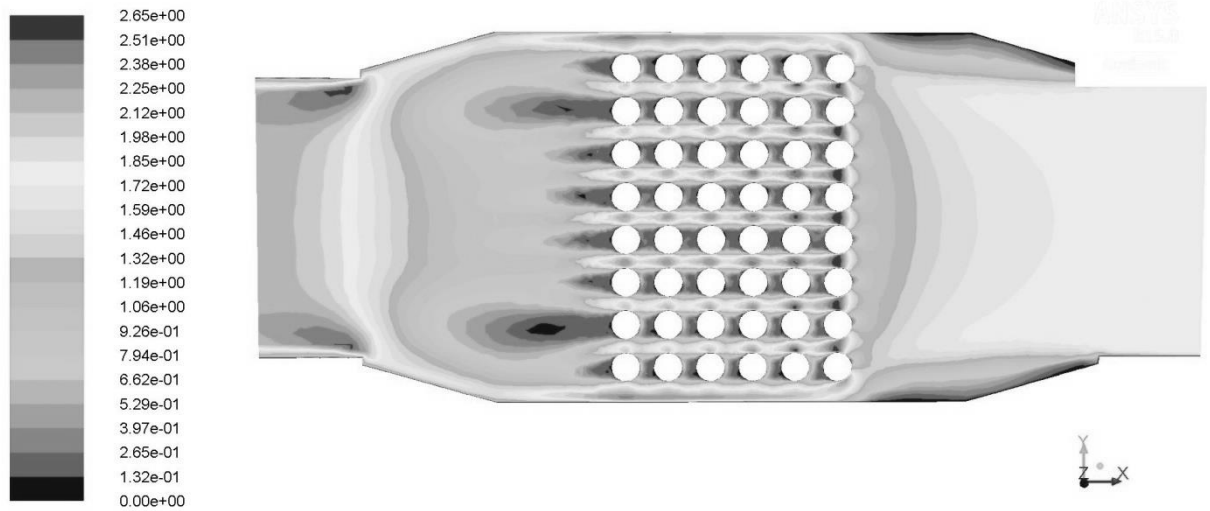

Fig. 7. Air velocity (in m/s) contours inside the longitudinal section of the modified apparatus, proposition 1, (d_r = 300 mm, t = 100 °C, v_r = 2 m/s, inlet on the right)

After increasing the outer diameter of the inlet pipe from 200 to 300 mm (proposition 1, Table 3) contours of the gas flow are becoming harmonized already in the first inter-pipe gaps (Figs. 7 and 12).

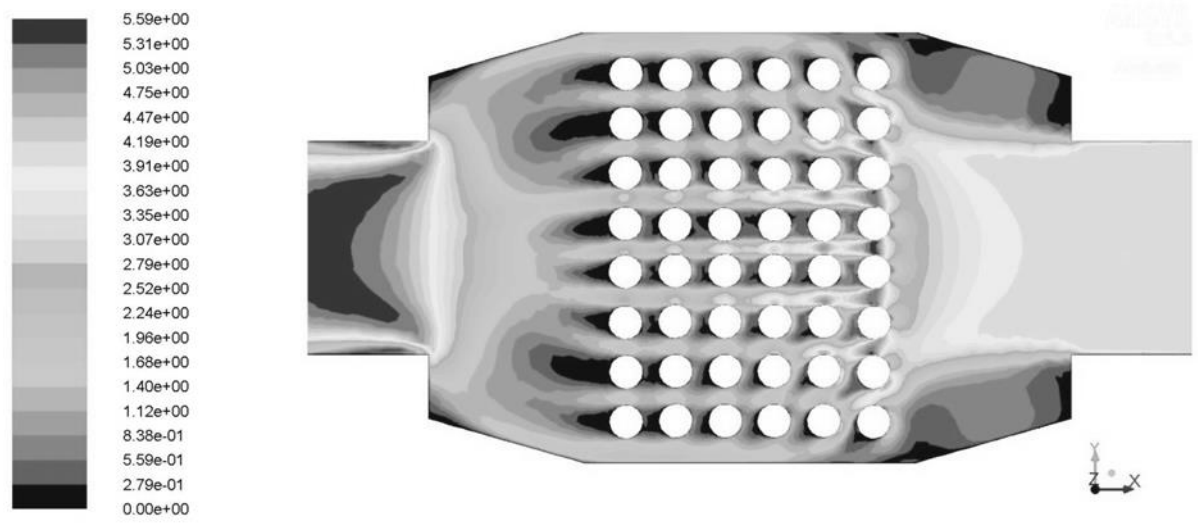

Fig. 8. Air velocity (in m/s) contours inside the longitudinal section of the modified apparatus, proposition 2, (t = 100 °C, v_r = 2 m/s, inlet on the right)

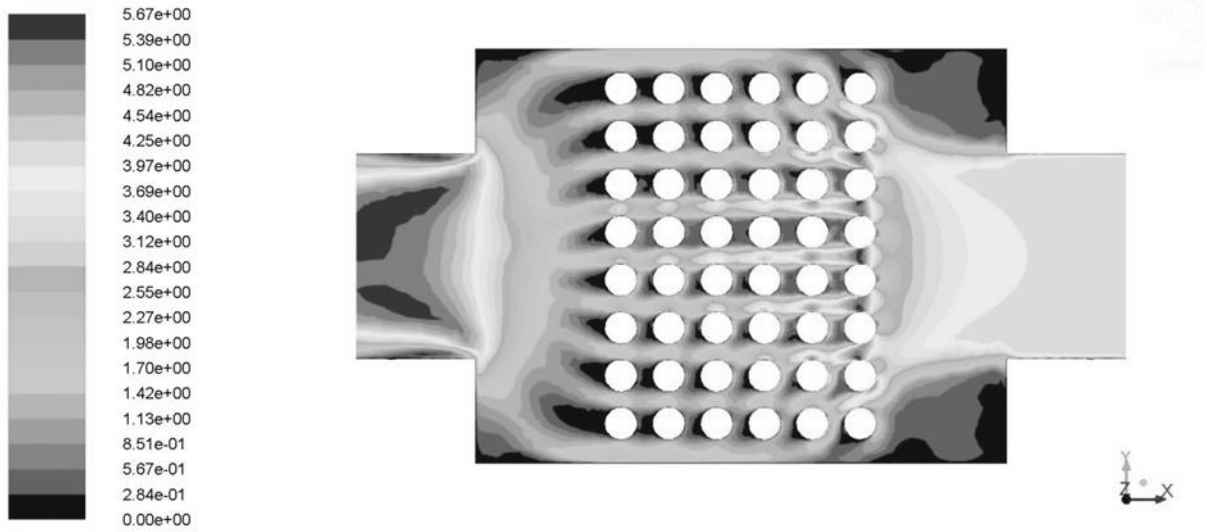

Fig. 9. Air velocity (in m/s) contours inside the longitudinal section of the modified apparatus perpendicular do the pipes, proposition 3, (t = 100 °C, v_r = 2 m/s, inlet on the right)

Local velocities are within the assumed range of values (between 2 and 6 m/s), nearly in the entire volume of the heat exchanger. For the highest gas inlet velocity, the maximum velocity between the 1st and the 2nd rows exceeds slightly (by 8 %) the assumed maximum velocity of 6 m/s; for the lowest inlet velocity in the last layer area (5th and 6th rows), it drops slightly (by 10 %) below the value of 2 m/s. As the distance from the inlet of the apparatus increases, the mean velocity changes a little (by 12 and 8 % for the lowest and the highest gas inlet velocity, respectively).

The inlet and outlet element design changes (propositions 2 and 3, Table 3) do not lead to changes in the profile of inter-pipe flow velocity in the heat exchanger of the examined devices (Figs. 8 - 9, and 12). In all modifications, the distance between the inlet of the device and pipes of the exchanger was so small that the gas stream had no time to extend above the diameter of inlet pipe. The analyzed modifications slightly increase the pressure drop in the device (by up to 5-7 % for the highest gas inlet velocity).

Modification 4 (Table 3) with the large opening angle of baffles (Fig. 10) extends the air stream in such a way that in the inter-pipe gaps, in the proximity of solid walls of the device, velocity increases. However, behind the baffle a dead zone with low gas velocity is formed, which causes velocity drop in the inter-pipe gaps behind the barrier (Figs. 10 and 12). This design causes slight increase in pressure drop (6% for v_r = 6 m/s).

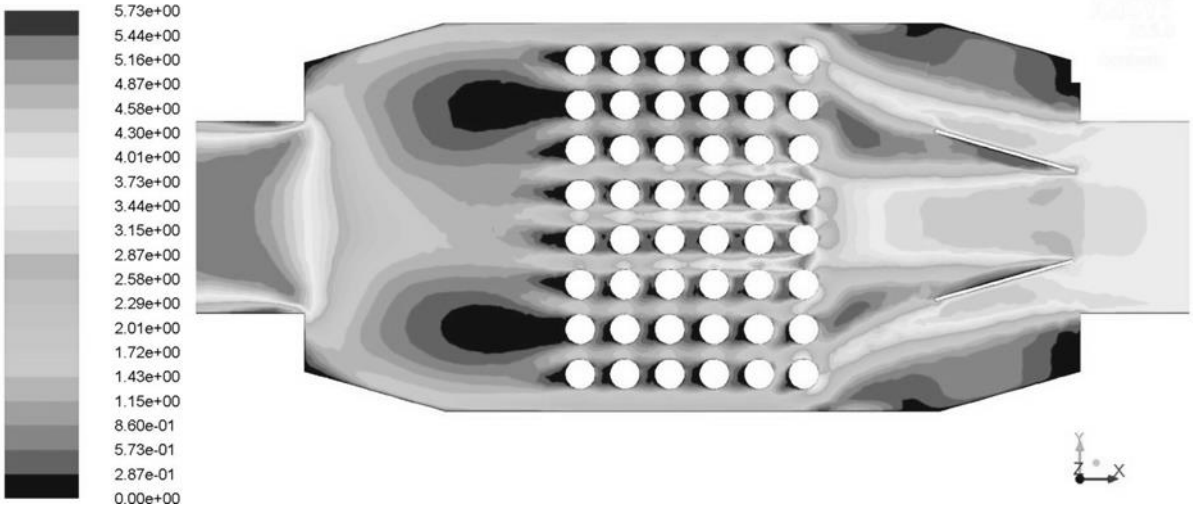

Fig. 10. Air velocity (in m/s) contours inside the longitudinal section of the modified apparatus perpendicular to the pipes, proposal 4, (t = 100 °C, v_r = 2 m/s, inlet on the right)

Modifications 2 - 4 were related with cross-section perpendicular to pipes of the heat exchanger. Therefore, the outcome of air flow guides, extending the stream crosswise and alongside the pipes of the heat exchanger was analyzed. Based on proposition 4, a revised design was proposed by adding two transverse plates of a longer size.

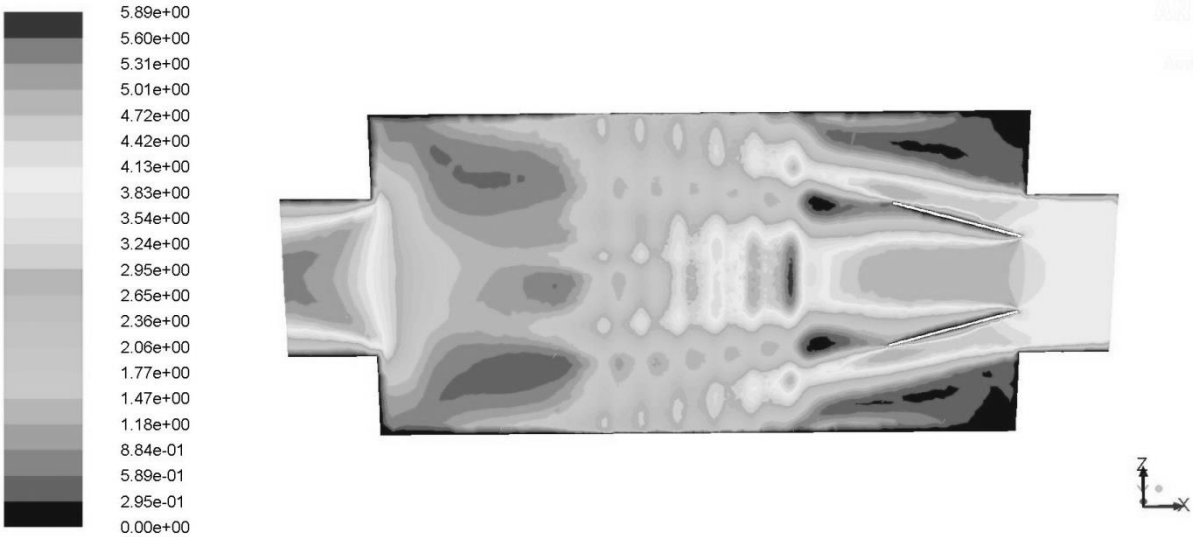

Fig. 11. Air velocity (in m/s) contours inside the longitudinal section of the modified apparatus parallel to the pipes, proposition 5, (t = 100 °C, v_r = 2 m/s, inlet on the right)

The suggested design of baffles leads to changes in air flow, both in parallel and perpendicular cross-section to pipes of the heat exchanger. Behind flow guides there are zones with reduced gas velocity, which is directed toward pipes closed to solid walls of the unit (Figs. 11 and 12). The proposed design causes significant increase of pressure drop in the device (by 26 % for v_r = 6 m/s).

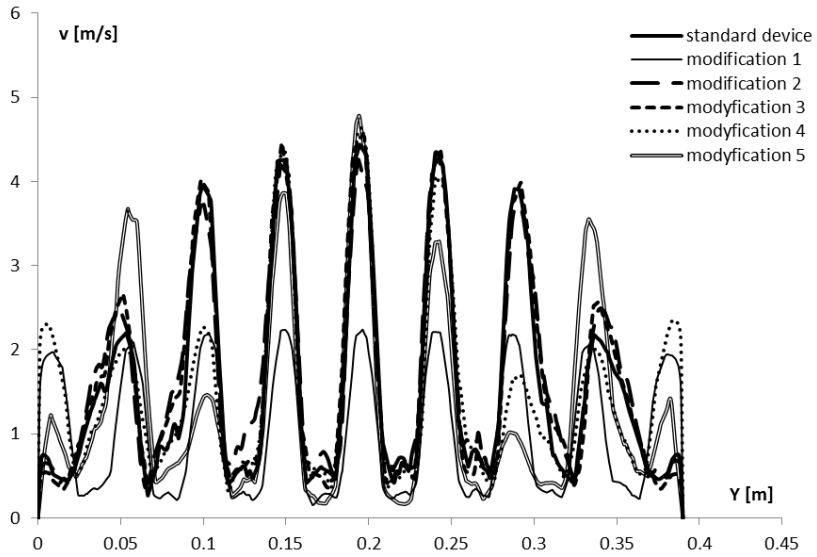

Fig. 12. Gas flow velocity in the cross section between 1st and 2nd row of pipes in the recuperator for different modifications (v_r = 2 m/s, t = 100°C)

5. CONCLUSIONS

Out of the tested modifications, proposition 1 seems to be the best construction, which is characterized by improvement in gas flow parameters: more homogenous inter-pipe gas flow in the heat exchanger and smaller pressure drop (by 60 % for v_r = 6 m/s). In this case one can take into account the increase of apparatus mass. Modifications 2 and 3 do not reduce the quality of the gas flow (velocity profiles and overall pressure drop are comparable to those in the standard recuperator), but they can decrease the mass of the device. Modifications 4 and 5 cause more homogenous inter-pipe gas flow in the heat exchanger and increase pressure drop and mass of the apparatus. Final conclusions on design change can be made only if experimental research tests are implemented with prototypes that will confirm the accuracy of the obtained results.

The studies were funded by the National Centre for Research and Development as a part of the project POIG.01.04.00-16-288/13.

SYMBOLS

d_r	inlet pipe external diameter, m
Δp	overall pressure drop in the apparatus, Pa
t	temperature, °C
v_r	average velocity calculated on the cross section of inter-pipe space, m/s
v	local velocity, m/s
w	average velocity calculated on the cross section of the empty apparatus, m/s
Y	distance from the wall parallel to heat exchanger pipes in recuperator, m

REFERENCES

Chang T.H., Lee C.H., Lee H.S., Lee K.S., 2015. Velocity profiles between two baffles in a shell and tube heat exchanger. *J. Therm. Sci.*, 4, 356-363. DOI: 10.1007/s11630-015-0795-x.

Gil S., Góral J., Horňak P., Ochman J., Wiśniewski T., 2015. Pressurized recuperator for heat recovery in industrial high temperature processes. *Arch. Metall. Mater.*, 60, 1847-1852. DOI: 10.1515/amm-2015-0315.

Goodarzi M., Nouri E., 2016. A new double-pass parallel-plate heat exchanger with better wall temperature uniformity under uniform heat flux. *Int. J. Therm. Sci.*, 102, 137-144. DOI: 10.1016/j.ijthermalsci.2015.11.012.

Jaworski Z., 2005. *Numeryczna mechanika płynów w inżynierii chemicznej i procesowej*, Akademicka Oficyna Wydawnicza Exit, Warszawa.

Pal E., Kumar I., Joshi J.B., Maheshwari N.K., 2016. CFD simulations of shell-side flow in a shell-and-tube type heat exchanger with and without baffles. *Chem. Eng. Sci.*, 143, 314-340. DOI: 10.1016/j.ces.2016.01.011.

Wen J., Yang H., Wang S., Xue Y., Tong X., 2015. Experimental investigation on performance comparison for shell-and-tube heat exchangers with different baffles. *Int. J. Heat Mass Transfer*, 84, 990-997. DOI: 10.1016/j.ijheatmasstransfer.2014.12.071.

Yang F., Zeng M., Wang Q., 2015. Numerical investigation on combined single shell-pass shell-and-tube heat exchanger with two-layer continuous helical baffles. *Int. J. Heat Mass Transfer*, 84, 103-113. DOI: 10.1016/j.ijheatmasstransfer.2014.12.042.

Received 25 September 2016
Received in revised form 20 October 2017
Accepted 18 November 2017

www.czasopisma.pan.pl www.journals.pan.pl
Chemical and Process Engineering 2017, 38 (4), 577-585
DOI: 10.1515/cpe-2017-0046

SIMULTANEOUS VELOCITY MEASUREMENT OF PHASES IN A LIQUID-GAS SYSTEM

Radosław Musoski, Jacek Stelmach*

Lodz University of Technology, Faculty of Process and Environmental Engineering, ul. Wólczańska 213, 90-924 Łódź, Poland

Results of velocity measurements of liquid and gas bubbles in a tank with a self-aspirating disk impeller are analysed. Studies were carried out using a fluorescent dye tracer in the measuring system with two cameras (simultaneous phase velocity measurement) and with one camera (sequential measurement of phase velocity). Based on a comparative analysis of the acquired data it was found that when differences in the phase velocities were small the simultaneous velocity measurement gave good results. However, sequential measurement gives greater possibilities for setting the measuring system and if the analysis of instantaneous velocities is not necessary, it seems to be a better solution.

Keywords: fluorescence, self-aspirating impeller, phase velocity, PIV

1. INTRODUCTION

The determination of velocity in a two-phase liquid-gas system is an important processing problem. When liquid is a continuous phase then relative velocity of gas bubbles in the liquid and energy dissipation rate (which may be calculated from velocity fluctuations) affect mass transfer coefficient and bubble size (Alves et al., 2004; Bröder and Sommerfeld, 2002; Garcia-Ochoa and Gomez, 2004; Lau et al., 2014; Linek et al., 2004; Millies and Mewes, 1999; Zhou and Kresta, 1998). On the other hand, when gas is a continuous phase, the velocity of liquid droplets can influence the process of bed humidification (Heim et al., 2004, Heim et al., 2008). However, it is difficult to determine the velocity of both phases. In the case of very small bubbles their population can be divided into two groups and – assuming that the trajectories of small bubbles are the mapping of liquid motion – velocities of the phases can be determined (Deen et al., 2002; Gui et al., 1997; Kiger and Pan, 2000; Stelmach and Kuncewicz, 2011). New possibilities have emerged after the advent of the measurement methods of PIV (Particle Image Velocimetry) (Aubin et al., 2004; Delnoij et al., 2000; Sathe et al., 2010) and PLIF (Planar Laser Induced Fluorescence). A fluorescent dye used in PLIF measurement can be included in trace particles (or liquid droplets) (Lindken and Merzkirch, 2002). Emitting secondary radiation the dye is used to obtain light with two wavelengths in the measuring system, i.e. the wavelengths of laser light and fluorescent dye. This radiation can be separated by optical filters. This allows us to separately analyze the movement of objects which reflect laser radiation and these which emit radiation generated during fluorescence. This measuring system enables a simultaneous measurement of phase velocities but requires the use of two synchronized cameras (Bröder and Sommerfeld, 2000; Chung et al., 2009; Honkanen and Saarenrinne, 2002; Kosiwczuk et al., 2005). Further analysis of this issue leads to a conclusion that in this method a problem may be time intervals between laser pulses, due to which in two frames the shifts of flow tracers are recorded. In the analyzed method such tracers are also gas

*Corresponding authors, e-mail: jacek.stelmach@p.lodz.pl

bubbles and if their velocities are much lower than the continuous phase velocities the recorded shifts will be too small to properly determine the velocity of bubbles on this basis.

The aim of the study was to compare liquid and gas velocities obtained by the PIV method during simultaneous and separate measurements of phase velocities. Results should show how the same time interval between laser pulses selected for one phase affects the accuracy of measurement of the second phase velocity during a simultaneous measurement.

2. EXPERIMENTAL

Measurements were conducted in a flat-bottomed glass tank of diameter T = 292 mm. The tank was equipped with four standard baffles ($B = 0.1 \cdot T$) and filled with water (20 °C) to height H = 300 mm ($H \approx T$). At height h = 75 mm over the bottom there was a self-aspirating disk impeller of diameter D = 125 mm. The impeller rotated at rotational frequency N = 6 s^{-1} (360 min^{-1}) dispersing the gas. The blade tip velocity was equal to U_{tip} = 2.36 m/s. The Reynolds number for the mixing process was Re = 93750 and the modified Froude number was $Fr' = N^2 \cdot D^2/[g \cdot (H - h)] = 0.255$. In these conditions the gas phase hold-up was Φ = 0.4% (Stelmach, 2000). The cylindrical tank was placed in a rectangular tank filled with water. This system of tanks reduced distortions caused by the curvature of the cylindrical tank wall (Stelmach, 2014). Under these conditions Sauter diameter of bubbles is equal to d_{32} = 1.59 mm. Bubble size distribution is log-normal with highest number of bubbles in the range from 0.2 to 0.6 mm (Stelmach, 2006; Stelmach, 2007). However, the bubbles flowing out of the orifices are about 5-8 mm in size (Stelmach and Rzyski, 2003).

Velocity measurements were made by the PIV method using a *LaVision* measuring system. A light knife about 1 mm thick cut the tank in a vertical plane symmetrically between the baffles. The light knife was generated by a double-pulse Nd:YAG laser emitting light of a wavelength λ = 532 nm with the highest frequency of 15 Hz. Tracer particles of size from 1 μm to 20 μm containing the fluorescent dye Rhodamine B were added to water. Under the influence of laser light the dye emits radiation at a wavelength λ = 553 nm.

Two settings of the measuring system were used:

- In the simultaneous measurement of liquid and gas velocities two *ImagerPro 4M* cameras (2048 px × 2048 px matrix, 14 bit grayscale) were used. Their optical axes were open at an angle of about 16° (Fig. 1a). One camera was equipped with a low-pass filter which cut off radiation with a wavelength greater than λ = 532 nm. The other camera had a high-pass filter cutting off radiation with a wavelength shorter than λ = 540 nm. Rays reflected from the interface reached the first camera, while these formed as a result of fluorescence reached the second one. Time interval between laser pulses was $\Delta\tau$ = 207 μs and $\Delta\tau$ = 1500 μs, respectively. In this measurement two pairs of images were obtained. The interrogation area of both cameras was 60 mm×60 mm. Perspective distortions were corrected on the basis of data acquired during the measuring system calibration.
- During separate (sequential) velocity measurements one *ImagerPro 4M* camera was applied. Its optical axis was perpendicular to the interrogation area (Fig. 1b). During water velocity measurements there was a low-pass filter on the camera lens and displacements of the tracer particles were recorded. In this case time interval between laser pulses was $\Delta\tau$ = 207 μs. While measuring the displacement of air bubbles the camera was equipped with a high-pass filter and time interval between laser pulses was $\Delta\tau$ = 1500 μs. The interrogation area was about 70 mm×70 mm.

In each case a series of 300 images (quadruple for setting (1) or double for setting (2)) was taken. Then, the images underwent two-pass processing using the *DaVis* 7.2 software. The interrogation area had the

final size of 64 px×64 px. A relatively large size of this area was adopted because of the size of gas bubbles. As a result of calculations the field of vectors of averaged axial and radial velocities was obtained. On the basis of velocity components the resultant velocity and angle between the vector of this velocity and level were calculated. For the PIV method it is difficult to estimate the velocity measurement error. Errors can be caused by poor estimation of the time interval $\Delta\tau$ between laser pulses.

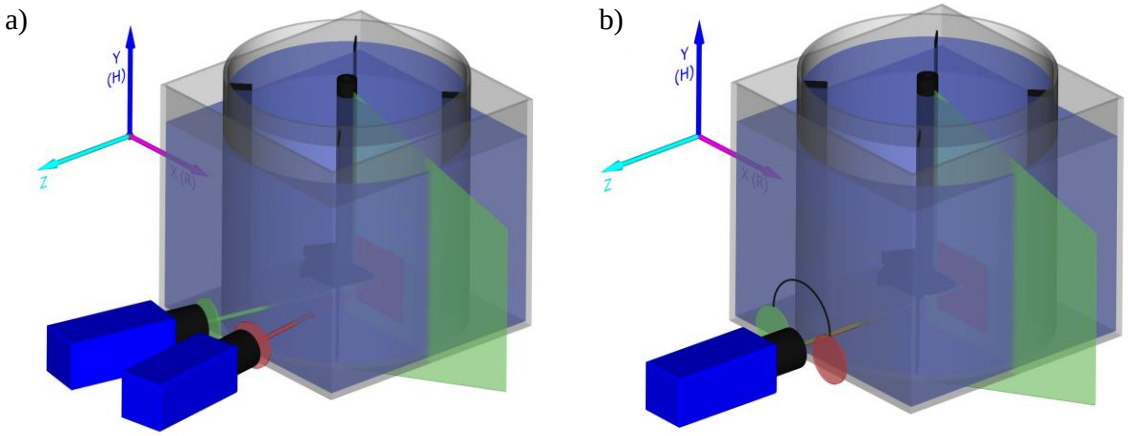

Fig. 1. Setting of the cameras and light knife during measurements, a) two cameras with filters - simultaneous measurement of phase velocity, b) one camera - sequential measurement with filter change

3. RESULTS AND DISCUSSION

3.1. Water velocity

In our earlier studies (Stelmach, 2014) the distribution of dimensionless radial and axial velocities was determined at the height of the impeller in a one-phase system when the impeller did not disperse gas. The reference velocity was the peripheral velocity of the blade tip. Results are shown in Fig. 2. Based on these measurements the required time interval between laser pulses was specified.

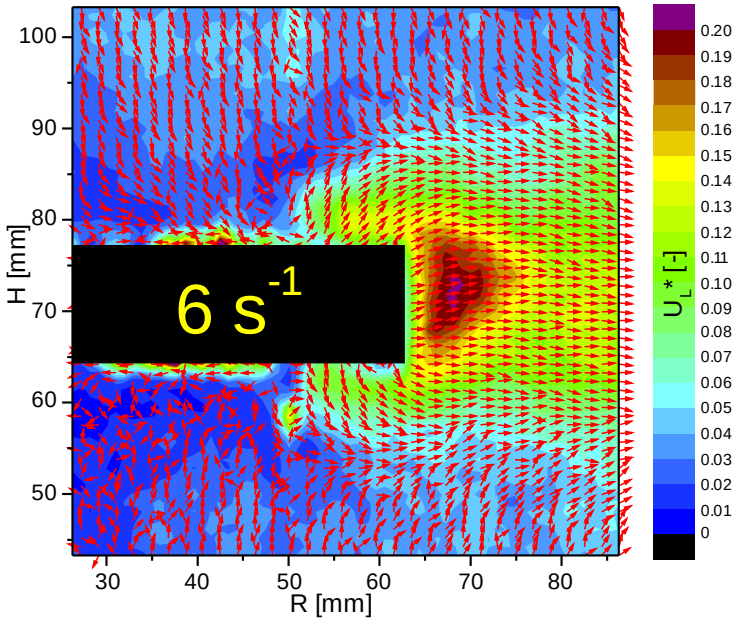

Fig. 2. Dimensionless average water velocities in the one-phase system for N = 6 s^{-1}

Since for process parameters the hold-up of the gas phase and therefore the number of bubbles is small, the results for the one-phase system can be treated as comparative (reference) data for the liquid phase. Figure 3 shows water velocity maps obtained during simultaneous (a) and separate (b) measurements. Due to changes in the equipment setting the interrogation areas in both cases are slightly different.

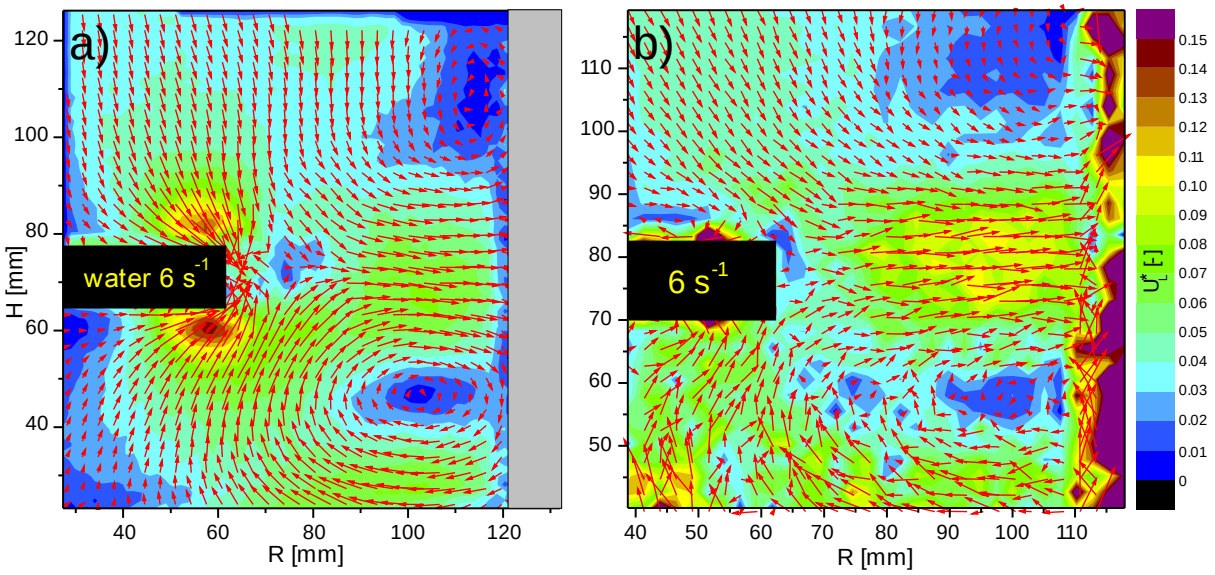

Fig. 3. Dimensionless average water velocities in two phase system in simultaneous (a) and separate (b) velocity measurements for $\Delta\tau$ = 207 μs

The analysis of Fig. 3 shows that for these parameters similar water velocity distributions were obtained. The reasons of worse ordering of vectors in Fig. 3b can be as follows:

- different frequency of laser flashes which makes the position of the blade relative to the baffles change. This, as found in the previous studies (Heim and Stelmach, 2011), has an influence on the average velocity field;
- the aging of the fluorescent dye and changes in light emission (tracer particles remained in the liquid for a few days during which the tests were made).

In turn, a comparison of Figs. 2 and 3 leads to a conclusion that gas bubbles leaving the impeller outlets change the flow of liquid at a small distance from the blade tips. In a one-phase system, at a small distance from the blade tip liquid velocities are the highest (about 20% of impeller tip velocity U_{tip}). In the two-phase system in such place slow liquid velocities (only 5% of U_{tip}) are observed because there is the highest concentration of gas bubbles and the interphase surface can strongly diffuse light, leading to a decrease water velocity. By contrast, outside the impeller zone (5 mm above and under impeller plates, 15 mm outside impeller tip) the circulation of liquid in the one- and two-phase system is almost identical and equal to several percent of U_{tip}. Because in the region near the blade tips of the self-aspirating impeller the highest mass transfer coefficients were reported this is a very important problem which requires further in-depth studies at various positions of the blade relative to the baffles. With small gas hold-up in the simultaneous (with gas velocity measurement) and separate liquid velocity measurements almost identical liquid velocity fields were obtained.

During simultaneous velocity measurements of liquid and gas bubbles time interval between laser pulses is constant. If there are significant differences in the velocities of phases the interval determined for one phase can be inappropriate for the second phase which can consequently lead to measuring errors. Since gas bubbles should move more slowly than liquid, the measurements were carried out at time interval between laser pulses being $\Delta\tau$ = 1500 μs. Results obtained for this case are shown in Fig. 4.

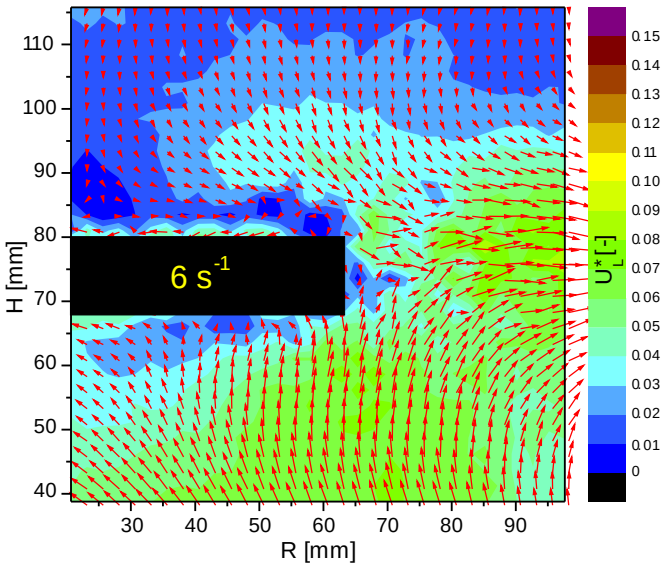

Fig. 4. Dimensionless water velocities in the simultaneous velocity measurement for $\Delta\tau$ = 1500 μs

The longer time interval between laser pulses did not affect significantly the image of liquid circulation and velocity. Figure 4 shows that only below the impeller there is a circulation zone in the direction of the tank axis. As such a zone is not observed in the two-phase system, results obtained for $\Delta\tau$ = 1500 μs seem to be less reliable in this case. This also confirms the need for a proper selection of time interval between laser pulses. The time interval between laser pulses has an influence on results obtained.

3.2. Air velocities

As mentioned earlier, time interval between laser pulses is associated with the displacement of tracer images in both recorded frames. In the case of the gas phase an additional factor influencing final results is the likelihood of incomplete illumination of gas bubbles by the light knife (Honkanen and Sarenrinne, 2002). This problem is illustrated in Fig. 5.

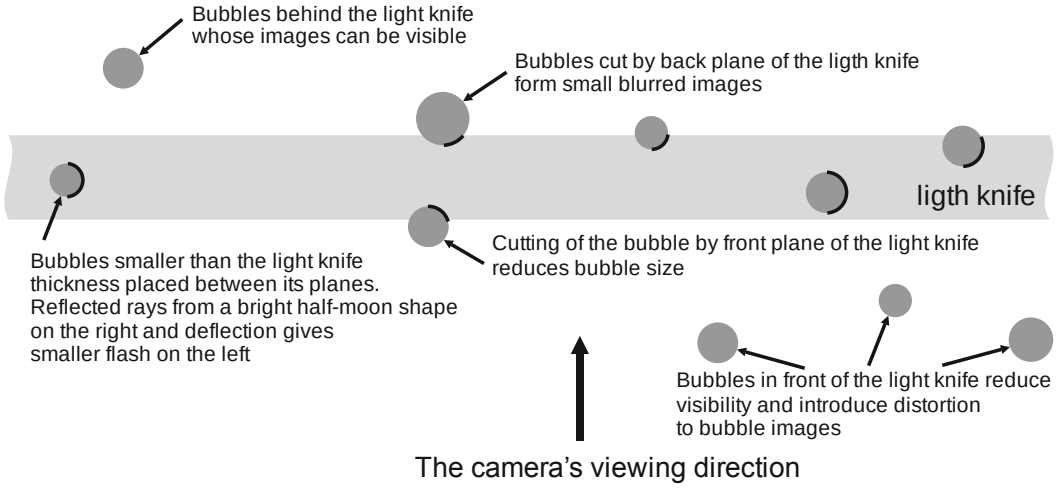

Fig. 5. Lighting of gas bubbles with a light knife

In the two-phase system there is also scattering of light reflected from the surface of bubbles. The scattered light additionally illuminates bubbles located in front of and behind the light knife plane. Therefore the images were binarized to eliminate the effect of background on the measurement. The

ImagerPro 4M cameras differentiate 16,384 levels of brightness. Based on the analysis of images the level of brightness equal to 5,000 was used in binarization. This reduces the number of analyzed objects and it can appear that average velocities determined on the basis of 300 double images will show chaotic velocity vectors, especially in the areas of low concentration of bubbles. This case is illustrated in Fig. 6.

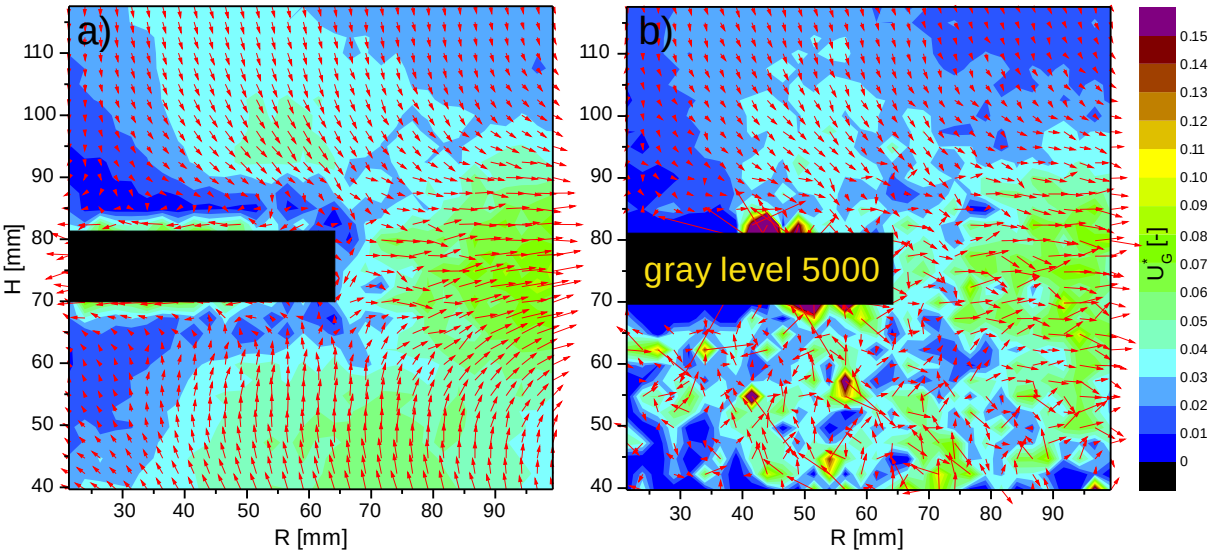

Fig. 6. Comparison of bubble velocity maps obtained on the basis of original (a) and binarized (b) images

In fact, for images subjected to prior binarization below the impeller the average velocity vectors show a large scatter of returns. At the same time, however, a comparison of Figs. 6a and 6b leads to a conclusion that for the assumed level of binarization the velocity differences are very small. This suggests that the impact of the images of bubbles outside the light knife plane is very small.

Bubble velocity maps shown in Fig. 6 were obtained for the time interval between pulses equal to $\Delta\tau = 1500$ μs during the simultaneous velocity measurement. Figure 7 shows the map of bubble velocities for time interval between pulses equal to $\Delta\tau = 207$ μs.

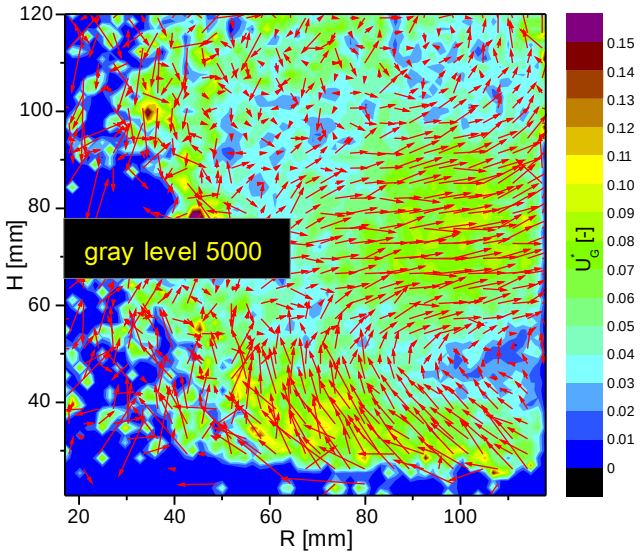

Fig. 7. Gas bubble velocities obtained from binarized images ($\Delta\tau = 207$ μs)

Due to shifting of the fields of camera view in Figs. 6 and 7 there is only a very similar flow of gas bubbles. However, a more accurate comparison of velocities of water and gas bubbles leads to a

conclusion that for interval $\Delta\tau = 207$ μs the velocities of bubbles in the stream flowing from the impeller towards the wall are slightly larger than water velocities determined in the same measurement (Fig. 8).

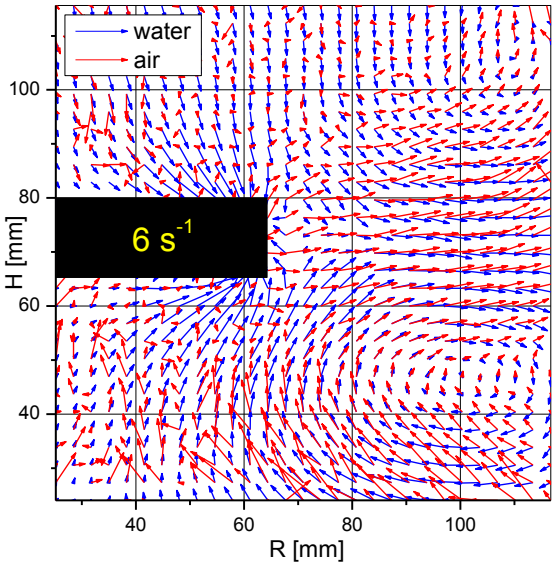

Fig. 8. Comparison of phase velocities for $\Delta\tau = 207$ μs in the simultaneous measurement

In various time intervals during sequential measurements bubble velocities are smaller than water velocity and radial flow from the impeller to the tank wall is observed. However, in this case it seems that interval $\Delta\tau = 1500$ μs assumed for bubble velocity measurement is too big because velocities of the bubble in the radial stream flowing from the impeller to the tank wall are only slightly lower than water velocity.

Determination of a proper interval between laser pulses to measure the velocity of gas bubbles is therefore crucial for the accuracy of results. The importance of this issue comes down to the fact that relative velocities of phases are related to mass transfer rates. Naturally, to obtain correct dependencies it is necessary to carry out similar measurements for peripheral velocity component because the tested type of impeller produces a strong circumferential circulation.

4. CONCLUSIONS

- The use of two cameras and a tracer with fluorescent dye in the PIV system enables a simultaneous measurement of the velocities of liquid and gas bubbles dispersed in it. However, if phase velocities exhibit significant differences, such a measurement can be encumbered with an error difficult to estimate. This error is caused by various shifts of images of the tracer and bubbles in time which elapses between laser pulses. A major problem in this case is such setting of the cameras so that they could cover the same area of the tank.
- In the system with two cameras for simultaneous velocity measurements it is very difficult to obtain the same field in both cameras. In the case of significant non-compliance of these fields it becomes necessary to use interpolation to determine the velocity of one of the phases in the measuring point (in the middle of the area for which the velocity vector is determined).
- Due to differences in the velocity of liquid and gas phases when determining average velocities of the phases, it is more appropriate to measure separately the velocity with one camera. It enables the use of different intervals between laser pulses whose duration is adapted to the phase velocity. Furthermore, for both phases the camera covers the same sector and maintaining the perpendicularity of the optical axis of the camera to the knife light surface correction of the

image distortion is confined to the distortion caused by the curvature of the tank wall. For both phases a different number of frames required to average the velocity can be taken. For the measurement of bubble velocity on the basis of binarized images the assumed sample size is too small.

- A simultaneous recording of images for the liquid and gas phases can be of great importance when studying the flow of liquid around large bubbles.
- The results suggest that there is no need to binarize the images of bubbles. However, studies were carried out for a small gas hold-up. At a greater number of bubbles the bubbles lit by scattered light from the interface can strongly influence the results. It therefore seems appropriate to binarize images for the determined brightness threshold.

The work was completed within the statutory activities of the Department of Process Equipment no. W-10/1/2016/Dz.St.

SYMBOLS

B	baffle width, m
D	impeller diameter, m
g	acceleration of gravity, m/s^2
h	impeller level, m
H	liquid height, m
N	rotational frequency, s^{-1}
U	velocity, m/s
T	tank diameter, m

Greek symbols

Φ	gas hold-up
μ	dynamic viscosity, Pa·s
λ	wavelength of light, nm
ρ	density, kg/m^3
$\Delta\tau$	time interval between laser pulses, μs

Dimensionless numbers

$Fr' = N^2 \cdot D^2/[g \cdot (H - h)]$ modified Froude number for mixing process

$Re = N \cdot D^2 \cdot \rho/\eta$ Reynolds number for mixing process

REFERENCES

Alves S.S., Maia C.I., Vasconcelos J.M.T., 2004. Gas-liquid mass transfer coefficient in stirred tanks interpreted through bubble contamination kinetics. *Chem. Eng. Process. Process Intensif.*, 443, 823-830. DOI: 10.1016/S0255-2701(03)00100-4.

Aubin J., Le Sauze N., Bertrand J., Fletcher D.F., Xuereb C., 2004. PIV measurements of flow in an aerated tank stirred by a down- and an up-pumping axial flow impeller. *Exp. Therm Fluid Sci.*, 28, 447-456. DOI: 10.1016/j.expthermflusci.2001.12.001.

Bröder D., Sommerfeld M., 2000. A PIV/PTV system for analysing turbulent bubbly flows. *10th International Symposium on Applications of Laser Techniques to Fluid Mechanics*, Lisbon, Portugal, 10-13 July 2000.

Bröder D., Sommerfeld M., 2002. Experimental studies of bubble interaction and coalescence in a turbulent flow by an imaging PIV/PTV system. *11th International Symposium on Applications of Laser Techniques to Fluid Mechanics*, Lisbon, Portugal, 8-11 July 2002.

Chung K.H.K., Simmons M.J.H., Barigou M., 2009. Local gas and liquid phase velocity measurement in a miniature stirred vessel using PIV combined with a new image processing algorithm. *Exp. Therm Fluid Sci.*, 33, 743-753. DOI: 10.16/j.expthermflusci.2009.01.010.

Deen N.G., Westerweel J., Delnoij E., 2002. Two-phase PIV in bubbly flows: Status and trends. *Chem. Eng. Technol.*, 25, 97-101. DOI: 10.1002/1521-4125(200201)25:1.

Delnoij E., Kuipers J.A.M., van Swaaij W.P.M., Westerweel J., 2000. Measurement of gas-liquid two-phase flow in bubble columns using ensemble correlation PIV. *Chem. Eng. Sci.*, 55, 3385-3395. DOI: 10.1016/S0009-2509(99)00595-3.

Garcia-Ochoa F., Gomez E., 2004. Theoretical prediction of gas-liquid mass transfer coefficient, specific area and hold-up in sparged stirred tanks. *Chem. Eng. Sci.*, 59, 2489-2501. DOI: 10.1016/j.ces.2004.02.009.

Gui L., Lindken R. Merzkirch W. 1997. Phase-separated PIV measurements of the flow around systems of bubbles rising in water. *ASME Fluids Engineering Division Summer Meeting*.

Heim A., Gluba T., Obraniak A., 2004. The effect of the wetting droplets size on power consumption during drum granulation. *Granular Matter.*, 6, 137-143. DOI: 10.1007/s10035-004-0169-7.

Heim A., Gluba T., Obraniak A., Błaszczyk M., Gawot-Młynarczyk E., 2008. The effect of wetting liquid droplet size on the properties of drum-granulated product. *Przemysł Chemiczny*, 87 (2), 150-153 (in Polish).

Heim A., Stelmach J., 2001. The comparison of velocities at the self-aspirating disk impeller level. *Przemysł Chemiczny*, 90(9), 1642-1646 (in Polish).

Honkanen M., Saarenrinne P., 2002. Turbulent bubbly flow measurements in a mixing vessel with PIV. *11th International Symposium on Applications of Laser Techniques to Fluid Mechanics*, Lisbon, Portugal, 8-11 July 2002.

Kiger K.T., Pan G., 2000. PIV technique for the simultaneous measurement of dilute two-phase flows. *J. Fluids Eng.*, 122, 811-818. DOI: 10.1115/1.1314864.

Kosiwczuk W., Cessou A., Trinité M., Lecordier B., 2005. Simultaneous velocity field measurements in two-phase flows for turbulent mixing of sprays by means of two-phase PIV. *Exp. Fluids*, 39, 895-908. DOI:10.1007/s00348-005-0027-3.

Lau Y.M., Bai W., Deen N.G., Kuipers J.A.M., 2014. Numerical study of bubble break-up in bubbly flows using a deterministic Euler-Lagrange framework. *Chem. Eng. Sci.*,108, 9-22. DOI: 10.1016/j.ces.2013.12.034.

Lindken R., Merzkirch W., 2002. A novel PIV technique for measurements in multiphase flows and its application to two-phase bubbly flows. *Exp. Fluids*, 33, 814-825. DOI: 10.1007/S00348-002-0500-1.

Linek V., Kordač M., Fujasová M., Moucha T., 2004. Gas-liquid mass transfer coefficient in stirred tanks interpreted through models of idealized eddy structure of turbulence in the bubbly vicinity. *Chem. Eng. Process. Process Intensif.*, 43, 1511-1517. DOI: 10.1016/j.cep.2004.02.009.

Millies M., Mewes D., 1999. Interfacial area density in bubbly flow. *Chem. Eng. Process. Process Intensif.*, 38, 307-319. DOI: 10.1016/S0255-2701(99)00022-7.

Sathe M.J., Thaker I.H., Strand T.E., Joshi J.B., 2010. Advanced PIV/LIF and shadowgraphy system to visualize flow structure in two-phase bubbly flows. *Chem. Eng. Sci.*, 65, 2431-2442. DOI: 10.1016/j.ces.2009.11.014.

Stelmach J. 2000. *Investigation of self-aspirating disk impeller work*. PhD thesis, Politechnika Łódzka (in Polish).

Stelmach J. 2006. Bubble sizes in the initial phase of self-aspirating, *Chemical Engineering and Equipment*, 6s, 225-227 (in Polish).

Stelmach J. 2007. Distribution of gas bubble sizes at the beginning of self-aspirating, *Chemical Engineering and Equipment*, 4-5, 117-119 (in Polish).

Stelmach J. 2014. *Hydrodynamics of two-phase liquid-gas system. Use of photooptics methods.*. Monografie Politechniki Łódzkiej, Łódź (in Polish).

Stelmach J., Kuncewicz Cz., 2011. Liquid and gas buble velocities at the level of a self-aspirating disk impeller. *Przemysł Chemiczny*, 90 (9), 1680-1685 (in Polish).

Stelmach J., Ryzski E., 2003. The outflow of gas bubbles from a self-aspirating impeller. *Inżynieria i Aparatura Chemiczna*, 5s, 192-194 (in Polish).

Zhou G., Kresta S.M., 1998. Correlation of mean drop size and minimum drop size with the turbulence energy dissipation and the flow in an agitated tank. *Chem. Eng. Sci.*, 53, 2063-2079. DOI: 10.1016/S0009-2509(97)00438-7.

Received 12 October 2016
Received in revised form 21 November 2017
Accepted 20 November 2017

DE GRUYTER OPEN
www.czasopisma.pan.pl PAN POLSKA AKADEMIA NAUK www.journals.pan.pl
Chemical and Process Engineering 2017, 38 (4), 587-588
DOI: 10.1515/cpe-2017-0047
PAN

ACKNOWLEDGMENTS TO REVIEWERS 2017

Herewith the Editorial Committee of the Chemical and Process Engineering quarterly (Inżynieria Chemiczna i Procesowa) expresses our sincere words of gratitude to all peer-reviewers for their concerted efforts at assessment of manuscripts submitted in 2017. The evaluation concerned both the formal requirements as well as scientific merit of the submissions. We are thankful for the honest and invaluable work of all the referees, which highly contributed to the recent growth in the scientific standing and dissemination of our quarterly. The reviewers' names are listed below.

LIST OF REVIEWERS 2017

Abiev Rufat
Ambrosewicz-Walacik Marta
Ameur Houari
Bałdyga Jerzy
Berezowski Marek
Beris Anthony N.
Bińk Andrzej
Bizukojć Marcin
Bresser Dominic
Bueck Andreas
Chwojnowski Andrzej
Continillo Gaetano
Czub Piotr
Dembczyński Radosław
Di Maio Ernesto
Douglas Timothy
Dunnet Sarah
Dziubiński Marek
Eibl Regine
Ferrari Michele
Florides Georgios
Ford Warren T.
Gierycz Paweł
Gil Stanisław
Gliścińska Eulalia
Guido Stefano
Gumińska Jolanta
Hoffman Pavel
Jarzębski Andrzej
Jasińska Magdalena
Jaworska Małgorzata
Jaworski Zdzisław
Jokiniemi Jorma
Kamiński Władysław
Kawalec-Pietrenko Bożenna
Knez Željko
Koniuszy Adam
Krasiński Andrzej
Królikowski Lechosław
Kupecki Jakub
Kuncewicz Czesław
Kysela Bohuš

Ledakowicz Stanisław
Lemanowicz Marcin
Likozar Blaž
Liu Xiangdong
Lopez Gartzen
Makowski Łukasz
Mei Deqing
Mocek Piotr
Moskal Arkadiusz
Navarro Lopez Maria
Arkadiusz Nędzarek
Nowicki Lech
Ochowiak Marek
Oguntimein Gbekeloluwa B.
Opaliński Ireneusz
Orciuch Wojciech
Pacek Andrzej
Padron Gustavo A.
Press-Broniarz Lubomira
Prochaska Krystyna
Ptaszek Paweł
Rajfur Małgorzata
Rakoczy Rafał
Rożeń Antoni
Saastamoinen Jaakko
Skalska Kinga
Sosnowski Tomasz
Stelmach Jacek
Sun Yongxia
Ściążko Marek
Śliwa Tomasz
Świątkowski Andrzej
Tabiś Bolesław
Teoh Wey Yang
Thullie Jan
Vienken Joerg
Wade Jonathan
Wang Lei
Warmuziński Krzysztof
Weatherley Laurence
Wojdalski Janusz
Wu Zhaoliang
Zander Lidia
Zhang Mingyao
Zhang Zhenzhong
Żmuda Wiesław

CONTENTS OF CHEMICAL AND PROCESS ENGINEERING VOL. 38, 2017

ISSUE 1

ISSUE 2

ISSUE 3

ISSUE 4

AUTHOR INDEX
CHEMICAL AND PROCESS ENGINEERING, VOL. 38, 2017

Instructions for Authors

All manuscripts submitted for publication in Chemical and Process Engineering must comprise a description of original research that has neither been published nor submitted for publication elsewhere.

The content, aim and scope of the proposals should comply with the main subject of the journal, i.e. they should deal with mathematical modelling and/or experimental investigations on momentum, heat and mass transfer, unit processes and operations, integrated processes, biochemical engineering, statics and kinetics of chemical reactions. The experiments and modelling may cover different scales and processes ranging from the molecular phenomena up to production systems. The journal language is grammatically correct British English.

Chemical and Process Engineering publishes: i) full text research articles, ii) invited reviews, iii) letters to the editor and iv) short communications, aiming at important new results and/or applications. Each of the publication form is peer-reviewed by at least two independent referees.

Submission of materials for publication

The manuscripts are submitted for publication via email address *A.Bin@ichip.pw.edu.pl*. When writing the manuscript, authors should preferably use the template for articles, which is available on the *www.degruyter.com/view/j/cpe*.

Proposals of a paper should be uploaded using the Internet site of the journal and should contain:

- a manuscript file in Word format (*.doc, *.docx),
- the manuscript mirror in PDF format,
- all graphical figures in separate graphics files.

In the following paragraph the general guidelines for the manuscript preparation are presented.

Manuscript outline

1. Header details

a. Title of paper
b. Names (first name and further initials) and surnames of authors
c. Institution(s) (affiliation)
d. Address(es) of authors
e. Information about the corresponding author; academic title, name and surname, email address, address for correspondence

2. Abstract – should contain a short summary of the proposed paper. In the maximum of 200 words the authors should present the main assumptions, results and conclusions drawn from the presented study.

3. Keywords – Up to 5 characteristic keyword items should be provided.

4. Text

a. Introduction. In this part, description of motivation for the study and formulation of the scientific problem should be included and supported by a concise review of recent literature.
b. Main text. It should contain all important elements of the scientific investigations, such as presentation of experimental rigs, mathematical models, results and their discussion. This part may be divided into subchapters.
c. Conclusions. The major conclusions can be put forward in concise style in a separate chapter. Presentation of conclusions from the reported research work accompanied by a short commentary is also acceptable.

Figures: drawings, diagrams and photographs should be located in appropriate places in the manuscript text according to the template. Their graphical form should be of vector or raster type with the minimum resolution of 900 dpi. In addition, separate files containing each of the drawings, graphs and photos should be uploaded onto the journal Web site in one of the following formats: bmp, gif, tiff, jpg, eps. Due to rigid editorial reasons, graphical elements created within MS Word and Excel are not acceptable. The final length of figures should be intended typically for 8 cm (single column) or 16 cm in special cases of rich-detail figures. The basic font size of letters in figures should be at least 10 pts after adjusting graphs to the final length.

Figures: drawings, diagrams and photographs should be in gray scale. In case of coloured graphs or photo an additional payment of 300 PLN (72 €) per 1 page containing coloured figures on both sides, or 150 PLN (36 €) per page containing coloured figures on one side will be required.

Tables should be made according to the format shown in the template.

All figures and tables should be numbered and provided with appropriate title and legend, if necessary. They have to be properly referenced to and commented in the text of the manuscript.

5. List of symbols should be accompanied by their units

6. Acknowledgements may be included before the list of literature references

7. Literature citations

The method of quoting literature source in the manuscript depends on the number of its authors:

- single author – their surname and year of publication should be given, e.g. Marquardt (1996) or (Marquardt, 1996),
- two authors – the two surnames separated by the conjunction "and" with the publication year should be given, e.g. Charpentier and McKenna (2004) or (Charpentier and McKenna, 2004),
- three and more authors – the surname of the first author followed by the abbreviation "et al." and year of publication should be given, e.g. Bird et al. (1960) or (Bird et al., 1960).

In the case of citing more sources in one bracket, they should be listed in alphabetical order using semicolon for separation, e.g. (Bird et al., 1960; Charpentier and McKenna, 2004; Marquardt, 1996). Should more citations of the same author(s) and year appear in the manuscript then letters "a, b, c, ..." should be successively applied after the publication year.

Bibliographic data of the quoted literature should be arranged at the end of the manuscript text in alphabetic order of surnames of the first author. It is obligatory to indicate the DOI number of those literature items, which have the numbers already assigned. Journal titles should be specified by typing their right abbreviations or, in case of doubts, according to the List of Title Word Abbreviations available at http://www.issn.org/2-22661-LTWA-online.php.

Examples of citation for:

Articles

Charpentier J. C., McKenna T. F., 2004. Managing complex systems: some trends for the future of chemical and process engineering. *Chem. Eng. Sci.*, 59, 1617-1640. DOI: 10.1016/j.ces.2004.01.044.

Information from books (we suggest adding the page numbers where the quoted information can be found)

Bird R. B., Stewart W.E., Lightfood E.N., 2002. *Transport Phenomena*. 2nd edition, Wiley, New York, 415-421.

Chapters in books

Hanjalić K., Jakirlić S., 2002. Second-moment turbulence closure modelling, In: Launder B.E., Sandham N.D. (Eds.), *Closure strategies for turbulent and transitional flows*. Cambridge University Press, Cambridge, 47-101.

Conferences

ten Cate A., Bermingham S.K., Derksen J.J., Kramer H.M.J., 2000. Compartmental modeling of an 1100L DTB crystallizer based on Large Eddy flow simulation. *10th European Conference on Mixing*. Delft, the Netherlands, 2-5 July 2000, 255-264.

8. Payments

Starting from 2014 a principle of publishing articles against payment is introduced, assuming non-profit making editorial office. According to the principle authors or institutions employing them, will have to cover the expenses amounting to 40 PLN (or 10 €) per printed page. The above amount will be used to supplement the limited financial means received from the Polish Academy of Sciences for the editorial and publishing; and in particular to increase the capacity of the next CPE volumes and to proofread the linguistic correctness of the articles. The method of payment will be indicated in an invoice sent to the authors or institutions after acceptance of their manuscripts to be published. In justifiable cases presented in writing, the editorial staff may decide to relieve authors from basic payment, either partially or fully.

All correspondence should be sent to Editor-in-Chief, Prof. Andrzej K. Biń, email address *A.Bin@ichip.pw.edu.pl*.

The Azoty Group is a future-oriented project. But this has always been the case. When in 1927 President Ignacy Mościcki decided to build the State-owned Nitrogenous Compounds Factory it was a vision of the future. A vision of Poland's grand chemical industry.

This vision, and the history of all the companies the Group put together give us the picture of one of the key capital groups in the European fertiliser-chemical sector.

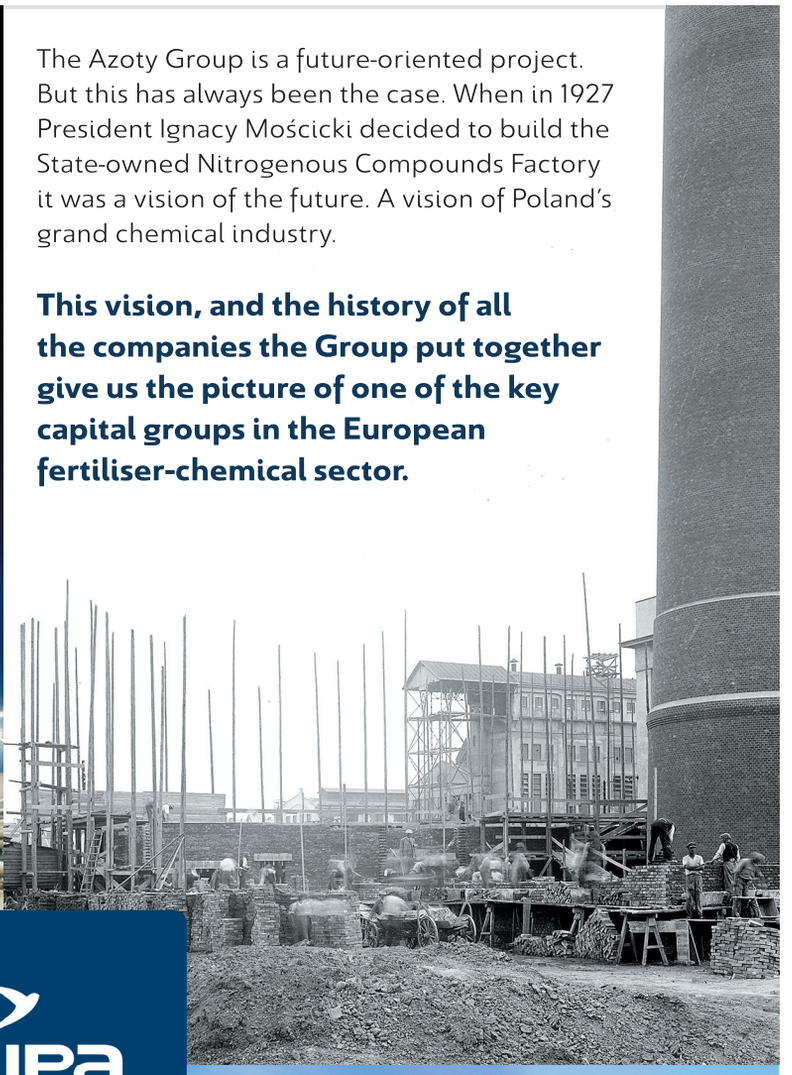

GRUPA AZOTY

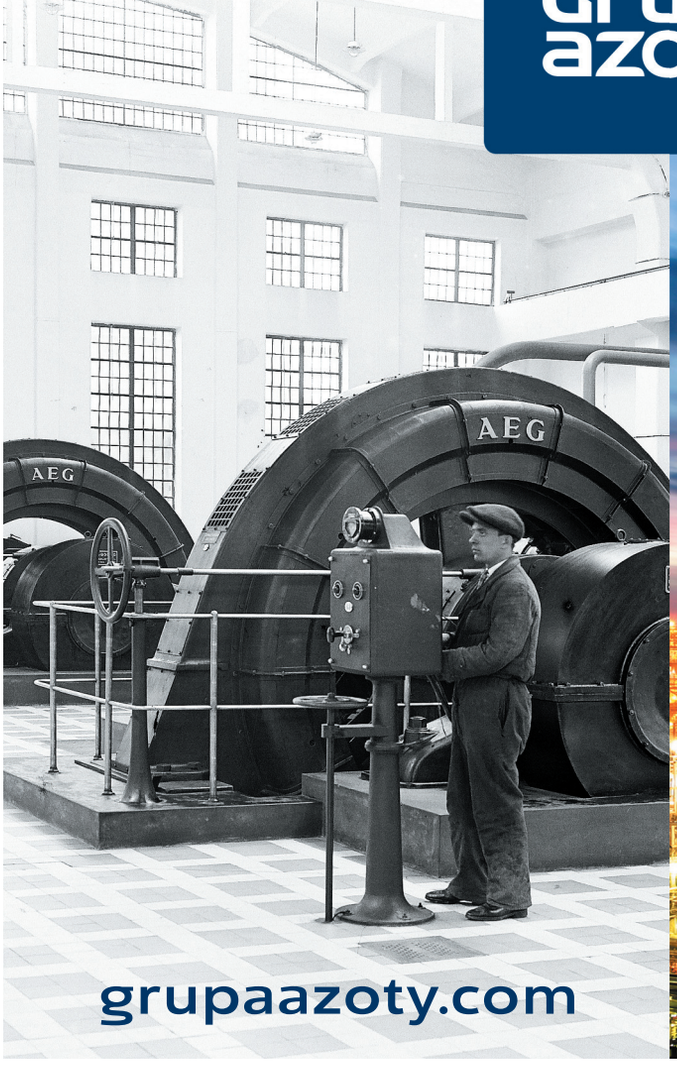

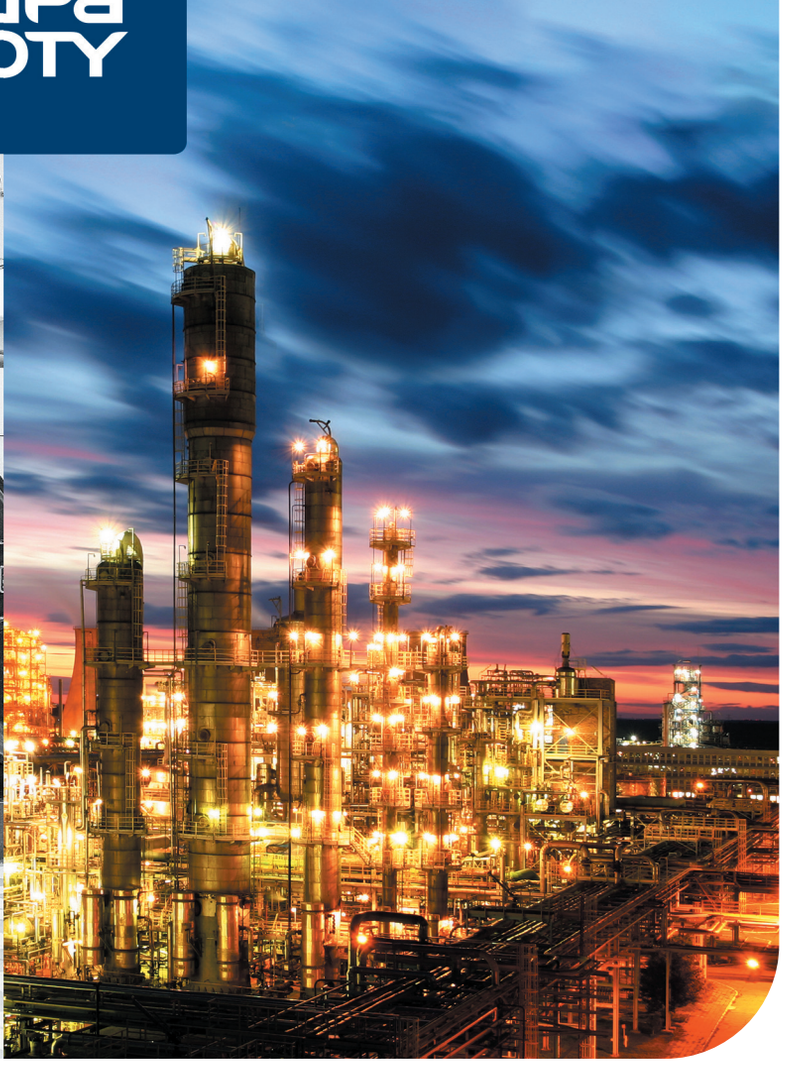

grupaazoty.com